Copyright
by
Jonás de Dios De Basabe Delgado
2009

The Dissertation Committee for Jonás de Dios De Basabe Delgado
certifies that this is the approved version of the following dissertation:

High-Order Finite Element Methods for Seismic Wave Propagation

Committee:

Mrinal K. Sen, Supervisor

Mary F. Wheeler, Supervisor

Clint Dawson

Björn Engquist

Omar Ghattas

High-Order Finite Element Methods for Seismic Wave Propagation

by

Jonás de Dios De Basabe Delgado, B.S.; M.S.

DISSERTATION

Presented to the Faculty of the Graduate School of

The University of Texas at Austin

in Partial Fulfillment

of the Requirements

for the Degree of

DOCTOR OF PHILOSOPHY

THE UNIVERSITY OF TEXAS AT AUSTIN

May 2009

To Eunice, my beloved wife.
And to our beautiful daughter Elena.

God is our refuge and strength,
an ever-present help in trouble.

Therefore we will not fear, though the earth give way
and the mountains fall into the heart of the sea.

Psalm 46:1–2

Acknowledgments

My sincere gratitude is extended to my advisor Mrinal K. Sen, who took me under his wing at the outset of graduate school. He introduced me to the topic of this dissertation and patiently guided me through all the development. His generous nature and the breadth of his knowledge make him an excellent advisor. I am indebted to him for teaching me, not only about Geophysics, but also about writing and publishing research papers.

I would also like to express my gratefulness to my coadvisor, Mary F. Wheeler. She has taught me all that I know about Finite Elements. I warmly remember all her words of encouragement and that she believed in me against all odds.

I am also deeply grateful to all of the other committee members: Clint Dawson, Björn Engquist and Omar Ghattas. I sincerely appreciate their valuable feedback. A special acknowledgement to Dimitri Komatitsch from the University of Pau, France, who provided substantial feedback on the grid dispersion analysis of the Spectral Element Method.

During the course of my studies I have been honored by many sponsorships that allowed me to focus on my research. First and foremost, it was a great privilege to be granted the CONACYT Fellowship from the Mexican Department for Science and Technology that supported me during the first four years of my graduate studies. The fifth year was supported by the Continuing Fellowship of the Graduate School from the University of Texas at Austin. Furthermore, I am grateful to the Bruton Fellowship, Gale White Fellowship and EDGER Fellowship, which provided additional support.

My mother is perhaps the largest contributor to my character and abilities. I acknowledge her spiritual and emotional investment in me, not only during my graduate studies, but throughout my lifetime. With deep feelings I acknowledge the support of my wife Eunice, who provides the inspiration for everything that I do.

Jonás de Dios De Basabe Delgado

High-Order Finite Element Methods for Seismic Wave Propagation

Publication No. _____

Jonás de Dios De Basabe Delgado, Ph.D.
The University of Texas at Austin, 2009

Supervisors: Mrinal K. Sen
Mary F. Wheeler

Purely numerical methods based on the Finite Element Method (FEM) are becoming increasingly popular in seismic modeling for the propagation of acoustic and elastic waves in geophysical models. These methods offer a better control on the accuracy and more geometrical flexibility than the Finite Difference methods that have been traditionally used for the generation of synthetic seismograms. However, the success of these methods has outpaced their analytic validation. The accuracy of the FEMs used for seismic wave propagation is unknown in most cases and therefore the simulation parameters in numerical experiments are determined by empirical rules. I focus on two methods that are particularly suited for seismic modeling: the Spectral Element Method (SEM) and the Interior-Penalty Discontinuous Galerkin Method (IP-DGM).

The goals of this research are to investigate the grid dispersion and stability of SEM and IP-DGM, to implement these methods and to apply them to subsurface models to obtain synthetic seismograms. In order to analyze the grid dispersion and stability, I use the von Neumann method (plane wave analysis) to obtain a generalized eigenvalue problem. I show that the eigenvalues are related to the grid dispersion and that, with certain assumptions, the size of the eigenvalue problem

can be reduced from the total number of degrees of freedom to one proportional to the number of degrees of freedom inside one element.

The grid dispersion results indicate that SEM of degree greater than 4 is isotropic and has a very low dispersion. Similar dispersion properties are observed for the symmetric formulation of IP-DGM of degree greater than 4 using nodal basis functions. The low dispersion of these methods allows for a sampling ratio of 4 nodes per wavelength to be used. On the other hand, the stability analysis shows that, in the elastic case, the size of the time step required in IP-DGM is approximately 6 times smaller than that of SEM. The results from the analysis are confirmed by numerical experiments performed using an implementation of these methods. The methods are tested using two benchmarks: Lamb's problems and the SEG/EAGE salt dome model.

Table of Contents

List of Tables

List of Figures

Chapter 1

Introduction

1.1 Motivation

During the last four decades there has been intensive research in numerical seismology focused on the development of methods to approximate the propagation of acoustic and elastic waves in the Earth. This has been motivated by the fact that exact analytic solutions do not exist for subsurface models of interest in exploration and global seismology. The advantage of the numerical methods is that they are based on the acoustic or elastic wave equations for heterogeneous media and therefore they can simulate direct waves, primary and multiply reflected and transmitted waves, surface and head waves, converted waves, diffracted waves and critically refracted waves, whenever these are present in the physical model.

The complexity and scale of the geophysical models in exploration and global seismology make the wave propagation problem mathematically and computationally challenging. To undertake this problem effectively a cross-disciplinary approach is required involving geophysics, applied mathematics and large-scale computing.

In the recent past the Finite Element Methods (FEM) have attracted the interest of researchers in the field of numerical wave propagation, in particular the Spectral Element (SEM) and Discontinuous Galerkin Methods (DGM). Some advantages of FEM are the flexibility with which it can accommodate surface topography, discontinuities in the subsurface model and boundary conditions, and the ability to approximate the wave field with polynomials of arbitrarily high order. DGM has the

further advantages that it can accommodate discontinuities, not only in the media parameters, but also in the wave field (pressure, displacement, velocity or stress, depending on the formulation), it can be energy conservative, it can handle more general meshes, and it is suitable for local time stepping and parallel implementations.

The main analysis tools that determine the applicability of a numerical method to the wave propagation problem are the stability and grid dispersion criteria. The stability criterion determines the largest time step for the time-marching scheme such that the numerical solution remains bounded. On the other hand, the grid dispersion criterion determines the largest sampling ratio for the spatial discretization such that the numerical solution has an acceptable accuracy.

Although FEM has been applied to the wave propagation problem since the late 60's and early 70's (Chopra et al., 1969; Lysmer & Drake, 1972; Smith, 1975), the grid dispersion and stability analysis was not available until the early 80's, and only for the first order FEM schemes (Mullen & Belytschko, 1982; Marfurt, 1984). The grid dispersion analysis was extended to higher-order elements for the acoustic case using SEM in Cohen (2002). Similarly, the grid dispersion properties of DGM have only been analyzed for the acoustic wave equation (Ainsworth et al., 2006). Thus the applicability of these methods for elastic wave propagation is unclear.

The goal of this dissertation is to implement SEM and the Interior Penalty DGM (IP-DGM) for acoustic and elastic wave propagation and investigate their grid dispersion and stability, paying particular attention to the high-order elastic case. Furthermore, I will use these methods to calculate wave fields on realistic geophysical models.

1.2 Research Objectives

1. Implement SEM and IP-DGM for acoustic and elastic wave propagation,
2. Analyze the grid dispersion and stability of SEM and IP-DGM, and
3. Systematically compare their efficiency and accuracy.

1.3 Literature Review

Two of the most common numerical methods to simulate the wave equation in the Earth are the Finite Differences Method (FDM) and FEM. Various schemes based on FDM and FEM are reported in geophysical literature. Examples of FDM are the standard-grid acoustic (Alterman & Karal, 1968; Alford et al., 1974) and elastic formulations (Kelly et al., 1976), and the staggered-grid formulation (Madariaga, 1976; Virieux, 1984, 1986; Levander, 1988). Examples of FEM include the Finite Volume Method (Dormy & Tarantola, 1995; Dumbser et al., 2007a), the Mixed FEM (Cohen & Fauqueux, 2000, 2005; Jenkins et al., 2002; Bécache et al., 2000, 2002), the classical FEM (Lysmer & Drake, 1972), SEM (Seriani & Priolo, 1994; Komatitsch & Vilotte, 1998), and DGM (Rivière & Wheeler, 2001; Grote et al., 2006; Chung & Engquist, 2006; Käser & Dumbser, 2006).

In this section I will summarize the development of the classical FEM, SEM and DGM as applied to seismic wave propagation with an emphasis on the stability and grid dispersion results.

1.3.1 Finite Element Method

The research on the applicability of FEM to seismology has been constantly progressing since the late 60's and early 70's (Chopra et al., 1969; Lysmer & Drake, 1972). Lysmer & Drake (1972), in their seminal paper, stressed out the advantages

of FEM as applied to the wave propagation problem, the main ones being the generality of the formulation, the flexibility with which media parameters and boundary conditions are handled, and the solid theory on which it is based. The early work on FEM for wave propagation considered only first order elements (Chopra et al., 1969; Lysmer & Drake, 1972; Smith, 1975; Mullen & Belytschko, 1982; Marfurt, 1984). The popularity of the method declined with respect to the FDM due to accuracy and efficiency limitations. One of the disadvantages of FEM that limited the applicability to seismology is that the proposed methods were implicit, which means that a linear system needed to be solved, and therefore were significantly slower than the competing FDM. The other disadvantage was that the accuracy was not better than that of FDM due to pollution by grid dispersion (Marfurt, 1984; De Basabe & Sen, 2007).

The grid dispersion of the classical FEM has been studied in Mullen & Belytschko (1982) and Marfurt (1984). Mullen & Belytschko (1982) considered the acoustic wave equation and compared the grid dispersion of elements of different shapes and of different types of mass lumping. They concluded that the quadrilateral elements represented the best choice for wave propagation and that the use of all the types of mass lumping that they considered had a detrimental effect in the accuracy. On the other hand, Marfurt (1984) considered acoustic and elastic wave propagation using quadrilateral elements. He inspected the grid dispersion due to the discretization in the space and time variables. He compared the grid dispersion of FEM to that of FDM and concluded that in either case a sampling ratio of 10 grid points per wave length should be used to get an acceptable accuracy and that neither method is suitable for media with a high Poisson's ratio.

Despite the disadvantages of the classical FEM, the generality and flexibility of the method make it still attractive for the wave propagation problem. The method

has been successfully applied to earthquake seismology by Bao et al. (1998) to simulate the seismic response of a subsurface model and estimate the risk for urban regions. To improve the efficiency, they used a mass lumping technique to render the method explicit. They controlled the loss of accuracy due to grid dispersion by increasing the sampling ratio.

1.3.2 Spectral Element Method

SEM, originally developed for fluid dynamics (Patera, 1984), has been successfully applied to the wave equation, addressing the efficiency issues and providing better accuracy than the FDM and more geometrical flexibility. This method was first implemented for the acoustic wave equation in the mid 90's by Seriani & Priolo (1994) using the Gauss-Lobatto-Chebyshev (GLC) nodes, and by Tordjman et al. (1994) and Tordjman (1995) using the Gauss-Lobatto-Legendre (GLL) nodes. The method was introduced to elastic wave propagation in the late 90's by Komatitsch & Vilotte (1998), and it quickly gained tremendous credibility within the seismological community (Komatitsch & Tromp, 1999, 2002a,b; Priolo, 2001; Komatitsch et al., 2005; Chaljub et al., 2007). It has been applied to problems in regional and global seismology obtaining results remarkably close to the empirical data (Komatitsch et al., 2002, 2004).

The main characteristics of SEM is that it uses high-order basis functions, with the advantage that a lower sampling ratio can be used, typically between 4 and 5 nodes per wave length. The mass matrix can be diagonalized by using the GLL nodes for the distribution of the nodes inside the elements and the GLL quadrature rules for the approximation of it's entries, thus avoiding the added cost of using high-order basis functions. The use of the GLL nodes and quadrature rules is tantamount to mass lumping, with the advantage that it preserves the accuracy.

The success of SEM in seismic modeling has outpaced it's analytic validation. The accuracy of SEM in 2D using the GLC nodes was empirically investigated by Seriani & Priolo (1994) for the acoustic scheme. They concluded that an average of 4.5 nodes per wave length with an eighth-order method eliminates grid dispersion. Although this showed promising results, the use of the GLC nodes does not lead to mass lumping. The accuracy of the 1D acoustic SEM scheme using the GLL, GLC or equispaced nodes was examined by Mulder (1999). He used a Fourier transform in the spatial variable to analyze the grid-dispersion error of the high-order methods and concluded that the error introduced by the spurious, or non-physical, modes can be neglected and that SEM using GLL nodes and quadrature rules was more accurate than using the GLC or equispaced nodes. On the other hand, Cohen (2002) analyzed the grid dispersion of the 1D, 2D and 3D acoustic SEM schemes using GLL nodes and quadrature rules. He used an eigenvalue formulation and Taylor series to get the asymptotic behavior of the grid dispersion. In his results, he showed dispersion curves for the 1D case using second- or third-order methods and various time-stepping schemes. See also the preliminary results in Tordjman et al. (1994), Tordjman (1995) and Fauqueux (2003). Finally, Ainsworth (2004a) studied the grid dispersion of arbitrary high-order elements in the acoustic case and obtained closed-form dispersion relations using Padé approximants. He considered the 1D case and outlined the extension to higher dimensions. As for the elastic SEM, there seems to be no grid dispersion or stability analyses available in the literature. This has led the geophysicists to set the order of the elements and the grid spacing according to the results available for the acoustic case (Komatitsch et al., 2005; Chaljub et al., 2007).

1.3.3 Discontinuous Galerkin Method

DGM was originally proposed in Reed & Hill (1973) to solve the hyperbolic neutron transport equation. The general framework for solving hyperbolic differential equations, using a first order conservative form, with DGM was developed by Cockburn and his collaborators in Cockburn & Shu (1989); Cockburn et al. (1989, 1990); and Cockburn & Shu (1998). In these papers, they proposed discretizing the differential equation in space using a flux formulation and a Runge-Kutta scheme to advance the system in time, thus the name Runge-Kutta DG (RKDG). The order of the Runge-Kutta scheme should be the same as the order of the DG scheme to obtain formally the same accuracy in space and in time.

In seismic wave propagation it is usually desirable to use basis functions of polynomial order between 4 and 10 (Komatitsch et al., 2005; Chaljub et al., 2007). As the order of the approximation in space gets higher, it can be cumbersome to use a high-order Runge-Kutta scheme to obtain the same accuracy for the approximation in time.

Instead of using a Runge-Kutta scheme for time stepping, the ADER method has been recently proposed (Dumbser & Munz, 2006; Käser & Dumbser, 2006; Dumbser & Käser, 2006; Käser et al., 2007a,b; de la Puente et al., 2007; Dumbser et al., 2007a,b). The goal of the ADER approach is to obtain the same accuracy for the space and time discretizations. This approach is based on a Taylor expansion in time of the wave field and a substitution of the time derivatives by space derivatives in the Taylor expansion using the Cauchy-Kovalewski procedure.

Other DGMs that have been examined for the wave propagation problem are the Non-symmetric Interior Penalty Galerkin (NIPG), the Symmetric Interior Penalty Galerkin (SIPG) and the Optimal DG. The convergence of the NIPG method

was analyzed in Rivière & Wheeler (2001). They considered the second order acoustic and elastic wave equations, and determined based on *a priori* error estimates that the convergence is optimal with respect to the element size in the energy norm and suboptimal in the L^2 norm. The SIPG method was studied by Grote et al. (2006), but they considered only the acoustic wave equation; they demonstrated optimal convergence with respect to the element size in the Energy and L^2 norms. Finally, the Optimal-DG method was developed and analyzed by Chung & Engquist (2006). This method is applicable to the acoustic wave equation in the first-order conservative form. The emphasis of this method was to obtain all of the following desirable characteristics: explicit time marching, energy conservative, and optimal higher-order accuracy.

The grid dispersion of DGM for wave propagation has been analyzed in Hu et al. (1999), Stanescu et al. (2000), Ainsworth (2004b) and Ainsworth et al. (2006). In Hu et al. (1999), the dispersion and dissipation errors of the discretization of the scalar advection equation and the acoustic wave equation are considered using the flux formulation DGM, Legendre basis functions, and triangular and quadrilateral elements. Stanescu et al. (2000) considered the flux formulation DGM applied to the scalar advection equation and linearized Euler equation in one spatial dimension. They did not use plane wave analysis and considered the dispersion due to the boundary conditions. Their formulation depends on a particular discretization of the domain. Ainsworth (2004b) studied the linearized advection equation in multiple space dimensions using a flux formulation DGM and tensor product basis functions. Finally, Ainsworth et al. (2006) considered the acoustic wave equation and IP-DGM as well as the flux formulation. Their grid dispersion results include up to third degree polynomial basis functions and conjecture on the extension to higher degree.

It should be noted that there are no results available for the grid dispersion

properties of any of the DGMs that are applicable to the elastic wave propagation. Furthermore, it cannot be assumed that the results available for the acoustic case can be applied to the elastic case.

1.4 Contributions

The contributions of this work can be summarized in two categories:

1. I have rigorously studied the applicability of the high-order SEM and IP-DGM to acoustic and elastic wave propagation. I have considered the accuracy in terms of grid dispersion and the stability, and obtained results that are readily useful to determine the parameters for numerical experiments. To the knowledge of the author, this is the first analysis of these methods for the elastic and the high-order acoustic cases.

2. I have developed a C++ code for seismic wave propagation that is useful, not only to test the methods and confirm the conclusions from the analysis, but also to perform numerical experiments using realistic geophysical models. In this code, I have included SEM, IP-DGM and Staggered Grid FDM, and many types of time-stepping methods. What makes this code different from others is the integration of all these methods for the discretization of the acoustic and elastic wave equations in space and in time. This code is particularly suited to evaluate and compare, not only the different methods, but also the different versions and basis functions of IP-DGM. The output of this program includes all the results considered useful in seismic modeling, including the snapshots, seismograms and shot gathers. The model, methods and output are fully configurable through an input file.

1.5 Dissertation Outline

After this introduction, the remainder of this dissertation is organized as follows. Chapter 2 describes the strong and weak formulations of the acoustic and elastic wave equations and introduces the numerical methods to discretize them in space and time. The 3rd chapter contains the grid dispersion and stability analyses of the methods. Chapter 4 focuses on the numerical experiments and shows the results for benchmark tests and realistic models. Finally, chapter 5 summarizes the conclusions and discusses possible directions for further research.

Chapter 2

Discretizations of the Wave Equation

This chapter introduces the basic equations used in seismic modeling, the numerical methods and the notation that will be used in the following chapters. It starts by presenting the strong form of the equations, and then proceeds to show the weak formulations used in FEM and IP-DGM. Finally, it describes the time-stepping strategies.

2.1 Formulations of the Wave Equation

There exist various forms of the wave equation useful in seismic modeling. Examples of these are the acoustic and elastic wave equations. The acoustic wave equation models compressional waves propagating through the domain, it is also known as the pressure formulation or as the scalar wave equation because the dependent variable is the pressure, a scalar field. The elastic wave equation models the propagation of compressional and shear waves, it is a more accurate approximation to the propagation of waves in the Earth but it is typically more difficult to solve and computationally more expensive because it needs to be solved for the displacement, a vector field. Different versions of the elastic wave equation exist for isotropic, anisotropic, homogeneous or heterogeneous media.

The wave propagation phenomena is modeled by the equation of motion, which is given by (using Einstein's summation convention)

$$\rho \partial_{tt} u_i = \partial_j \sigma_{ij} + \partial_j m_{ij} + f_i \quad \text{in} \quad \Omega \times (0, T] \quad i, j = 1, \ldots, d, \tag{2.1.1}$$

where d is the number of physical dimensions (2 or 3), $\Omega \subset \mathbb{R}^d$ is the physical domain, $(0, T]$ is the time domain, u_i is the displacement vector, σ_{ij} is the stress tensor, and the source is described by the moment tensor m_{ij} and the force vector f_i. The shorthand notation $\partial_l u_k = \partial u_k / \partial x_l$ is used in the above equation. The stress tensor can be written as a function of the displacement using the generalized Hooke's Law, also known as the stress–strain relation. In an elastic medium, the stress is linearly related to the displacement as follows:

$$\sigma_{ij}(\boldsymbol{u}) = C_{ijkl}\varepsilon_{kl}(\boldsymbol{u}), \tag{2.1.2}$$

where C_{ijkl} is the elastic fourth order tensor with symmetries $C_{ijkl} = C_{klij} = C_{jikl}$, and ε_{kl} is the strain tensor, defined as

$$\varepsilon_{kl}(\boldsymbol{u}) = \frac{1}{2}\left(\partial_l u_k + \partial_k u_l\right). \tag{2.1.3}$$

In an isotropic medium, the stress tensor is given by

$$\sigma_{ij}(\boldsymbol{u}) = \lambda \partial_k u_k \delta_{ij} + \mu(\partial_i u_j + \partial_j u_i), \tag{2.1.4}$$

where λ and μ are the Lamé parameters and are assumed to be varying in space in an heterogeneous medium, and δ_{ij} is Kronecker's delta.

In an acoustic medium $\mu = 0$, thus Hooke's law is simplified to

$$\sigma_{ij} = \lambda \partial_k u_k \delta_{ij} = \delta_{ij} p, \tag{2.1.5}$$

where p is the pressure. Substituting in the equation of motion and dividing by the density yields

$$\partial_{tt} u_i = \rho^{-1}\left(\partial_i p + \partial_j m_{ij} + f_i\right). \tag{2.1.6}$$

Finally, the acoustic wave equation is obtained by taking the divergence on both sides of the equation. Prescribing suitable boundary and initial conditions, the

acoustic wave equation is given by

$$\begin{aligned} \lambda^{-1}\partial_{tt}p - \partial_i\rho^{-1}\partial_i p &= \tilde{f} && \text{in} \quad \Omega \\ p &= 0 && \text{on} \quad \Gamma_D \\ \rho^{-1}\partial_i p\, n_i &= 0 && \text{on} \quad \Gamma_N \\ p = \partial_t p &= 0 && \text{for} \quad t = 0 \end{aligned} \tag{2.1.7}$$

where $\tilde{f} = \partial_i\rho^{-1}\left(\partial_j m_{ij} + f_i\right)$, $\Gamma_D \cup \Gamma_N = \partial\Omega$, $\Gamma_D \cap \Gamma_N = \emptyset$, $\partial\Omega$ is the boundary of Ω, and $n_i, i = 1, \ldots, d$, is a unit vector outward normal to $\partial\Omega$.

The elastic wave equation in an isotropic heterogeneous medium is obtained by substituting Hooke's law in the equation of motion, and is given by

$$\begin{aligned} \rho\partial_{tt}u_i - \partial_i\lambda\partial_j u_j - \partial_j\mu(\partial_j u_i + \partial_i u_j) &= \partial_j m_{ij} + f_i && \text{in} \quad \Omega \\ u_i &= 0 && \text{on} \quad \Gamma_D \\ \lambda\partial_k u_k n_i + \mu(\partial_i u_j + \partial_j u_i)n_j &= 0 && \text{on} \quad \Gamma_N \\ u_i = \partial_t u_i &= 0 && \text{for} \quad t = 0. \end{aligned} \tag{2.1.8}$$

2.2 Finite Element Method

This section describes the discretization in space of the acoustic and elastic wave equations using FEM. The first step in a finite element approximation is to derive the weak, or variational, formulations of eqs. (2.1.7) and (2.1.8). The weak formulation is then discretized by introducing an approximation for the pressure or displacement in a finite-dimensional subspace to obtain a linear system of ordinary differential equations. In the following, $d = 2$ will be assumed for succinctness.

2.2.1 Acoustic Formulation

The weak formulation of the acoustic wave equation is given by the following statement: Find $p \in X^C = \{\varphi \mid \varphi \in H^1(\Omega), \varphi = 0 \text{ on } \Gamma_D\}$ such that for all $v \in X^C$

$$\partial_{tt}\int_\Omega \frac{1}{\lambda} pv \; dx \; dz + \int_\Omega \frac{1}{\rho}\nabla p \cdot \nabla v \; dx \; dz = \int_\Omega \tilde{f} v \; dx \; dz. \tag{2.2.1}$$

The equivalence of eq. (2.1.7) with the above statement is given by the following proposition.

Proposition 2.2.1. *(i) If p is a solution to eq. (2.1.7), then it is also a solution to eq. (2.2.1); (ii) If p is a solution to eq. (2.2.1) and $p \in H^2(\Omega)$, then it is also a solution to eq. (2.1.7).*

Proof. (i) The equivalence is readily obtained by observing that multiplying eq. (2.1.7) by an arbitrary function in X^C and applying the divergence theorem yields eq. (2.2.1).

(ii) Let $\hat{p} \in H^2(\Omega)$ be a solution to eq. (2.2.1). Substituting in eq. (2.2.1) and applying the divergence theorem yields

$$\int_{\Omega} \left(\partial_{tt} \frac{1}{\lambda} \hat{p} - \nabla \cdot \frac{1}{\rho} \nabla \hat{p} - \tilde{f} \right) v \, dx \, dz = \int_{\Gamma_N} v \frac{1}{\rho} \nabla \hat{p} \cdot \boldsymbol{n} \, ds \quad \forall \, v \in X^C. \tag{2.2.2}$$

Taking $v \in H_0^1(\Omega)$ immediately yields eq. (2.1.7), and using the fact that the left-hand side is identically zero yields the homogeneous Newmann boundary condition. □

Using eq. (2.2.1), the original PDE can be written as a system of ODEs by introducing a finite dimensional subspace $X_h^C \subset X^C$, with basis $\{\phi_i\}_{i=1}^n$. Substituting in eq. (2.2.1) for p the approximation p_h given by the linear combination

$$p_h(x, z, t) = P_j(t)\phi_j(x, z) \, , \tag{2.2.3}$$

where P_j are the coefficients of the FEM approximation p_h, and substituting for v each of the basis functions, yields

$$M_{ij} \partial_{tt} P_j + K_{ij} P_j = F_i, \tag{2.2.4}$$

where

$$M_{ij} = \int_\Omega \frac{1}{\lambda}\phi_i\phi_j \, dx \, dz, \tag{2.2.5}$$

$$K_{ij} = \int_\Omega \frac{1}{\rho}\nabla\phi_i \cdot \nabla\phi_j \, dx \, dz, \tag{2.2.6}$$

$$F_i = \int_\Omega f\phi_i \, dx \, dz. \tag{2.2.7}$$

Usually in the FEM literature $\boldsymbol{M} = (M_{ij})$ is called the mass matrix and $\boldsymbol{K} = (K_{ij})$ is called the stiffness matrix. I will use these names because they are standard in FEM terminology although they can be misleading in the wave propagation context since the matrices are not necessarily related to mass or stiffness. The ODE system (2.2.4) is called the continuous in time or semidiscrete form of eq. (2.2.1) because it has been discretized in space through the substitution of the basis functions but the time derivative remains. The convergence of the method in the semidiscrete case is given by the following theorem (Dupont, 1973, Theorem 1).

Theorem 2.2.2. *Let p be the solution to eq. (2.2.1) and suppose that p, $\partial_t p \in L^\infty(H^m(\Omega))$ and $\partial_{tt} p \in L^2(H^m(\Omega))$. Then there exists a constant C such that*

$$\|\partial_t(p_h - p)\|_{L^\infty(0,T;L^2(\Omega))} + \|p_h - p\|_{L^\infty(0,T;L^2(\Omega))} \leq Ch^m. \tag{2.2.8}$$

Altough The proof of the above theorem is beyond the scope of this work, it should be noted that it uses Grönwall's lemma and therefore the constant C can be large for long propagation times. The corresponding theorem for the discretization in time can be found in Dupont (1973).

2.2.2 Elastic Formulation

The weak form of the elastic wave equation is given by the following statement: Find $\boldsymbol{u} \in \boldsymbol{X}^C = \{\boldsymbol{\varphi} \mid \boldsymbol{\varphi} \in \boldsymbol{H}^1(\Omega),\ \boldsymbol{\varphi} = 0 \text{ on } \Gamma_D\}$ such that for all $\boldsymbol{v} \in \boldsymbol{X}^C$

$$\int_\Omega \Big(\lambda(\nabla \cdot \boldsymbol{u})(\nabla \cdot \boldsymbol{v}) + \mu(\nabla \boldsymbol{u} + \nabla \boldsymbol{u}^T) : \nabla \boldsymbol{v}\Big)\, dx\, dz + \partial_{tt} \int_\Omega \rho \boldsymbol{u} \cdot \boldsymbol{v}\, dx\, dz = \int_\Omega \boldsymbol{f} \cdot \boldsymbol{v}\, dx\, dz, \tag{2.2.9}$$

where the double dot product is defined as $\boldsymbol{A} : \boldsymbol{B} = A_{ij}B_{ij}$ for $\boldsymbol{A} = (A_{ij})$ and $\boldsymbol{B} = (B_{ij})$. The equivalence of the above statement with eq. (2.1.8) is given without proof in the following proposition. The proof follows the same steps as that of Proposition 2.2.1.

Proposition 2.2.3. *(i) If $\boldsymbol{u}$ is a solution to eq. (2.1.8), then it is also a solution to eq. (2.2.9); (ii) If $\boldsymbol{u}$ is a solution to eq. (2.2.9) and $\boldsymbol{u} \in \boldsymbol{H}^2(\Omega)$, then it is also a solution to eq. (2.1.8).*

We can now use the weak formulation of the elastic wave equation to obtain a system of ODEs by introducing the finite dimensional subspace $\boldsymbol{X}_h^C = X_h^C \times X_h^C \subset \boldsymbol{X}^C$. Substituting for $\boldsymbol{u}$ the approximation $\boldsymbol{u}_h \in \boldsymbol{X}_h^C$ given by the linear combination

$$\boldsymbol{u}_h(x,z,t) = \big(U_j^x(t)\phi_j(x,z)\ ,\ U_j^z(t)\phi_j(x,z)\big)^T, \tag{2.2.10}$$

where U_j^x and U_j^z are the coefficients of the FEM approximations to the horizontal and vertical displacement respectively, and substituting $\boldsymbol{v} = (\phi_i, 0)^T$ yields the following system of equations

$$M_{ij}\partial_{tt}U_j^x + K_{ij}^1 U_j^x + K_{ij}^2 U_j^z = F_i^x. \tag{2.2.11}$$

Similarly, substituting $\boldsymbol{v} = (0, \phi_i)^T$, yields

$$M_{ij}\partial_{tt}U_j^z + K_{ij}^3 U_j^x + K_{ij}^4 U_j^z = F_i^z, \tag{2.2.12}$$

where the matrices in eqs. (2.2.11) and (2.2.12) are given by

$$M_{ij} = \int_\Omega \rho\phi_i\phi_j \, dx \, dz, \tag{2.2.13}$$

$$K^1_{ij} = \int_\Omega \Big((\lambda+2\mu)\phi_{i,x}\phi_{j,x} + \mu\phi_{i,z}\phi_{j,z}\Big) \, dx \, dz, \tag{2.2.14}$$

$$K^2_{ij} = \int_\Omega (\lambda\phi_{i,x}\phi_{j,z} + \mu\phi_{i,z}\phi_{j,x}) \, dx \, dz, \tag{2.2.15}$$

$$K^3_{ij} = \int_\Omega (\lambda\phi_{i,z}\phi_{j,x} + \mu\phi_{i,x}\phi_{j,z}) \, dx \, dz, \tag{2.2.16}$$

$$K^4_{ij} = \int_\Omega \Big((\lambda+2\mu)\phi_{i,z}\phi_{j,z} + \mu\phi_{i,x}\phi_{j,x}\Big) \, dx \, dz, \tag{2.2.17}$$

$$F^x_i = \int_\Omega f_x\phi_i \, dx \, dz, \tag{2.2.18}$$

$$F^z_i = \int_\Omega f_z\phi_i \, dx \, dz, \tag{2.2.19}$$

where f_x and f_z are the x and z components of $\boldsymbol{f}$. In these equations, the shorthand notation $\phi_{i,x} = \partial\phi_i/\partial x$ and $\phi_{i,z} = \partial\phi_i/\partial z$ is used.

2.2.3 Basis Functions

Basis functions, also known as shape functions, play an important role in FEM. A careful selection of them can lead to an accurate and efficient numerical scheme. In this section I will describe some important characteristics of the basis functions used in FEM without trying to be exhaustive. A detailed description of them can be found in Karniadakis & Sherwin (1999), where nodal and modal basis functions are defined. A concise description of modal basis is that they are of increasing polynomial degree and that they are hierarchical; that is, the modal basis of degree $\kappa+1$ are the basis of degree κ plus a polynomial of degree $\kappa+1$. On the other hand, nodal basis are of uniform degree and are given by interpolating over a set of nodes inside a given interval, as described below. Here I will consider nodal basis functions only because they are amenable to mass lumping and are the most popular in seismic modeling.

The basis functions in FEM are continuous piecewise polynomial functions with local support. For a basis of degree κ, a grid in one element is defined by setting $\kappa + 1$ nodes in each side of the element, therefore the element will have a total of $(\kappa + 1)^2$ nodes. In a classical FEM, the nodes are uniformly distributed in each side of the elements as shown in Fig. 2.1a. However, they can also be distributed non-uniformly. For example, the nodes can be the Gauss-Lobatto-Legendre (GLL) nodes as shown in Fig. 2.1b (Cohen, 2002).

I will first consider the basis functions in a unitary square element with corners at (0,0), (0,1), (1,0) and (1,1) (see Fig. 2.1). Let $\{\xi_i\}_{i=0}^{\kappa}$ be the nodes in either side of the element (note that $\xi_0 = 0$ and $\xi_\kappa = 1$) and let $\{\varphi_j\}_{j=0}^{\kappa}$ be the Lagrange polynomials of degree κ that interpolate these nodes satisfying $\varphi_j(\xi_i) = \delta_{ij}$, where δ_{ij} is Kronecker's delta defined to be 1 for $i = j$ and zero otherwise. Using these polynomials, the basis functions in the unit square element are given by

$$\phi_q^e(x, z) = \varphi_i(x)\varphi_j(z), \quad i, j = 0, 1, \ldots, \kappa. \tag{2.2.20}$$

where I have numbered the basis functions with $q = (\kappa + 1)j + i$ instead of the equivalent of using two indices, this notation is useful to reduce the number of indices, for example, in eqs. (2.2.4), (2.2.11) and (2.2.12). Note that the range of the index is $q = 0, 1, \ldots, (\kappa + 1)^2 - 1$, and that by construction $\phi^e_{(\kappa+1)j+i}(x_m, z_n) = \varphi_i(x_m)\varphi_j(z_n) = \delta_{im}\delta_{jn}$. When the basis functions are constructed this way they are usually called tensor-product Lagrange basis functions.

Basis functions defined on the entire domain can be constructed using the ones defined in eq. (2.2.20). First note that a basis function can be defined on a node of any element by translating, stretching and scaling eq. (2.2.20). Using these, a global basis function can be built for each node in the domain by fixing them to be zero in all the elements except on those that include the node and putting together all the basis functions defined to be one in that node.

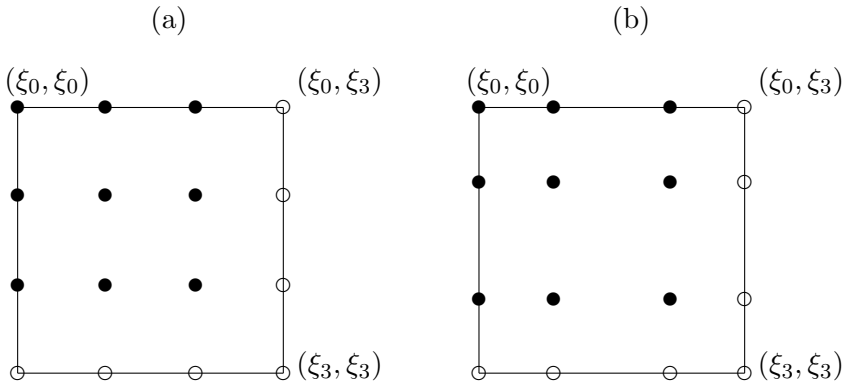

Figure 2.1: An example of a third order element in a finite element mesh using (a) equispaced nodes and (b) the GLL nodes. Filled circles represent distinct degrees of freedom, see section 3.1.

2.3 Interior-Penalty Discontinuous Galerkin Method

This section introduces the weak formulations of the acoustic and elastic wave equations used in IP-DGM. There are three important differences between the weak formulations used in FEM and IP-DGM. In IP-DGM the basis functions are allowed to be discontinuous at the element boundaries, the integrals are performed element wise, and the continuity of the wave field across the elements is weakly imposed using penalties.

In the following, Ω_h denotes a finite element partition of the domain, and Γ_h the set of all the faces between the elements in Ω_h. Also, $\{\cdot\}$ denotes the average of the function at $\gamma \in \Gamma_h$ and $[\cdot]$ the function jump. This is the standard notation in the DGM literature (Wheeler, 1978), and it is defined as follows: Let γ be the edge between the elements E_1 and E_2, then the jump and average of a scalar function u on γ are given by

$$\{u\} = \frac{1}{2}(u|_{E_1} + u|_{E_2}) \quad \text{and} \quad [u] = u|_{E_1} - u|_{E_2}, \tag{2.3.1}$$

and for a vector function $\boldsymbol{u}$,

$$\{\boldsymbol{u}\} = \frac{1}{2}(\boldsymbol{u}|_{E_1} + \boldsymbol{u}|_{E_2}) \quad \text{and} \quad [\boldsymbol{u}] = \boldsymbol{u}|_{E_1} - \boldsymbol{u}|_{E_2}. \tag{2.3.2}$$

2.3.1 Acoustic Formulation

The interior-penalty weak formulation of the acoustic wave equation is given by the following statement: Find $p \in X^D$ such that for all $v \in X^D$

$$\sum_{E\in\Omega_h} \Big(\left(\lambda^{-1}\partial_{tt}p, v\right)_E + B_E(p,v) \Big) + \sum_{\gamma\in\Gamma_h} J_\gamma(p,v;S,R) = \sum_{E\in\Omega_h} (\tilde{f}, v)_E \tag{2.3.3}$$

where

$$\begin{aligned}
(u,v)_E &= \int_E uv \; dx \; dz, && (2.3.4)\\
B_E(p,v) &= \int_E \rho^{-1}\nabla p \cdot \nabla v \; dx \; dz, && (2.3.5)\\
J_\gamma(p,v;S,R) &= -\int_\gamma \{\rho^{-1}\nabla p \cdot \boldsymbol{n}^\gamma\}[v] \; d\gamma + S\int_\gamma \{\rho^{-1}\nabla v \cdot \boldsymbol{n}^\gamma\}[p] \; d\gamma && (2.3.6)\\
&+ R\int_\gamma \{\rho^{-1}\}[p][v] \; d\gamma,
\end{aligned}$$

and $X^D = \left\{\varphi \mid \varphi \in H^1(E) \; \forall \; E \in \Omega_h, \; \varphi = 0 \text{ on } \Gamma_D\right\}$ with norm

$$\|\varphi\|_{X^D} = \sum_{E\in\Omega_h} \|\varphi\|_{H^1(E)}. \tag{2.3.7}$$

The parameter R in eq. (2.3.6) is the penalty, and S is a parameter that takes the values 0, 1 or -1 depending on the particular formulation of IP-DGM: $S = 0$ for IIPG (Dawson et al., 2004), $S = -1$ for SIPG (Darlow, 1980; Grote et al., 2006) and $S = 1$ for NIPG (Rivière et al., 1999, 2001).

Proposition 2.3.1. *(i) If p is a solution to eq. (2.1.7), then it is also a solution to eq. (2.3.3); (ii) If p is a solution to eq. (2.3.3) and $p \in H^2(\Omega)$, then it is also a solution to eq. (2.1.7).*

Proof. *(i)* Multiplying eq. (2.1.7) by a test function, integrating over an arbitrary element E and using the Gauss divergence theorem yields

$$\partial_{tt}\int_E pv\ dx\ dz + \int_E \rho^{-1}\nabla p\cdot\nabla v\ dx\ dz - \int_{\partial E}\rho^{-1}\nabla p\cdot\boldsymbol{n}v\ d\gamma = \int_E \tilde{f}v\ dx\ dz. \quad (2.3.8)$$

Eq. (2.3.3) is obtained upon addition through all the elements and noting that the second and third terms of J_γ vanish whenever p is continuous.

(ii) The opposite equivalence is readily obtained by reversing the steps of part (i) and recalling that $H^2(\Omega)$ is embedded in $C^0(\Omega)$ by the Sobolev embedding theorem. □

To solve for the pressure in eq. (2.3.3), a subspace $X_h^D \subset X^D$ is introduced by defining a finite number of basis functions $\{\phi_i^E\}_{i=1}^m$ in element E for all $E \in \Omega_h$. The basis functions ϕ_i^E will be discussed at the end of this section. The following chapters will take advantage of these basis functions being defined element wise, but for the purposes of this chapter, a global enumeration of the basis functions will be introduce here $\varphi_j = \phi_i^e$, where $j = i + em$, $e = 0, \ldots, N_e - 1$, and N_e is the total number of elements in Ω_h. With this numbering of the basis functions, a linear system like that in eq. (2.2.4) is obtained, where

$$M_{ij} = \sum_{E\in\Omega_h} (\lambda^{-1}\varphi_i, \varphi_j)_E \quad (2.3.9)$$

$$K_{ij} = \sum_{E\in\Omega_h} B_E(\varphi_i, \varphi_j) + \sum_{\gamma\in\Gamma_h} J_\gamma(\varphi_i, \varphi_j; S, R) \quad (2.3.10)$$

$$F_i = \sum_{E\in\Omega_h} (\tilde{f}, \varphi_i)_E. \quad (2.3.11)$$

The following theorems regarding the convergence of the method are given for completeness. Their proofs are beyond the scope of this dissertation and can be found elsewhere.

Theorem 2.3.2. *(NIPG convergence, Rivière & Wheeler, 2001, Theorems 3.2 and 3.4) Let $p_h \in X_h^D$ satisfy*

$$\sum_{E\in\Omega_h}\Big(\left(\lambda^{-1}\partial_{tt}p_h, v\right)_E + B_E(p_h, v)\Big) + \sum_{\gamma\in\Gamma_h}\Big(J_\gamma(p_h, v; 1, R) + R\int_\gamma \{\rho^{-1}\}[\partial_t p_h][v]\, d\gamma\Big) = \sum_{E\in\Omega_h}(\tilde{f}, v)_E \tag{2.3.12}$$

for all $v \in X_h^D$, with $R \geq R_0 > 0$, and suppose that $p, \partial_t p \in L^\infty(H^m(\Omega))$ and $\partial_{tt}p \in L^2(H^m(\Omega))$. Then there exist constants C_1 and C_2 independent of h and κ such that

$$\|p_h - p\|_{L^\infty(0,T;X^D)} \leq C_1 \frac{h^{\mu-1}}{\kappa^{m-1}} \tag{2.3.13}$$

and

$$\|p_h - p\|_{L^\infty(0,T;L^2)} \leq C_2 \frac{h^{\mu-1}}{\kappa^{m-1}} \tag{2.3.14}$$

where $\kappa \geq 1$ and $\mu = \min(\kappa+1, m)$.

Theorem 2.3.3. *(SIPG convergence, Grote et al., 2006, Theorems 4.1 and 4.2) Let $p_h \in X_h^D$ satisfy*

$$\sum_{E\in\Omega_h}\Big(\left(\lambda^{-1}\partial_{tt}p_h, v\right)_E + B_E(p_h, v)\Big) + \sum_{\gamma\in\Gamma_h} J_\gamma(p_h, v; -1, R) = \sum_{E\in\Omega_h}(\tilde{f}, v)_E \tag{2.3.15}$$

for all $v \in X_h^D$, with $R \geq R_0 > 0$, and suppose that $p, \partial_t p \in L^\infty(H^m(\Omega))$ and $\partial_{tt}p \in L^2(H^m(\Omega))$. Then there exist constants C_1 and C_2 independent of h and κ such that

$$\|\partial_t(p_h - p)\|_{L^\infty(0,T;L^2)}\|p_h - p\|_{L^\infty(0,T;X^D)} \leq C_1 h^{\mu-1} \tag{2.3.16}$$

and

$$\|p_h - p\|_{L^\infty(0,T;L^2)} \leq C_2 h^{\mu} \tag{2.3.17}$$

where $\kappa \geq 1$ and $\mu = \min(\kappa+1, m)$.

Note that Theorem 2.3.2 deals with the convergence of a slightly different problem than the one formulated at the beginning of this section because there is one extra term penalizing the first time derivative of the pressure. It is also important to point out that the corresponding convergence theorems for the elastic case using the NIPG formulation are found in Rivière & Wheeler (2001). Theorem 2.3.3 shows that SIPG has optimal convergence in the energy and L^2 norms, whereas theorem 2.3.2 shows that NIPG is optimal in the energy norm and suboptimal in the L^2 norm.

2.3.2 Elastic Formulation

The interior-penalty weak formulation of the elastic wave equation is given by the following statement: Find $\boldsymbol{u} \in \boldsymbol{X}^D = \left\{\varphi \mid \varphi \in \boldsymbol{H}^1(E)\ \forall\ E \in \Omega_h,\ \boldsymbol{\varphi} = 0 \text{ on } \Gamma_D\right\}$ such that for all $\boldsymbol{v} \in \boldsymbol{X}^D$

$$\sum_{E\in\Omega_h} \Big((\rho\partial_{tt}\boldsymbol{u}, \boldsymbol{v})_E + \boldsymbol{B}_E(\boldsymbol{u}, \boldsymbol{v}) \Big) + \sum_{\gamma\in\Gamma_h} \boldsymbol{J}_\gamma(\boldsymbol{u}, \boldsymbol{v}; S, R) = \sum_{E\in\Omega_h} (\boldsymbol{f}, \boldsymbol{v})_E \quad (2.3.18)$$

where $\boldsymbol{v}$ is a vector test function,

$$(\boldsymbol{u}, \boldsymbol{v})_E = \int_E \boldsymbol{u}\cdot\boldsymbol{v}\ dx\ dz, \quad (2.3.19)$$

$$\boldsymbol{B}_E(\boldsymbol{u}, \boldsymbol{v}) = \int_E \Big(\lambda\nabla\cdot\boldsymbol{u}\nabla\cdot\boldsymbol{v} + \mu(\nabla\boldsymbol{u} + \nabla\boldsymbol{u}^T) : \nabla\boldsymbol{v}\Big)\ dx\ dz, \quad (2.3.20)$$

$$\begin{aligned}\boldsymbol{J}_\gamma(\boldsymbol{u}, \boldsymbol{v}; S, R) &= -\int_\gamma \{\tau_i(\boldsymbol{u})\}[v_i]\ d\gamma + S\int_\gamma \{\tau_i(\boldsymbol{v})\}[u_i]\ d\gamma \\ &+ R\int_\gamma \{\lambda + 2\mu\}[\boldsymbol{u}]\cdot[\boldsymbol{v}]\ d\gamma,\end{aligned} \quad (2.3.21)$$

and τ_i is the traction vector, given in the isotropic case by

$$\tau_i(\boldsymbol{u}) = \sigma_{ij}(\boldsymbol{u})n_j = \lambda u_{k,k}n_i + \mu(u_{i,j} + u_{j,i})n_j. \quad (2.3.22)$$

The parameters R and S in eq. (2.3.21) are defined as in eq. (2.3.3). The equivalence of the above formulation with eq. (2.1.8) is stated without proof in the following proposition, the proof is similar to that of Prop. 2.3.1.

Proposition 2.3.4. *(i) If* $\boldsymbol{u}$ *is a solution to eq.* (2.1.8)*, then it is also a solution to eq.* (2.3.18)*; (ii) If* $\boldsymbol{u}$ *is a solution to eq.* (2.3.18) *and* $\boldsymbol{u} \in \boldsymbol{H}^2(\Omega)$*, then it is also a solution to eq.* (2.1.8)*.*

Introducing the subspace $\boldsymbol{X}_h^D = X_h^D \times X_h^D \subset \boldsymbol{X}^D$ and substituting in eq. (2.3.18) the test function and the displacement by linear combinations of the basis functions, yields a system of ordinary differential equations like the one in eqs. (2.2.11) and (2.2.12), where

$$M_{ij} = \sum_{E\in\Omega_h} (\rho\varphi_i, \varphi_j)_E \tag{2.3.23}$$

$$K_{ij}^1 = \sum_{E\in\Omega_h} \boldsymbol{B}_E\big((\varphi_i,0)^T,(\varphi_j,0)^T\big) + \sum_{\gamma\in\Gamma_h} \boldsymbol{J}_\gamma\big((\varphi_i,0)^T,(\varphi_j,0)^T\big) \tag{2.3.24}$$

$$K_{ij}^2 = \sum_{E\in\Omega_h} \boldsymbol{B}_E\big((0,\varphi_i)^T,(\varphi_j,0)^T\big) + \sum_{\gamma\in\Gamma_h} \boldsymbol{J}_\gamma\big((0,\varphi_i)^T,(\varphi_j,0)^T\big) \tag{2.3.25}$$

$$K_{ij}^3 = \sum_{E\in\Omega_h} \boldsymbol{B}_E\big((\varphi_i,0)^T,(0,\varphi_j)^T\big) + \sum_{\gamma\in\Gamma_h} \boldsymbol{J}_\gamma\big((\varphi_i,0)^T,(0,\varphi_j)^T\big) \tag{2.3.26}$$

$$K_{ij}^4 = \sum_{E\in\Omega_h} \boldsymbol{B}_E\big((0,\varphi_i)^T,(0,\varphi_j)^T\big) + \sum_{\gamma\in\Gamma_h} \boldsymbol{J}_\gamma\big((0,\varphi_i)^T,(0,\varphi_j)^T\big) \tag{2.3.27}$$

$$F_i^x = \sum_{E\in\Omega_h} (f_x, \varphi_i)_E, \tag{2.3.28}$$

$$F_i^z = \sum_{E\in\Omega_h} (f_z, \varphi_i)_E. \tag{2.3.29}$$

2.3.3 Basis Functions

A general description of the basis functions can be found in classical finite element literature, *e.g.* Hughes (2000). The nodal and modal basis functions for higher-order methods are described in detail in Karniadakis & Sherwin (1999). The above references deal with basis functions for FEM and therefore define the basis functions to be continuous across the entire domain. A description of the basis functions used in DGM can be found in Li (2006). An important difference between

FEM and DGM is that in DGM the basis functions are not required to be continuous over the entire domain but only inside the elements. In general, all the basis functions used in FEM can be used in DGM with simplifications, since they can be defined here locally on each element. This important feature of DGM implies that the mass matrix is always block-diagonal, which translates in to an efficient time-marching algorithm. Furthermore, the basis functions can be chosen such that the mass matrix is exactly diagonal. This is a desirable property because it is necessary to invert the mass matrix. In the following, the attention will be restricted to the tensor product basis functions in quadrilateral elements that yield a diagonal mass matrix. The degree of the basis functions in one side of the element will be denoted as κ, and $m = (\kappa + 1)^2$ will be used to denote the total number of basis functions in the elements.

The first approach to obtain a diagonal mass matrix is to use tensor products of the Legendre polynomials as the basis functions. The Legendre polynomials are given by the eigenfunctions of the following Sturm-Louville problem:

$$\frac{d}{dx}\left((1-x)(1+x)\frac{d}{dx}y(x)\right) = \lambda y(x) \quad x \in (-1,1), \tag{2.3.30}$$

and are usually denoted as P_n. The Legendre polynomials up to degree 3 are shown in Fig. 2.2a. These are called modal basis functions (Dubiner, 1991; Karniadakis & Sherwin, 1999), and it is the traditional approach that has been used in DGM when a diagonal mass matrix is sought (Cockburn & Shu, 1989; Cockburn et al., 1989; Li, 2006). They are orthogonal under the L^2 inner product and have simple recursion formulas for the higher order polynomials and their derivatives. The first two Legendre polynomials are given by $P_0(x) = 1$ and $P_1(x) = x$, and the higher order Legendre polynomials satisfy the recurrence relations

$$(n+1)P_{n+1}(x) = (2n+1)xP_n(x) - nP_{n-1}(x), \quad n \geq 1 \tag{2.3.31}$$

$$(x^2-1)P_n'(x) = nxP_n(x) - nP_{n-1}(x), \quad n \geq 1. \tag{2.3.32}$$

It should be noted that this approach yields a diagonal mass matrix only if the media parameters are constant inside each element, and that the condition number of the mass matrix is greater than $4\kappa^2$ in the 2D case (see Appendix 3).

A second approach is to use nodal basis functions, making the nodes inside the element match the quadrature points. This idea has been exploited in SEM, where the Gauss-Lobatto-Legendre (GLL) points and quadrature rules are used to impose the continuity of the basis functions at the element boundaries (see sec. 2.2.3). The third degree Lagrange polynomials using the GLL nodes are shown in Fig. 2.2b. This approach leads to a diagonal mass matrix independently of how the media parameters change inside the elements, but the mass matrix integrals are not computed exactly even if the media parameters are piece-wise constant.

The third approach is closely related to the second one, but uses the Gauss nodes and quadrature rules instead of the GLL nodes and quadrature rules. The Lagrange polynomials using these nodes are shown in Fig. 2.2c. The primary difference between the Gauss and the GLL nodes is that the endpoints of the interval are always included in the GLL nodes. We can use the Gauss nodes in DGM to define the basis functions because, unlike in FEM, the basis functions do not have to be continuous across the elements. In this approach, as well as in the second one, the mass matrix is always diagonal but, unlike in the second approach, the integration will be exact for piece-wise constant and piece-wise linearly varying media parameters.

2.4 Time Stepping

In the previous sections, the discretizations in space of the acoustic and elastic wave equations were given using FEM and IP-DGM. Clearly the time derivative needs to be discretized also in an implementation of these methods. As for the dis-

(a) Legendre

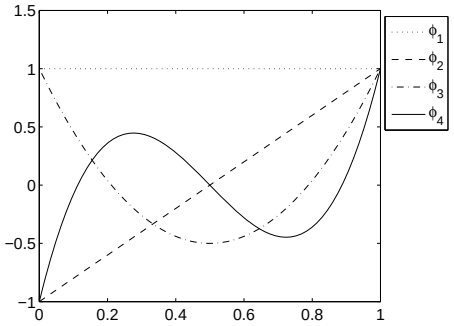

(b) GLL

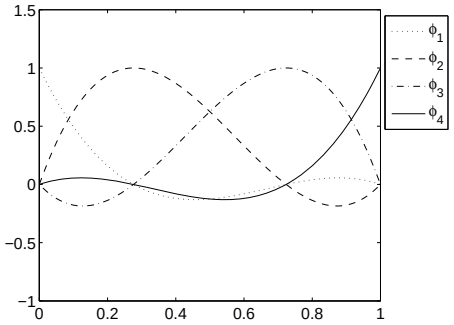

(c) Gauss

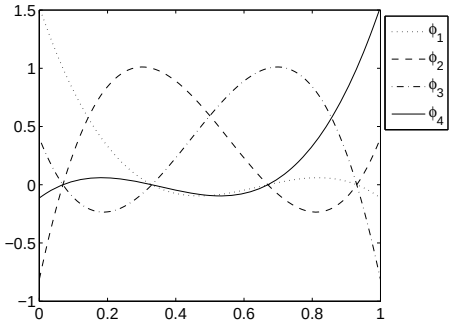

Figure 2.2: 1D Basis functions. (a) Legendre polynomials, (b) Lagrange polynomials using the GLL nodes, (c) Lagrange polynomials using the Gauss nodes.

cretization in space, there exist several strategies for the discretization of the time derivative. Three strategies will be considered here ranging from the most popular to the state of the art, namely the Newmark, Runge-Kutta and Lax-Wendroff methods. These strategies are applicable to either FEM or IP-DGM and to the acoustic or elastic formulations. The following notation will be used for the linear system in order to emphasize the generality of the strategies:

$$\begin{aligned} \mathbf{A}\partial_{tt}\mathbf{x} &= -\mathbf{B}\mathbf{x} + \mathbf{f}, \\ \mathbf{x}(0) &= \mathbf{x}^0, \\ \partial_t\mathbf{x}(0) &= \mathbf{v}^0, \end{aligned} \tag{2.4.1}$$

where, in the acoustic case, $\mathbf{x}$ contains the coefficients of the pressure fields, $\mathbf{A}$ is the mass matrix as defined in eqs. (2.2.5) or (2.3.9), and $\mathbf{B}$ is the stiffness matrix as defined in eqs. (2.2.6) or (2.3.10). In the elastic case, $\mathbf{x}$ contains the coefficients of the two components of displacement, and $\mathbf{A}$ and $\mathbf{B}$ are the block matrices given by

$$\mathbf{A} = \begin{pmatrix} \boldsymbol{M} & \boldsymbol{0} \\ \boldsymbol{0} & \boldsymbol{M} \end{pmatrix}, \tag{2.4.2}$$

$$\mathbf{B} = \begin{pmatrix} \boldsymbol{K}^1 & \boldsymbol{K}^2 \\ \boldsymbol{K}^3 & \boldsymbol{K}^4 \end{pmatrix}, \tag{2.4.3}$$

where $\boldsymbol{M}$ and $\boldsymbol{K}^i, i = 1, \ldots, 4$, are the mass and stiffness matrices as defined in eqs. (2.2.13)–(2.2.17) or (2.3.23)–(2.3.27).

The system (2.4.1) can be written as a first order system as follows

$$\begin{aligned} \partial_t\mathbf{y} &= \mathbf{C}\mathbf{y} + \mathbf{g}, \\ \mathbf{y}(0) &= \mathbf{y}^0, \end{aligned} \tag{2.4.4}$$

where

$$\mathbf{C} = \begin{pmatrix} \mathbf{0} & \mathbf{I} \\ -\mathbf{A}^{-1}\mathbf{B} & \mathbf{0} \end{pmatrix}, \tag{2.4.5}$$

$$\mathbf{g} = \begin{pmatrix} \mathbf{0} \\ \mathbf{A}^{-1}\mathbf{f} \end{pmatrix}, \tag{2.4.6}$$

$$\mathbf{y} = \begin{pmatrix} \mathbf{x} \\ \partial_t \mathbf{x} \end{pmatrix}, \tag{2.4.7}$$

$$\mathbf{y}^0 = \begin{pmatrix} \mathbf{x}^0 \\ \mathbf{v}^0 \end{pmatrix}. \tag{2.4.8}$$

Note that there may be many ways of writting the second order system as a first order system. The system in eq. (2.4.4) is known as the velocity-displacement formulation. A more common way of writting the first order system is the so-called velocity-stress formulation, it's main disadvantage is that it requires more degrees of freedom and will not be considered here for that reason. The following describes the application of the time stepping methods to either eq. (2.4.1) or (2.4.4), and the applicability to the case when there is a first order time derivative in eq. (2.4.1).[1]

2.4.1 Newmark Method

The classical approach to solve a second-order initial value problem is to use the Newmark method (Hughes, 2000). For the system (2.4.1), it is given by the following iterative scheme

$$\begin{aligned} (\mathbf{A} + \Delta t \delta_1 \mathbf{B})\mathbf{x}^{n+1} &= \left[2\mathbf{A} - \Delta t^2 \Big(\frac{1}{2} - 2\delta_1 + \delta_2\Big)\mathbf{B}\right]\mathbf{x}^n \\ &+ \left[\mathbf{A} - \Delta t^2 \Big(\frac{1}{2} + \delta_1 - \delta_2\Big)\mathbf{B}\right]\mathbf{x}^{n-1} \\ &+ \Delta t^2 \left[\delta_1 \mathbf{f}^{n+1} + \Big(\frac{1}{2} - 2\delta_1 + \delta_2\Big)\mathbf{f}^n + \Big(\frac{1}{2} + \delta_1 - \delta_2\Big)\mathbf{f}^{n-1}\right], \end{aligned} \tag{2.4.9}$$

[1] This situation may rise in practical applications, for example, for certain types of absorbing boundary conditions or when modeling fluid-solid internal boundary conditions.

for $n \geq 1$, and

$$
\begin{aligned}
(\mathbf{A} + \Delta t \delta_1 \mathbf{B})\mathbf{x}^1 &= \left[\mathbf{A} - \Delta t^2 \Big(\frac{1}{2} - 2\delta_1 + \delta_2\Big)\mathbf{B}\right]\mathbf{x}^0 + \Delta t \mathbf{A}\mathbf{v}^0 \\
&+ \Delta t^2 \left[\delta_1 \mathbf{f}^1 + \Big(\frac{1}{2} - \delta_1\Big)\mathbf{f}^0\right],
\end{aligned} \tag{2.4.10}
$$

where the time index is interpreted as $\mathbf{x}^n = \mathbf{x}(n\Delta t)$, and δ_1 and δ_2 are two free parameters that determine the accuracy and stability of the method.

The Finite Difference Method (FDM), also known as the leap-frog scheme, is obtained as a special case by setting $\delta_1 = 0$ and $\delta_2 = 1/2$. This is the most popular time-stepping scheme in seismic modeling (Komatitsch & Tromp, 1999; Chaljub et al., 2007; Cohen, 2002; Grote et al., 2006). The advantages are that it is second order accurate and it is explicit whenever the mass matrix is diagonal (which is often the case in seismic modeling). For this choice of parameters the scheme is conditionally stable, therefore the size of the time step needs to be bounded by a CFL condition. The stability conditions will be analyzed in the next chapter. This method is applicable when there is a first order time derivative, but the implementation becomes cumbersome mostly because the method is no longer explicit.

2.4.2 Runge-Kutta Method

The Runge-Kutta (RK) method is the most popular to advance the system in time when high-order accuracy is sought (Cockburn & Shu, 1989; Cockburn et al., 1989, 1990; Cockburn & Shu, 1998). It is applicable to the first order form, eq. (2.4.4). The system can be numerically solved in $k+1$ intermediate steps by

$$\mathbf{y}^{n,0} = \mathbf{y}^n, \tag{2.4.11}$$

$$\mathbf{y}^{n,m} = \sum_{i=0}^{m-1} \Big(\alpha_{m,i}\mathbf{y}^{n,i} + \beta_{m,i}\Delta t(\mathbf{C}\mathbf{y}^{n,i} + \mathbf{g})\Big) \quad m = 1, \ldots, k+1, \tag{2.4.12}$$

$$\mathbf{y}^{n+1} = \mathbf{y}^{n,k+1}, \tag{2.4.13}$$

where $\alpha_{m,i}$ and $\beta_{m,i}$ are free parameters that determine the accuracy and stability of the method, and the intermediate steps are indicated by the double upper index $\mathbf{y}^{n,m}$. The parameters $\alpha_{m,i}$ and $\beta_{m,i}$ for high-order accuracy can be found, for example, in Gottlieb (2005) and Kubatko et al. (2007). Since this method works with the first order system, it is applicable without modifications to the case when there is a first order time derivative. The main disadvantages of this method are the additional operations and memory required for the intermediate time steps.

2.4.3 Lax-Wendroff Method

The Lax-Wendroff method (LWM, Lax & Wendroff, 1964), aims to obtain formally a higher-order accuracy in time without demanding to save many time steps. It was introduced to seismic modeling by Dablain (1986) in the context of Finite Differences and later used by Cohen (2002) and Jund & Salmon (2007) in the context of SEM and by Käser & Dumbser (2006) in the context of DGM. This approach is based on a Taylor expansion in time of the wave field and a substitution of the time derivatives by matrix operations using eqs. (2.4.1) or (2.4.4).

Second Order Systems

The application of the LWM to eq. (2.4.1) has been described in Dablain (1986) and Cohen (2002). It is interesting to note that this method usually bears other names when it is applied to second order systems, for example, in Cohen (2002) it is called the modified equation approach. Nevertheless, due to the important similarities to the original formulation, it is suitable to regard this as a LWM. The first part of this method is to obtain an expression that allows the substitution of the higher-order time derivatives by matrix operation, which is given by the following theorem.

Theorem 2.4.1. *The* $2k$th *order time derivative of* $\mathbf{x}$ *is given by*

$$\partial_t^{2k}\mathbf{x} = (-\mathbf{A}^{-1}\mathbf{B})^k\mathbf{x} + \sum_{l=0}^{k-1}(-\mathbf{A}^{-1}\mathbf{B})^l\mathbf{A}^{-1}\partial_t^{2(k-l-1)}\mathbf{f}. \tag{2.4.14}$$

Proof. Proceeding by induction, taking $k = 1$ yields exactly eq. (2.4.1). Taking now $k+1$ and using eqs. (2.4.1) and (2.4.14)

$$\begin{aligned}
\partial_t^{2k+2}\mathbf{x} &= \partial_t^2(\partial_t^{2k}\mathbf{x}) \\
&= \partial_t^2\left((-\mathbf{A}^{-1}\mathbf{B})^k\mathbf{x} + \sum_{l=0}^{k-1}(-\mathbf{A}^{-1}\mathbf{B})^l\mathbf{A}^{-1}\partial_t^{2(k-l-1)}\mathbf{f}\right) \\
&= (-\mathbf{A}^{-1}\mathbf{B})^k\partial_t^2\mathbf{x} + \sum_{l=0}^{k-1}(-\mathbf{A}^{-1}\mathbf{B})^l\mathbf{A}^{-1}\partial_t^{2(k-l)}\mathbf{f} \\
&= (-\mathbf{A}^{-1}\mathbf{B})^{k+1}\mathbf{x} + (-\mathbf{A}^{-1}\mathbf{B})^k\mathbf{A}^{-1}\mathbf{f} + \sum_{l=0}^{k-1}(-\mathbf{A}^{-1}\mathbf{B})^l\mathbf{A}^{-1}\partial_t^{2(k-l)}\mathbf{f} \\
&= (-\mathbf{A}^{-1}\mathbf{B})^{k+1}\mathbf{x} + \sum_{l=0}^{k}(-\mathbf{A}^{-1}\mathbf{B})^l\mathbf{A}^{-1}\partial_t^{2(k-l)}\mathbf{f},
\end{aligned}$$

which is eq. (2.4.14) for $k+1$. □

The second part of this method is to obtain a Taylor expansion for the time stepping. Evaluating the Taylor expansion of $\mathbf{x}$ at $t + \Delta t$ and $t - \Delta t$ yields

$$\mathbf{x}^{n+1} = \mathbf{x}^n + \Delta t\partial_t\mathbf{x}^n + \frac{\Delta t^2}{2}\partial_t^2\mathbf{x}^n + \frac{\Delta t^3}{3!}\partial_t^3\mathbf{x}^n + \dots \tag{2.4.15}$$

$$\mathbf{x}^{n-1} = \mathbf{x}^n - \Delta t\partial_t\mathbf{x}^n + \frac{\Delta t^2}{2}\partial_t^2\mathbf{x}^n - \frac{\Delta t^3}{3!}\partial_t^3\mathbf{x}^n + \dots \tag{2.4.16}$$

Upon addition of the above equations the odd-order terms mutually cancel, to obtain

$$\mathbf{x}^{n+1} - 2\mathbf{x}^n + \mathbf{x}^{n-1} = 2\sum_{k=1}^{N}\frac{\Delta t^{2k}}{2k!}\partial_t^{2k}\mathbf{x}^n + O(\Delta t^{2N}). \tag{2.4.17}$$

Note that the above equation requires only even-order derivatives. These can be substituted by matrix multiplications using eq. (2.4.14). Given $\mathbf{x}^n$ and $\mathbf{x}^{n-1}$, $\mathbf{x}^{n+1}$

can be readily calculated using eq. (2.4.17). These procedures include the FDM as the special case when $N = 1$, therefore in this sense it is a higher-order generalization of the FDM. The stability of this method will be considered in the next chapter. The limitation of this approach is that it cannot be directly applied when there is a first-order time derivative. If that is the case, a similar approach can be developed for the first-order system as described below.

First Order Systems

This is the original formulation of the LWM. It has been called the *Arbitrary High Order Derivatives* (ADER) method in Schwartzkopff et al. (2001, 2002, 2004) and applied to seismic wave propagation in Dumbser & Munz (2006); Käser & Dumbser (2006); Dumbser & Käser (2006); de la Puente et al. (2007); Dumbser et al. (2007b,a); Käser et al. (2007a,b) and Jund & Salmon (2007). This method is based on the Cauchy-Kovalewski procedure, which confers the method the ability to get the same order of accuracy in space and in time, and it is stated as follows.

Theorem 2.4.2. *(Cauchy-Kovalewski) The kth order time derivative of* $\mathbf{y}$ *is given by*

$$\partial_t^k \mathbf{y} = \mathbf{C}^k \mathbf{y} + \sum_{l=0}^{k-1} \mathbf{C}^l \partial_t^{2(k-l-1)} \mathbf{g}. \tag{2.4.18}$$

The proof is closely related to that of Theorem 2.4.1. Using eq. (2.4.18), the time derivatives can be substituted by matrix operations in the following Taylor expansion

$$\mathbf{y}(t + \Delta t) = \sum_{k=0}^{N} \frac{\Delta t^k}{k!} \partial_t^k \mathbf{y}(t) + O(\Delta t^N). \tag{2.4.19}$$

The advantage of this approach is that it is applicable to systems when there is a first order time derivative term in eq. (2.4.1), but the disadvantage is that it

needs to include more terms in the Taylor expansion to attain the same accuracy than the Lax-Wendroff method for second order systems.

Chapter 3

Grid Dispersion and Stability

The grid dispersion and stability analyses are the most important analytical tools that help determine the simulation parameters for the numerical propagation of acoustic or elastic waves. This chapter presents the analyses of FEM and IP-DGM for acoustic and elastic wave propagation. Particular attention will be devoted to allow for non-equispaced nodes and high-order basis functions.

The analyses are based on the von Neumann method (Mitchell & Griffiths, 1980; Hughes, 2000), which assumes a plane wave propagating through the finite-element domain. It will be shown that the plane wave assumption leads to a generalized eigenvalue formulation that is originally large, proportional to the number of nodes in the finite element mesh, but with some assumptions, it can be reduced to a smaller one, proportional to the number of nodes inside one element.

Since the goal of these analyses is to derive the stability condition and grid-dispersion relations, to have a manageable set of parameters the analyses make several assumptions about the medium. The analyses assume that the medium is isotropic, homogeneous, unbounded and source free. Similar assumptions are always made whenever a plane wave analysis is sought; see for example Alford et al. (1974), Mullen & Belytschko (1982), Marfurt (1984), Hu et al. (1999), Cohen (2002), Ainsworth (2004a,b) and Ainsworth et al. (2006). In practice these assumptions are not expected to be satisfied, nevertheless the results from an analysis based on these assumptions can provide valuable information to determine the discretization

parameters for a numerical experiment. Furthermore, it will be assumed that the finite-element mesh is periodic, and that the elements are square with sides parallel to the coordinate axis and with tensor product basis functions; these are common assumptions when a finite element method is analyzed, see for example Marfurt (1984), Cohen (2002), Ainsworth (2004a,b) and Ainsworth et al. (2006). For convenience, these will be referred to as the *simplifying assumptions* and are summarized in Table 3.1.

The medium is assumed to be:	**The elements are assumed to be:**
Unbounded	Periodic
Homogeneous	Square
Isotropic	With sides parallel to coordinate axis
Source free	With tensor product basis functions

Table 3.1: Simplifying assumptions for the plane wave analysis.

3.1 Finite Element Method

3.1.1 Acoustic Case

This section derives grid-dispersion relations for the acoustic FEM of any order. The approach is based on a generalized eigenvalue problem that can be reduced to order κ^2 using the assumptions in Table 3.1. It is a generalization of the analysis found in Cohen (2002), where only the SEM was considered. It will be shown that the eigenvalues of the order κ^2 problem can be decomposed as combinations of the eigenvalues of two order κ problems (Cohen, 2002), making the computation more efficient. Unfortunately closed form grid-dispersion relations are not given except for low-order elements, and in general the grid dispersion needs to be computed numerically for each wavenumber and sampling ratio.

3.1.1.1 The Eigenvalue Problem

Introducing the simplifying assumptions of the media from Table 3.1 in eq. (2.2.4) yields

$$\mathcal{M}_{ij}\partial_{tt}P_j + \mathcal{K}_{ij}P_j = 0, \tag{3.1.1}$$

where

$$\mathcal{M}_{ij} = \int_\Omega \phi_i\phi_j \, dx \, dz, \tag{3.1.2}$$

$$\mathcal{K}_{ij} = \alpha^2 \int_\Omega \nabla\phi_i \cdot \nabla\phi_j \, dx \, dz, \tag{3.1.3}$$

and $\alpha = \sqrt{\lambda/\rho}$ is the velocity of the acoustic wave. Using the assumptions on the finite-element mesh, the elements in the domain are square with sides h. Note that with this assumption $x_n = h(i+\xi_j)$ and $z_n = h(i+\xi_j)$ with $n = \kappa i + j$ and $0 \leq j < \kappa$; thus the nodes are κ-periodic in both directions, $x_{n+\kappa} = x_n + h$ and $z_{n+\kappa} = z_n + h$. Recall from section 2.2.3 that the ξ_j represent the node distribution in one side of the element, and that $\xi_0 = 0$ and $\xi_\kappa = 1$. Using the plane wave assumption, P_j has the following form (no summation over j)

$$P_j(t) = A_j e^{\mathrm{i}(\boldsymbol{k}\cdot\boldsymbol{x}_j - \omega t)}, \tag{3.1.4}$$

where $\boldsymbol{k}$ is the wavenumber, $\boldsymbol{x}_j$ contains the jth node coordinates and A_j is an arbitrary constant. Note that eq. (3.1.4) represents a plane wave evaluated at the jth node. Substituting eq. (3.1.4) in eq. (3.1.1) yields the following generalized eigenvalue problem

$$\Lambda\mathcal{M}_{ij}P_j = \mathcal{K}_{ij}P_j. \tag{3.1.5}$$

The matrix $\mathcal{M}_{ij}$ is well known from the finite-element literature to be symmetric positive definite, and $\mathcal{K}_{ij}$ is known to be symmetric positive semidefinite (Brenner & Scott, 2002) and thus all the eigenvalues are real and positive (Watkins, 2002). The

eigenvalues of the above equation have the form $\Lambda = \omega_h^2$, where ω_h is the angular frequency at which the wave travels in the grid. The eigenvalues will take a different form if the time derivative is discretized, for example, for the finite-difference in time case, the eigenvalues have the form $\Lambda = 4\Delta t^{-2}\sin^2(\omega_h \Delta t/2)$. These definitions will be used after solving for the eigenvalues to obtain the grid-dispersion relations.

The size of the eigenvalue problem (3.1.5) depends on the total number of nodes. I will not attempt to solve for the eigenvalues of eq. (3.1.5) to get the grid dispersion since that would be an intractable problem in an unbounded domain. Instead I will use the assumptions previously given to reduce the order of the problem. In order to do this, first note that in a regular grid using tensor product elements with $\kappa+1$ nodes per element in each direction there are only κ^2 classes of degrees of freedom, as shown in Fig. 2.1 (Marfurt, 1984; Cohen, 2002); thus there are only κ^2 distinct eigenvalues.

To derive an eigenvalue equation of order κ^2, let us write $\mathcal{M}_{ij}$ and $\mathcal{K}_{ij}$ as fourth-order tensors using the definitions of the mass and stiffness matrices, eqs. (3.1.2) and (3.1.3), and the definition of the basis functions, eq. (2.2.20):

$$\begin{aligned}
\mathcal{M}_{ij} &= \int_\Omega \phi_i(x,z)\phi_j(x,z)\,dx\,dz = \int_\Omega \varphi_{m_1}(x)\varphi_{m_2}(z)\varphi_{n_1}(x)\varphi_{n_2}(z)\,dx\,dz \\
&= M_{m_1 m_2 n_1 n_2}, \qquad (3.1.6)\\
\mathcal{K}_{ij} &= \alpha^2 \int_\Omega \nabla\phi_i \cdot \nabla\phi_j\,dx\,dz \\
&= \alpha^2 \int_\Omega \nabla(\varphi_{m_1}(x)\varphi_{m_2}(z)) \cdot \nabla(\varphi_{n_1}(x)\varphi_{n_2}(z))\,dx\,dz \\
&= K_{m_1 m_2 n_1 n_2}, \qquad (3.1.7)
\end{aligned}$$

with $i = (\kappa+1)m_2 + m_1$ and $j = (\kappa+1)n_2 + n_1$. Also, P_j can be written as a second-order tensor by changing the index to $j = (\kappa+1)n_2 + n_1$ to get (no summation over n_1 and n_2)

$$P_j = P_{n_1 n_2} = A_{n_1 n_2} e^{\mathrm{i}(k_x x_{n_1} + k_z z_{n_2} - \omega t)}. \qquad (3.1.8)$$

Furthermore, since the nodes are κ-periodic in both directions, the constants $A_{n_1 n_2}$ are also κ-periodic, and thus

$$A_{n_1 n_2} = A_{(\kappa q_1 + l_1)(\kappa q_2 + l_2)} = A_{l_1 l_2}, \tag{3.1.9}$$

with $n_1 = \kappa q_1 + l_1$, $n_2 = \kappa q_2 + l_2$, and $0 \leq l_1, l_2 < \kappa$. Substituting eqs. (3.1.6), (3.1.8) and (3.1.9) in the left-hand side of eq. (3.1.5) yields

$$\begin{aligned} M_{m_1 m_2 n_1 n_2} P_{n_1 n_2} &= M_{m_1 m_2 n_1 n_2} A_{n_1 n_2} e^{\mathrm{i}(k_x x_{n_1} + k_z z_{n_2} - \omega t)} \\ &= M_{m_1 m_2 (\kappa q_1 + l_1)(\kappa q_2 + l_2)} e^{\mathrm{i}(k_x h q_1 + k_z h q_2)} A_{l_1 l_2} e^{\mathrm{i}(k_x h \xi_{l_1} + k_z h \xi_{l_2} - \omega t)} \\ &= \widetilde{M}_{m_1 m_2 l_1 l_2}(k_x, k_z) \widetilde{A}_{l_1 l_2}(k_x, k_z) e^{-\mathrm{i}\omega t}\,, \end{aligned} \tag{3.1.10}$$

and similarly, substituting eqs. (3.1.7), (3.1.8) and (3.1.9) on the right-hand side yields

$$K_{m_1 m_2 n_1 n_2} P_{n_1 n_2} = \widetilde{K}_{m_1 m_2 l_1 l_2}(k_x, k_z) \widetilde{A}_{l_1 l_2}(k_x, k_z) e^{-\mathrm{i}\omega t}\,, \tag{3.1.11}$$

where

$$\widetilde{M}_{m_1 m_2 l_1 l_2}(k_x, k_z) = M_{m_1 m_2 (\kappa q_1 + l_1)(\kappa q_2 + l_2)} e^{\mathrm{i}(k_x h q_1 + k_z h q_2)}, \tag{3.1.12}$$

$$\widetilde{K}_{m_1 m_2 l_1 l_2}(k_x, k_z) = K_{m_1 m_2 (\kappa q_1 + l_1)(\kappa q_2 + l_2)} e^{\mathrm{i}(k_x h q_1 + k_z h q_2)}, \quad \text{and} \tag{3.1.13}$$

$$\widetilde{A}_{l_1 l_2}(k_x, k_z) = A_{l_1 l_2} e^{\mathrm{i}(k_x h \xi_{l_1} + k_z h \xi_{l_2})}. \tag{3.1.14}$$

Note that a summation is implied over q_1 and q_2 (but not on l_1 and l_2), and that the summations are always finite, even in an unbounded domain, because the mass and stiffness matrices are sparse.

Substituting eqs. (3.1.10) and (3.1.11) in eq. (3.1.5) and eliminating the $e^{-\mathrm{i}\omega t}$ factor yields the following reduced-order eigenvalue equation:

$$\Lambda \widetilde{M}_{m_1 m_2 l_1 l_2} \widetilde{A}_{l_1 l_2} = \widetilde{K}_{m_1 m_2 l_1 l_2} \widetilde{A}_{l_1 l_2}, \quad 0 \leq m_1, m_2 < \kappa. \tag{3.1.15}$$

The eigenvectors $\widetilde{A}_{l_1 l_2}$, as defined in eq. (3.1.14), are explicitly dependent on the node coordinates, but the eigenvalues depend on the grid nodes only in the sense that the nodes are used to compute the mass and stiffness matrices. *In practice this means that, to get the grid dispersion, the node's coordinates are used only to compute the integrals in eqs.* (3.1.2) *and* (3.1.3)*, thus avoiding the difficulty due to irregular node spacing.*

The above eigenvalue problem can be reduced to two eigenvalue problems of order κ each, as stated in the following theorem (compare to Theorem 4 in Cohen, 2002).

Theorem 3.1.1. *Let λ_x and λ_z be eigenvalues of*

$$\lambda_\eta \widetilde{M}^{1D}_{ij}(k_\eta)\widetilde{A}_j = \widetilde{K}^{1D}_{ij}(k_\eta)\widetilde{A}_j, \quad \eta = x, z. \tag{3.1.16}$$

Then the eigenvalues of eq. (3.1.15) *are given by $\Lambda = \lambda_x + \lambda_z$, where (summation is implied over l on the right-hand side)*

$$\widetilde{M}^{1D}_{mn}(k_\eta) = M^{1D}_{m(\kappa l+n)} e^{\mathrm{i}k_\eta h l}, \tag{3.1.17}$$

$$\widetilde{K}^{1D}_{mn}(k_\eta) = K^{1D}_{m(\kappa l+n)} e^{\mathrm{i}k_\eta h l}, \tag{3.1.18}$$

and M^{1D}_{mn} and K^{1D}_{mn} are the mass and stiffness matrices of the 1D problem given by

$$M^{1D}_{mn} = \int \varphi_m \varphi_n dx \quad \textit{and} \tag{3.1.19}$$

$$K^{1D}_{mn} = \alpha^2 \int \varphi'_m \varphi'_n dx. \tag{3.1.20}$$

Proof. Using the definition of the mass and stiffness matrices, for tensor-product rectangular elements and for a regular mesh, the mass and stiffness matrices for the 2D case can be written in terms of the corresponding 1D matrices. Starting from

the definition of the mass matrix, eq. (3.1.6), it can be written as

$$\begin{aligned} M_{m_1m_2n_1n_2} &= \int_\Omega \varphi_{m_1}(x)\varphi_{m_2}(z)\varphi_{n_1}(x)\varphi_{n_2}(z)\,dx\,dz \\ &= \int_\Omega \varphi_{m_1}(x)\varphi_{n_1}(x)\,dx \int_\Omega \varphi_{m_2}(z)\varphi_{n_2}(z)\,dz \\ &= M^{1D}_{m_1n_1} M^{1D}_{m_2n_2}. \end{aligned} \tag{3.1.21}$$

Similarly, from the definition of the stiffness matrix, eq. (3.1.7), it can be written as

$$\begin{aligned} K_{m_1m_2n_1n_2} &= \alpha^2 \int_\Omega \nabla\big(\varphi_{m_1}(x)\varphi_{m_2}(z)\big)\cdot\nabla\big(\varphi_{n_1}(x)\varphi_{n_2}(z)\big)\,dx\,dz \\ &= \alpha^2 \int_\Omega \varphi'_{m_1}(x)\varphi'_{n_1}(x)\,dx \int_\Omega \varphi_{m_2}(z)\varphi_{n_2}(z)\,dz \\ &+ \alpha^2 \int_\Omega \varphi_{m_1}(x)\varphi_{n_1}(x)\,dx \int_\Omega \varphi'_{m_2}(z)\varphi'_{n_2}(z)\,dz \\ &= K^{1D}_{m_1n_1} M^{1D}_{m_2n_2} + K^{1D}_{m_2n_2} M^{1D}_{m_1n_1}. \end{aligned} \tag{3.1.22}$$

These decompositions of the mass and stiffness matrices yields a similar decomposition for the dynamic mass and stiffness matrices. Substituting the mass matrix decomposition in eq. (3.1.12) yields

$$\begin{aligned} \widetilde{M}_{m_1m_2l_1l_2}(k_x,k_z) &= M^{1D}_{m_1(\kappa q_1+l_1)} e^{\mathrm{i}k_x h q_1} M^{1D}_{m_2(\kappa q_2+l_2)} e^{\mathrm{i}k_z h q_2} \\ &= \widetilde{M}^{1D}_{m_1l_1}(k_x)\widetilde{M}^{1D}_{m_2l_2}(k_z). \end{aligned} \tag{3.1.23}$$

Substituting the stiffness-matrix decomposition in eq. (3.1.13) yields

$$\begin{aligned} \widetilde{K}_{m_1m_2l_1l_2}(k_x,k_z) &= K^{1D}_{m_1(\kappa q_1+l_1)} e^{\mathrm{i}k_x h q_1} M^{1D}_{m_2(\kappa q_2+l_2)} e^{\mathrm{i}k_z h q_2} \\ &+ K^{1D}_{m_2(\kappa q_2+l_2)} e^{\mathrm{i}k_z h q_2} M^{1D}_{m_1(\kappa q_1+l_1)} e^{\mathrm{i}k_x h q_1} \\ &= \widetilde{K}^{1D}_{m_1l_1}(k_x)\widetilde{M}^{1D}_{m_2l_2}(k_z) + \widetilde{K}^{1D}_{m_2l_2}(k_z)\widetilde{M}^{1D}_{m_1l_1}(k_x). \end{aligned} \tag{3.1.24}$$

Substituting the second-degree tensor $B_{kl} = A^{(1)}_k A^{(2)}_l$ and the decomposition of the

stiffness matrix in the right-hand side of eq. (3.1.15) yields

$$\begin{aligned}
\widetilde{K}_{ijkl}B_{kl} &= \left(\widetilde{K}^{1D}_{ik}(k_x)\widetilde{M}^{1D}_{jl}(k_z) + \widetilde{K}^{1D}_{jl}(k_z)\widetilde{M}^{1D}_{ik}(k_x)\right) A^{(1)}_k A^{(2)}_l \\
&= \lambda_x \widetilde{M}^{1D}_{ik}(k_x)\widetilde{M}^{1D}_{jl}(k_z)A^{(1)}_k A^{(2)}_l + \lambda_z \widetilde{M}^{1D}_{jl}(k_z)\widetilde{M}^{1D}_{ik}(k_x)A^{(1)}_k A^{(2)}_l \\
&= (\lambda_x + \lambda_z)\,\widetilde{M}_{ijkl}B_{kl}, \qquad (3.1.25)
\end{aligned}$$

therefore $\Lambda = \lambda_x + \lambda_z$ is an eigenvalue of eq. (3.1.15), with corresponding eigenvector B_{kl}. It can be easily shown by contradiction that all the eigenvalues of eq. (3.1.15) can be expressed as a combination of the eigenvalues of the 1D problems by noting that all the possible combinations are κ^2, exactly the number of eigenvalues of eq. (3.1.15). □

As the degree of the polynomials gets higher it becomes impractical to derive an explicit grid-dispersion relation, but the κ eigenvalues of the 1D problem can always be obtained numerically in each direction to compute the grid dispersion. In seismic modeling there is only one eigenvalue with physical meaning; all the other eigenvalues correspond to non-physical, or spurious, modes. In the 1D case it has been shown that the non-physical modes have a negligible effect in the solution (Mulder, 1999; Cohen, 2002); it is reasonable to expect the same behavior on higher dimensions but I am not aware of a proof. I have found through numerical experiments that the eigenvalue that corresponds to the acoustic wave is the smallest one. Further research is needed to ascertain this hypothesis.

3.1.1.2 Procedure to Calculate the Grid Dispersion

To obtain the grid dispersion, let us first consider the eigenvalues of eq. (3.1.15) for the case $\alpha = 1$ and $h = 1$. The definition of the mass and stiffness matrices immediately yield

$$\widetilde{M}_{m_1 m_2 l_1 l_2} = h\widetilde{M}'_{m_1 m_2 l_1 l_2} \quad \text{and} \quad \widetilde{K}_{m_1 m_2 l_1 l_2} = \frac{\alpha^2}{h}\widetilde{K}'_{m_1 m_2 l_1 l_2}, \qquad (3.1.26)$$

where $\widetilde{M}'_{m_1m_2l_1l_2}$ and $\widetilde{K}'_{m_1m_2l_1l_2}$ are computed using $\alpha = 1$ and $h = 1$. Let Λ' be an eigenvalue of

$$\Lambda'\widetilde{M}'_{m_1m_2l_1l_2}\widetilde{A}_{l_1l_2} = \widetilde{K}'_{m_1m_2l_1l_2}\widetilde{A}_{l_1l_2}. \tag{3.1.27}$$

From eq. (3.1.26), Λ' is related to the eigenvalue Λ of eq. (3.1.15) by $\Lambda = \alpha^2\Lambda'/h^2$.

The grid-dispersion relations are given as follows. Let Λ' be the smallest eigenvalue of eq. (3.1.15) using $h = 1$ and $\alpha = 1$. Then the definition of the eigenvalues in the semi-discrete case yields $\omega_h = (\alpha/h)\sqrt{\Lambda'}$. Substituting $\omega_h = 2\pi\alpha_h\delta/h$ and multiplying by $h/(2\pi\alpha\delta)$ yields

$$\frac{\alpha_h}{\alpha} = \frac{1}{2\pi\delta}\sqrt{\Lambda'}, \tag{3.1.28}$$

where α_h is the velocity at which the wave travels in the grid, $\delta = h/(\kappa L)$ is the *average sampling ratio* in the element and L is the wavelength. Similarly, for the finite-difference in time case, the grid-dispersion relation is given by

$$\frac{\alpha_h}{\alpha} = \frac{1}{\pi\delta\ \mathrm{q}}\sin^{-1}\left(\frac{\mathrm{q}}{2}\sqrt{\Lambda'}\right). \tag{3.1.29}$$

The *grid-dispersion error* is defined as the relative difference between the physical velocity and the velocity at which the wave travels in the grid, and is given by

$$e_p = \frac{\alpha_h}{\alpha} - 1. \tag{3.1.30}$$

The procedure to derive the grid dispersion for a given degree, sampling ratio and wavenumber is summarized below:

1. Compute the 1D mass and stiffness matrices with eqs. (3.1.19) and (3.1.20) using $h = 1$ and $\alpha = 1$.
2. Compute $\widetilde{M}^{1D}_{mn}(k_x)$, $\widetilde{M}^{1D}_{mn}(k_z)$, $\widetilde{K}^{1D}_{mn}(k_x)$ and $\widetilde{K}^{1D}_{mn}(k_z)$ using eqs. (3.1.17) and (3.1.18).

3. Solve the eigenvalue problems $\lambda_\eta \widetilde{M}_{ij}^{1D}(k_\eta)\widetilde{A}_j = \widetilde{K}_{ij}^{1D}(k_\eta)\widetilde{A}_j$, $\eta = x, z$, and save the smallest eigenvalues; recall that the eigenvalue of the 2D problem is $\Lambda' = \lambda_x + \lambda_z$.

4. Calculate the grid dispersion using eq. (3.1.28) for the semi-discrete case or eq. (3.1.29) for the finite-difference in time case.

Grid-Dispersion Relations for the First-Degree Elements

Let us now derive explicitly the grid-dispersion relations for the lowest-degree FEM and SEM using finite differences in time. In the following I will refer to FEM-CM whenever equispaced nodes and exact integration is used (classical FEM), and to SEM whenever the GLL nodes and quadrature rules are used. For first-degree methods there is one degree of freedom; thus the eigenvalue problem can be trivially solved. For FEM, doing exact integration in eqs. (3.1.19) and (3.1.20), and substituting in eqs. (3.1.17) and (3.1.18) yields

$$\widetilde{M}^{1D}(k_\eta) = \frac{2+\cos(k_\eta h)}{3} \quad \text{and} \tag{3.1.31}$$

$$\widetilde{K}^{1D}(k_\eta) = 2 - 2\cos(k_\eta h). \tag{3.1.32}$$

Therefore the eigenvalue of the 2D problem is given by

$$\begin{aligned}\Lambda &= \frac{\widetilde{K}^{1D}(k_x)}{\widetilde{M}^{1D}(k_x)} + \frac{\widetilde{K}^{1D}(k_z)}{\widetilde{M}^{1D}(k_z)} \\ &= 6\frac{1-1\cos(k_x h)}{2+\cos(k_x h)} + 6\frac{1-1\cos(k_z h)}{2+\cos(k_z h)}.\end{aligned} \tag{3.1.33}$$

From this, the stability condition is given by $\mathrm{q} \leq 6^{-1/2}$, and the grid-dispersion relation is

$$\frac{\alpha_h}{\alpha} = \frac{1}{\pi\delta \mathrm{q}} \sin^{-1}\left(\mathrm{q}\sqrt{\frac{12 - 3\cos(k_x h) - 3\cos(k_z h) - 6\cos(k_x h)\cos(k_z h)}{8 + 4\cos(k_x h) + 4\cos(k_z h) + 2\cos(k_x h)\cos(k_z h)}}\right) \tag{3.1.34}$$

An equivalent equation but for the semi-discrete case was given in Mullen & Belytschko (1982) using a different approach.

In the SEM case, the trapezoidal rule of integration is used in eqs. (3.1.19) and (3.1.20). Substituting the results in eqs. (3.1.17) and (3.1.18) and solving for the eigenvalue yields

$$\Lambda = \frac{2\alpha^2}{h^2}\left(2 - \cos(k_x h) - \cos(k_z h)\right). \tag{3.1.35}$$

From this, the stability condition for this scheme is $\mathrm{q} \leq 2^{-1/2}$. Substituting this eigenvalue in eq. (3.1.29) yields the following grid-dispersion relation:

$$\frac{\alpha_h}{\alpha} = \frac{1}{\pi\delta \mathrm{q}} \sin^{-1}\left(\mathrm{q}\sqrt{\sin^2\left(\frac{k_x h}{2}\right) + \sin^2\left(\frac{k_z h}{2}\right)}\right), \tag{3.1.36}$$

which is the same as that for the acoustic FDM (Alford et al., 1974), as expected because the first-degree acoustic SEM is equivalent to the acoustic FDM (Cohen, 2002).

3.1.1.3 Results

This section presents the grid-dispersion curves for the acoustic FEM and SEM using the method presented above. It describes the effect that the stability parameter (q), the incidence angle (θ), the sampling ratio (δ), and the degree of the elements (κ) have in the grid dispersion.

Let us first consider the grid dispersion using the leap-frog scheme for time stepping, eq. (3.1.29). The grid-dispersion curves of the first-degree SEM, eq. (3.1.36), using $\mathrm{q} = 0.1$ and $\mathrm{q} = 0.7$ is shown in Fig. 3.1. As noted before, this scheme is equivalent to the acoustic FDM, therefore the same conclusions are drawn as those reported in Alford et al. (1974):

- the dispersion is greatest in the direction of any of the grid axes,

- the dispersion is smallest taking a time step close to the stability condition, and
- a minimum of 10 nodes per wavelength ($\delta = 0.1$) is recommended to achieve accurate results.

It is clearly advantageous to use higher-degree SEM, as concluded in Seriani & Priolo (1994), because not only the dispersion diminishes rapidly but also the anisotropy practically disappears in third- and higher-degree SEM (it is already small in second-degree SEM, see Fig. 3.2). Perhaps the most important advantage of using higher-degree SEM is that the sampling ratio can be decreased to 4–5 nodes per wavelength (Seriani & Priolo, 1994). Comparing Figs. 3.1b, 3.2a and 3.2b it can be concluded that, in contrast to first-degree SEM, using second-degree and above would introduce non-physical arrivals since the grid velocity is slightly increased with respect to the physical velocity; nevertheless, this increase in velocity is less than 1% for a sampling ratio of 4 nodes per wavelength in the second-degree method and much smaller in the higher-degree methods.

Approximately the same level of dispersion and anisotropy is observed using second-degree FEM (Fig. 3.3b) and second-degree SEM (Fig. 3.2a). Thus there is no loss of accuracy due to mass lumping. First-degree FEM (Fig. 3.3a) suffers from the same anisotropy and dispersion as first-degree SEM (Fig. 3.1b), with the difference that the waves are hastened instead of delayed, as noted in Mullen & Belytschko (1982). In both first-degree schemes, at least 10 nodes per wavelength are needed to obtain accurate results.

The following results are for the semidiscrete case, eq. (3.1.28). The convergence of FEM and SEM methods with respect to the sampling ratio and the order of the elements is plotted in Figs. 3.4 and 3.5. Note from Figs. 3.4a and 3.4b that

the error introduced by the grid dispersion has the same order of convergence for FEM and SEM, and that the order is $O(h^{2\kappa})$. This super-convergent behavior of the grid dispersion of SEM was noted in Cohen (2002). In Fig. 3.5 SEM is compared with the popular row-sum mass-lumping method and the consistent mass FEM. It is clear from the figure that the row-sum mass-lumping method is unsuitable for high-degree methods (the accuracy of this method will be further discussed in section 3.1.2.3). SEM reaches machine accuracy at $\kappa = 4$, after which point no further improvement is observed. FEM also reaches machine accuracy at $\kappa = 4$ but looses accuracy after that point. Finally, note that for a large κ, the SEM is superior to FEM, either with a consistent mass or mass lumped.

The numerical anisotropy introduced by the grid dispersion is shown in Fig. 3.6. Note that the waves are delayed in SEM, and hastened in FEM for all incidence angles. Also, the grid dispersion is minimum for an oblique incidence angle in both cases. In Fig. 3.6a, the grid dispersion has been exaggerated by a factor of 10 for visualization purposes, and the sampling ratio is $\delta = 0.1$. The grid dispersion is almost isotropic for the second-degree methods, as can be seen in Fig. 3.6b. In this figure the magnification factor is 500 and the sampling ratio is $\delta = 0.2$. The higher-degree methods have negligible anisotropy; their anisotropy curves (not shown) overlap the reference curve.

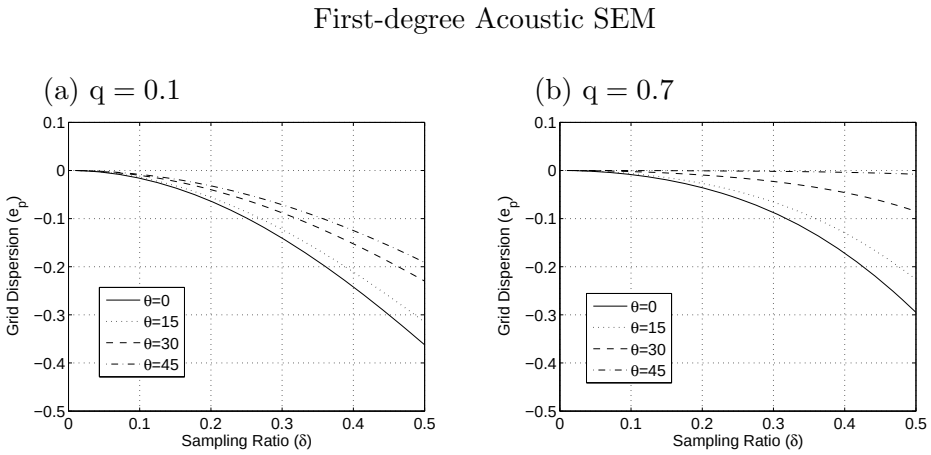

Figure 3.1: Grid dispersion of the acoustic FDM and first-degree SEM as a function of the sampling ratio (δ), eq. (3.1.36), with incidence angles of $\theta = 0°$, $15°$, $30°$ and $45°$ and (a) q = 0.1 and (b) q = 0.7. The dispersion is minimized for an oblique incidence angle and for a time step close to the stability condition.

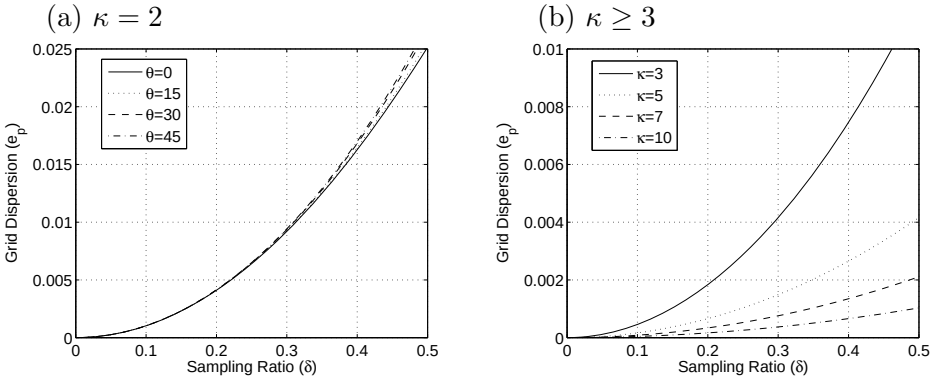

Figure 3.2: Grid dispersion of the acoustic SEM for second-degree and above, with q = 0.5. (a) Second-degree SEM (9-node elements, $\kappa = 2$). (b) $\kappa = 3, 5, 7, 10$. Note the small anisotropy of the second-degree scheme. For third degree and above the dispersion curves for different incidence angles are plotted on top of each other because they have negligible anisotropy.

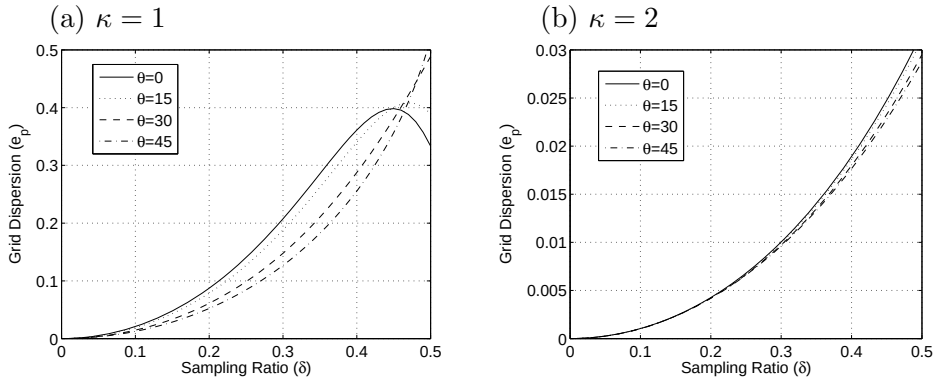

Figure 3.3: Grid dispersion of the acoustic FEM using q = 0.5. (a) First-degree FEM (4-node elements, eq. (3.1.34)), and (b) Second-degree FEM (9-node elements). The first-degree method has large and anisotropic dispersion. The second-degree FEM has a dispersion similar to the dispersion of the second-degree SEM, Fig. 3.2a, with the difference that for an oblique incidence angle the dispersion is the smallest.

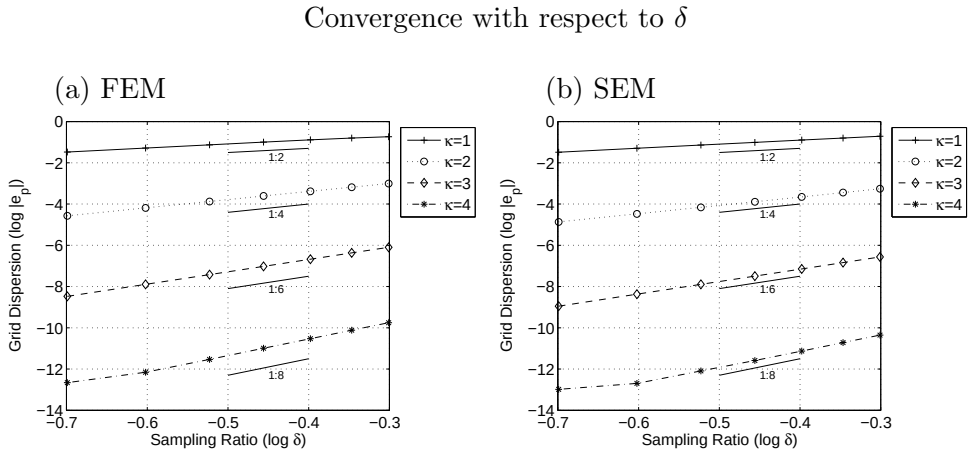

Figure 3.4: Convergence of the grid dispersion with respect to the sampling ratio in the semidiscrete case. (a) Convergence of FEM; (b) Convergence of SEM. The line segments indicate the slopes of the convergence curves. Note the super-convergence of the grid-dispersion error in both cases.

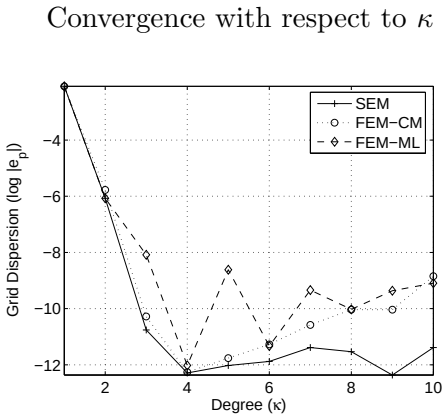

Figure 3.5: Convergence with respect to the degree of the elements of SEM, FEM with a consistent mass matrix (FEM-CM) and FEM with row-sum mass lumping (FEM-ML), semidiscrete case. Note the erratic convergence of FEM-ML.

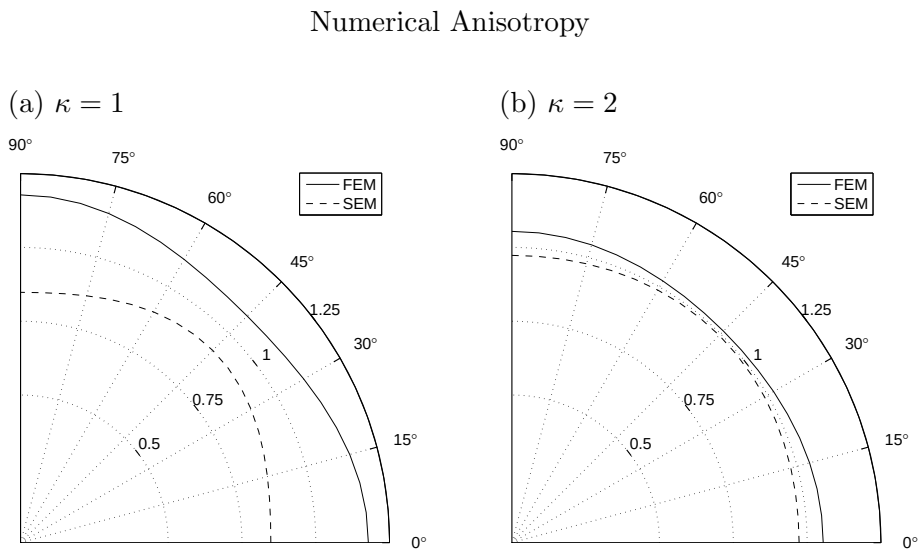

Figure 3.6: Numerical anisotropy introduced by the grid dispersion in FEM and SEM, semidiscrete case. The dispersion has been calculated for several wavelengths for visualization purposes. (a) Anisotropy of the first-degree methods for a propagation of 10 wavelengths, using $\delta = 0.1$; (b) Anisotropy of the second-degree methods for a propagation of 500 wavelengths, using $\delta = 0.2$.

3.1.2 Elastic Case

This section shows how to compute the grid dispersion of the elastic FEM. The approach is similar to the one used for the acoustic case. It is based on a generalized eigenvalue problem which can be reduced to order $2\kappa^2$ by using the simplifying assumptions. One difference is that here the eigenvalue problem can not be reduced to one of getting the eigenvalues of a 1D problem; nevertheless the $2\kappa^2$ eigenvalues can be computed numerically. A method to compute the grid dispersion and explicit grid-dispersion relations for first-degree SEM will be given at the end of this section.

3.1.2.1 The Eigenvalue Problem

Introducing the simplifying assumptions of Table 3.1 in eqs. (2.2.11) and (2.2.12) yields

$$\mathcal{M}_{ij}\partial_{tt}U_j^x + \mathcal{K}_{ij}^1 U_j^x + \mathcal{K}_{ij}^2 U_j^z = 0, \quad \text{and} \tag{3.1.37}$$

$$\mathcal{M}_{ij}\partial_{tt}U_j^z + \mathcal{K}_{ij}^3 U_j^x + \mathcal{K}_{ij}^4 U_j^z = 0, \tag{3.1.38}$$

where the matrices in the above equations are given by

$$\mathcal{M}_{ij} = \frac{r^2}{\alpha^2}\int_\Omega \phi_i\phi_j \, dx \, dz, \tag{3.1.39}$$

$$\mathcal{K}_{ij}^1 = r^2\int_\Omega \phi_{i,x}\phi_{j,x} \, dx \, dz + \int_\Omega \phi_{i,z}\phi_{j,z} \, dx \, dz, \tag{3.1.40}$$

$$\mathcal{K}_{ij}^2 = (r^2-1)\int_\Omega \phi_{i,x}\phi_{j,z} \, dx \, dz, \tag{3.1.41}$$

$$\mathcal{K}_{ij}^3 = K_{ji}^2, \tag{3.1.42}$$

$$\mathcal{K}_{ij}^4 = \int_\Omega \phi_{i,x}\phi_{j,x} \, dx \, dz + r^2\int_\Omega \phi_{i,z}\phi_{j,z} \, dx \, dz, \tag{3.1.43}$$

α is the P-wave velocity, β is the S-wave velocity and $r = \alpha/\beta$ is the P- to S-wave velocity ratio. These equations use the shorthand notation $\phi_{i,x} = \partial\phi_i/\partial x$ and $\phi_{i,z} = \partial\phi_i/\partial z$.

Assuming that the solution is a plane wave then U_j^x and U_j^z have the form (no summation over j)

$$U_j^x(t) = A_j e^{\mathrm{i}(\boldsymbol{k}\cdot\boldsymbol{x}_j - \omega t)} \quad \text{and} \quad U_j^z(t) = B_j e^{\mathrm{i}(\boldsymbol{k}\cdot\boldsymbol{x}_j - \omega t)}. \tag{3.1.44}$$

Recall that the nodes are defined the same way as in the acoustic case, but now there are two degrees of freedom at each one. Substituting in eqs. (3.1.37) and (3.1.38) yields

$$\Lambda \mathcal{M}_{ij} U_j^x = \mathcal{K}_{ij}^1 U_j^x + \mathcal{K}_{ij}^2 U_j^z \quad \text{and} \tag{3.1.45}$$

$$\Lambda \mathcal{M}_{ij} U_j^z = \mathcal{K}_{ij}^3 U_j^x + \mathcal{K}_{ij}^4 U_j^z, \tag{3.1.46}$$

where the eigenvalues are given by $\Lambda = \omega_h^2$. For the finite-difference in time case the eigenvalues take the form $\Lambda = 4\Delta t^{-2}\sin^2(\omega_h \Delta t/2)$. The above equations represent a generalized eigenvalue problem; this is clearly seen by writing

$$\Lambda \begin{bmatrix} \boldsymbol{M} & 0 \\ 0 & \boldsymbol{M} \end{bmatrix} \begin{bmatrix} \boldsymbol{U}^x \\ \boldsymbol{U}^z \end{bmatrix} = \begin{bmatrix} \boldsymbol{K}^1 & \boldsymbol{K}^2 \\ \boldsymbol{K}^3 & \boldsymbol{K}^4 \end{bmatrix} \begin{bmatrix} \boldsymbol{U}^x \\ \boldsymbol{U}^z \end{bmatrix}, \tag{3.1.47}$$

where $(\boldsymbol{M})_{ij} = \mathcal{M}_{ij}$, $(\boldsymbol{K}^l)_{ij} = \mathcal{K}_{ij}^l$, $(\boldsymbol{U}^x)_j = U_j^x$ and $(\boldsymbol{U}^z)_j = U_j^z$. It can be shown that the eigenvalues of the above system are real and positive, as stated in the following proposition.

Proposition 3.1.2. *The eigenvalues of eq.* (3.1.47) *are real and positive.*

Proof. It is sufficient to show that the matrix on the right-hand side is symmetric positive semidefinite and the one on the left-hand side is symmetric positive definite (Watkins, 2002). First consider the matrix on the left-hand side. Multiplying the matrix by an arbitrary vector from the left and right yields

$$\begin{aligned} \begin{bmatrix} \boldsymbol{v}^T, & \boldsymbol{w}^T \end{bmatrix} \begin{bmatrix} \boldsymbol{M} & 0 \\ 0 & \boldsymbol{M} \end{bmatrix} \begin{bmatrix} \boldsymbol{v} \\ \boldsymbol{w} \end{bmatrix} &= \boldsymbol{v}^T \boldsymbol{M}\boldsymbol{v} + \boldsymbol{w}^T \boldsymbol{M}\boldsymbol{w} \\ &= \mathcal{M}_{ij} v_i v_j + \mathcal{M}_{ij} w_i w_j, \end{aligned} \tag{3.1.48}$$

switching to index notation in the last step for convenience. In the first term, using the definition of M_{ij} given in eq. (3.1.39) yields

$$\begin{aligned} \mathcal{M}_{ij} v_i v_j &= \int_\Omega \phi_i \phi_j v_i v_j \, dx \, dz \\ &= \int_\Omega (\phi_i v_i)^2 \, dx \, dz > 0 \quad \forall \, \boldsymbol{v} \neq 0 \end{aligned} \tag{3.1.49}$$

and the same for the second term, thus the matrix on the left-hand side is symmetric positive definite. Let us now consider the matrix on the right-hand side. Multiplying the matrix by an arbitrary vector from the left and right yields

$$\begin{aligned} \begin{bmatrix} \boldsymbol{v}^T, & \boldsymbol{w}^T \end{bmatrix} \begin{bmatrix} \boldsymbol{K}^1 & \boldsymbol{K}^2 \\ \boldsymbol{K}^3 & \boldsymbol{K}^4 \end{bmatrix} \begin{bmatrix} \boldsymbol{v} \\ \boldsymbol{w} \end{bmatrix} &= \boldsymbol{v}^T \boldsymbol{K}^1 \boldsymbol{v} + \boldsymbol{v}^T \boldsymbol{K}^2 \boldsymbol{w} + \boldsymbol{w}^T \boldsymbol{K}^3 \boldsymbol{v} + \boldsymbol{w}^T \boldsymbol{K}^4 \boldsymbol{w} \\ &= \mathcal{K}^1_{ij} v_i v_j + \mathcal{K}^2_{ij} v_i w_j + \mathcal{K}^2_{ji} w_i v_j + \mathcal{K}^4_{ij} w_i w_j \\ &= \mathcal{K}^1_{ij} v_i v_j + 2\mathcal{K}^2_{ij} v_i w_j + \mathcal{K}^4_{ij} w_i w_j, \end{aligned} \tag{3.1.50}$$

using the fact that $\mathcal{K}^2_{ij} = \mathcal{K}^2_{ji}$ (see eq. (3.1.55)). Using the definitions of these matrices, given in eqs. (3.1.40) to (3.1.43) yields

$$\begin{aligned} \mathcal{K}^1_{ij} v_i v_j + 2\mathcal{K}^2_{ij} v_i w_j + \mathcal{K}^4_{ij} w_i w_j &= \alpha^2 \int_\Omega (\phi_{i,x} v_i)^2 \, dx \, dz + \beta^2 \int_\Omega (\phi_{i,z} v_i)^2 \, dx \, dz \\ &+ 2(\alpha^2 - \beta^2) \int_\Omega \phi_{i,x} v_i \phi_{j,z} w_j \, dx \, dz \\ &+ \beta^2 \int_\Omega (\phi_{j,x} w_j)^2 \, dx \, dz + \alpha^2 \int_\Omega (\phi_{j,z} w_j)^2 \, dx \, dz \\ &= \alpha^2 \int_\Omega (\phi_{i,x} v_i + \phi_{j,z} w_j)^2 \, dx \, dz \\ &+ \beta^2 \int_\Omega (\phi_{i,z} v_i - \phi_{j,x} w_j)^2 \, dx \, dz, \end{aligned} \tag{3.1.51}$$

using the fact that

$$\int_\Omega \phi_{i,x} \phi_{j,z} \, dx \, dz = \int_\Omega \phi_{i,z} \phi_{j,x} \, dx \, dz. \tag{3.1.52}$$

Clearly eq. (3.1.51) is greater than or equal to zero for any $\boldsymbol{v}$ and $\boldsymbol{w}$, therefore the matrix on the right-hand side is symmetric positive semidefinite. □

Proceeding in a similar way as for the acoustic case, let us write the mass and stiffness matrices as fourth-order tensors and as a combination of the corresponding matrices of the 1D problem

$$\mathcal{M}_{ij} = M_{m_1 m_2 n_1 n_2} = \frac{r^2}{\alpha^2} M^{1D}_{m_1 n_1} M^{1D}_{m_2 n_2}, \tag{3.1.53}$$

$$\mathcal{K}^1_{ij} = K^1_{m_1 m_2 n_1 n_2} = r^2 K^{1D}_{m_1 n_1} M^{1D}_{m_2 n_2} + K^{1D}_{m_2 n_2} M^{1D}_{m_1 n_1}, \tag{3.1.54}$$

$$\mathcal{K}^2_{ij} = K^2_{m_1 m_2 n_1 n_2} = (r^2-1) C^{1D}_{m_1 n_1} C^{1D}_{n_2 m_2} = (1-r^2) C^{1D}_{m_1 n_1} C^{1D}_{m_2 n_2}, \tag{3.1.55}$$

$$\mathcal{K}^3_{ij} = K^3_{m_1 m_2 n_1 n_2} = K^2_{m_1 m_2 n_1 n_2}, \quad \text{and} \tag{3.1.56}$$

$$\mathcal{K}^4_{ij} = K^4_{m_1 m_2 n_1 n_2} = K^{1D}_{m_1 n_1} M^{1D}_{m_2 n_2} + r^2 K^{1D}_{m_2 n_2} M^{1D}_{m_1 n_1}, \tag{3.1.57}$$

where $i = (\kappa+1)n_1 + m_1$, $j = (\kappa+1)n_2 + m_2$,

$$M^{1D}_{mn} = \int \varphi_m \varphi_n dx, \tag{3.1.58}$$

$$K^{1D}_{mn} = \int \varphi'_m \varphi'_n dx, \quad \text{and} \tag{3.1.59}$$

$$C^{1D}_{mn} = \int \varphi'_m \varphi_n dx. \tag{3.1.60}$$

Writing U^x_j and U^z_j with two indices using $j = (\kappa+1)n_2 + n_1$ as well, yields

$$U^x_j = U^x_{n_1 n_2} = A_{n_1 n_2} e^{\mathrm{i}(k_x x_{n_1} + k_z z_{n_2} - \omega t)} \quad \text{and} \tag{3.1.61}$$

$$U^z_j = U^z_{n_1 n_2} = B_{n_1 n_2} e^{\mathrm{i}(k_x x_{n_1} + k_z z_{n_2} - \omega t)}. \tag{3.1.62}$$

Since the nodes are κ-periodic in each direction, there are $2\kappa^2$ degrees of freedom and, as in the acoustic case, the constants are also κ-periodic. Thus

$$A_{n_1 n_2} = A_{(\kappa q_1 + l_1)(\kappa q_2 + l_2)} = A_{l_1 l_2} \quad \text{and} \tag{3.1.63}$$

$$B_{n_1 n_2} = B_{(\kappa q_1 + l_1)(\kappa q_2 + l_2)} = B_{l_1 l_2} \tag{3.1.64}$$

for $n_1 = \kappa q_1 + l_1$, $n_2 = \kappa q_2 + l_2$, and $0 \le l_1, l_2 < \kappa$. Substituting in eqs. (3.1.45) and (3.1.46) and eliminating the $e^{-\mathrm{i}\omega t}$ factor yields the following eigenvalue problem of

order $2\kappa^2$:

$$\Lambda\widetilde{M}_{m_1m_2n_1n_2}\widetilde{A}_{n_1n_2} = \widetilde{K}^1_{m_1m_2n_1n_2}\widetilde{A}_{n_1n_2} + \widetilde{K}^2_{m_1m_2n_1n_2}\widetilde{B}_{n_1n_2}, \quad (3.1.65)$$

$$\Lambda\widetilde{M}_{m_1m_2n_1n_2}\widetilde{B}_{n_1n_2} = \widetilde{K}^2_{m_1m_2n_1n_2}\widetilde{A}_{n_1n_2} + \widetilde{K}^4_{m_1m_2n_1n_2}\widetilde{B}_{n_1n_2}, \quad (3.1.66)$$

for $0 \leq m_1, m_2, n_1, n_2 < \kappa$, where

$$\begin{aligned}
\widetilde{M}_{m_1m_2n_1n_2}(k_x,k_z) &= \frac{r^2}{\alpha^2}\widetilde{M}^{1D}_{m_1n_1}(k_x)\widetilde{M}^{1D}_{m_2n_2}(k_z), && (3.1.67)\\
\widetilde{K}^1_{m_1m_2n_1n_2}(k_x,k_z) &= r^2\widetilde{K}^{1D}_{m_1n_1}(k_x)\widetilde{M}^{1D}_{m_2n_2}(k_z) && (3.1.68)\\
&+ \widetilde{K}^{1D}_{m_2n_2}(k_z)\widetilde{M}^{1D}_{m_1n_1}(k_x),\\
\widetilde{K}^2_{m_1m_2n_1n_2}(k_x,k_z) &= (1-r^2)\widetilde{C}^{1D}_{m_1n_1}(k_x)\widetilde{C}^{1D}_{m_2n_2}(k_z), && (3.1.69)\\
\widetilde{K}^4_{m_1m_2n_1n_2}(k_x,k_z) &= \widetilde{K}^{1D}_{m_1n_1}(k_x)\widetilde{M}^{1D}_{m_2n_2}(k_z) && (3.1.70)\\
&+ r^2\widetilde{K}^{1D}_{m_2n_2}(k_z)\widetilde{M}^{1D}_{m_1n_1}(k_x),\\
\widetilde{A}_{n_1n_2}(k_x,k_z) &= A_{n_1n_2}e^{\mathrm{i}(k_x\xi_{n_1}+k_z\xi_{n_2})}, && (3.1.71)\\
\widetilde{B}_{n_1n_2}(k_x,k_z) &= B_{n_1n_2}e^{\mathrm{i}(k_x\xi_{n_1}+k_z\xi_{n_2})}, && (3.1.72)\\
\widetilde{M}^{1D}_{mn}(k_\eta) &= M^{1D}_{m(\kappa l+n)}e^{\mathrm{i}k_\eta hl}, && (3.1.73)\\
\widetilde{K}^{1D}_{mn}(k_\eta) &= K^{1D}_{m(\kappa l+n)}e^{\mathrm{i}k_\eta hl}, \quad \text{and} && (3.1.74)\\
\widetilde{C}^{1D}_{mn}(k_\eta) &= C^{1D}_{m(\kappa l+n)}e^{\mathrm{i}k_\eta hl}\ . && (3.1.75)
\end{aligned}$$

In general, for higher-degree polynomials, there will be more eigenvalues than physical modes. If that is the case, I have found through numerical experimentation that the smallest eigenvalue corresponds to the S-wave dispersion, the next to the P-wave and the others to the non-physical modes; further research is needed to prove this hypothesis.

3.1.2.2 Procedure to Calculate the Grid Dispersion

The procedure to derive the grid dispersion for a given degree, sampling ratio and wavenumber is described below:

1. Compute the 1D mass and stiffness matrices with eqs. (3.1.58) to (3.1.60) using $h = 1$.

2. Compute $\widetilde{M}^{1D}_{mn}(k_x)$, $\widetilde{M}^{1D}_{mn}(k_z)$, $\widetilde{K}^{1D}_{mn}(k_x)$, $\widetilde{K}^{1D}_{mn}(k_z)$, $\widetilde{C}^{1D}_{mn}(k_x)$ and $\widetilde{C}^{1D}_{mn}(k_z)$ using eqs. (3.1.71) to (3.1.75).

3. Build the block matrices of the eigenvalue problem using eqs. (3.1.67) to (3.1.71) with $\alpha = 1$.

4. Solve the eigenvalue problem of eqs. (3.1.65) and (3.1.66) and save the two smallest eigenvalues. Call these Λ'_p and Λ'_s respectively.

5. Calculate the grid dispersion using, for the semi-discrete case,

$$\frac{\alpha_h}{\alpha} = \frac{1}{2\pi\delta}\sqrt{\Lambda'_p} \quad \text{and} \tag{3.1.76}$$

$$\frac{\beta_h}{\beta} = \frac{r}{2\pi\delta}\sqrt{\Lambda'_s}, \tag{3.1.77}$$

   and for the finite-differences in time case,

$$\frac{\alpha_h}{\alpha} = \frac{1}{\pi\delta \mathrm{q}} \sin^{-1}\left(\frac{\mathrm{q}}{2}\sqrt{\Lambda'_p}\right) \quad \text{and} \tag{3.1.78}$$

$$\frac{\beta_h}{\beta} = \frac{r}{\pi\delta \mathrm{q}} \sin^{-1}\left(\frac{\mathrm{q}}{2}\sqrt{\Lambda'_s}\right). \tag{3.1.79}$$

Grid-Dispersion Relations for the First-Degree Elements

Let us consider the first-degree SEM. For this case there are two degrees of freedom and the eigenvalue problem can be solved algebraically. Calculating the mass and stiffness matrices using the trapezoidal quadrature rule and substituting

in eqs. (3.1.67) to (3.1.71) yields

$$\widetilde{\mathbf{M}}(k_x,k_z) = \frac{h^2r^2}{\alpha^2}, \tag{3.1.80}$$

$$\widetilde{\mathbf{K}^1}(k_x,k_z) = 2r^2\left(1-\cos(k_xh)\right)+2\left(1-\cos(k_zh)\right), \tag{3.1.81}$$

$$\widetilde{\mathbf{K}^2}(k_x,k_z) = (r^2-1)\sin(k_xh)\sin(k_zh), \quad \text{and} \tag{3.1.82}$$

$$\widetilde{\mathbf{K}^4}(k_x,k_z) = 2\left(1-\cos(k_xh)\right)+2r^2\left(1-\cos(k_zh)\right). \tag{3.1.83}$$

Substituting these in eqs. (3.1.65) and (3.1.66), and solving the eigenvalue problem, yields $\Lambda_p = \alpha^2(\gamma_1+\gamma_2)/h^2$ and $\Lambda_s = \alpha^2(\gamma_1-\gamma_2)/h^2$, where

$$\gamma_1 = (r^2+1)(2-\cos(k_xh)-\cos(k_zh)) \quad \text{and} \tag{3.1.84}$$

$$\gamma_2 = (r^2-1)\sqrt{(\cos(k_xh)-\cos(k_zh))^2+\sin^2(k_xh)\sin^2(k_zh)}\,, \tag{3.1.85}$$

Using eqs. (3.1.78) and (3.1.79), the following grid-dispersion relations are obtained:

$$\frac{\alpha_h}{\alpha} = \frac{1}{\pi\,\delta\mathrm{q}}\sin^{-1}\left(\frac{\mathrm{q}}{2}\sqrt{\gamma_1+\gamma_2}\right) \quad \text{and} \tag{3.1.86}$$

$$\frac{\beta_h}{\beta} = \frac{r}{\pi\,\delta\mathrm{q}}\sin^{-1}\left(\frac{\mathrm{q}}{2}\sqrt{\gamma_1-\gamma_2}\right). \tag{3.1.87}$$

The stability condition for this scheme is $\mathrm{q}\sqrt{1+1/r^2}\le 1$. As expected, the stability condition and grid-dispersion relations are the same as those for the elastic standard grid FDM (see Appendix 2) because the first-degree elastic SEM is equivalent to the elastic standard grid FDM (Cohen, 2002).

3.1.2.3 Results

In the elastic schemes the grid dispersion is dominated by the S-wave dispersion in an unbounded domain and thus the sampling ratio is determined by the S-wave velocity.[1] Accordingly, the following results will focus on the S-wave dispersion.

[1] In practice the domain is usually bounded and thus the grid dispersion is dominated by the surface waves.

Let us first consider the grid dispersion using the leap-frog scheme for time stepping, eq. (3.1.79). The grid dispersion of the first-degree SEM is shown in Fig. 3.7 for different values of r and incidence angles. Figs. 3.7a and b correspond to eqs. (3.1.86) and (3.1.87). Recall that this particular case corresponds to the standard grid FDM. These figures show that the grid dispersion of the S-wave increases for increasing values of r. In particular, for $r = 10$ (Poisson's ratio equal to 0.495) the S-wave travels at nearly twice the physical velocity using 10 nodes per wavelength. In practice this means that if the physical model has a liquid-solid interface or a high Poisson's ratio, the sampling ratio needs to be very high to obtain accurate results.

This disadvantage is overcome by the staggered-grid finite difference method (see Appendix 2). The grid dispersion of this scheme using 2nd and 4th order approximations has been plotted in Fig. 3.8 for different values of r and incidence angles. Note in these figures that the S-wave dispersion is nearly insensitive to r, therefore this scheme can be efficiently applied to models with liquid-solid interfaces.

The grid dispersion of the first-degree FEM is plotted in Fig. 3.9. Note that, although there is less dispersion than in the first-degree SEM (Figs. 3.7a,b), it is not as accurate as the staggered-grid scheme. Comparing Figs. 3.9a and 3.9b, it can be observed that the grid dispersion and anisotropy increase as r increases.

As noted for the acoustic case, it is also true for the elastic SEM that it is advantageous to use higher-degree methods. It can be observed in Figs. 3.7c and d that, using a sampling ratio of 10 nodes per wavelength and second-degree SEM, the dispersion and anisotropy are negligible even for large values of r. Using higher-degree SEM the dispersion diminishes very fast and the anisotropy disappears, and thus a lower sampling ratio is appropriate (see Fig. 3.10). Comparing Figs. 3.2b and 3.10b it can be concluded that, as intuitively anticipated in Komatitsch et al. (2005),

the dispersion results for the acoustic case can be used to determine the sampling ratio in the elastic case since, for a degree greater than three, the dispersion of the elastic scheme is smaller than the dispersion of the acoustic scheme.

The following results are for the semidiscrete case, eq. (3.1.77). The convergence of FEM and SEM with respect to the sampling ratio and the degree of the elements is shown in Figs. 3.11 and 3.12. As noted for the acoustic case, the grid-dispersion error is $O(h^{2\kappa})$ for either FEM and SEM (see Fig. 3.11). We observe in Fig. 3.12 that SEM is more accurate than FEM, achieving a maximum accuracy for $\kappa = 4$, after which point no further improvements are observed. The row-sum mass-lumping method is also compared and it is shown to be unsuitable for the high-degree methods. This is consistent with the results obtained for the acoustic case.

The numerical anisotropy introduced by the grid dispersion is shown in Fig. 3.13. For comparison purposes, the grid dispersion of the second and fourth order staggered grid FDM (SG-2 and SG-4, respectively) is shown. In Fig. 3.13a, the first degree methods are compared to SG-2 using $\delta = 0.1$. Note the large anisotropic errors introduced by FEM and SEM, whereas the SG-2 dispersion is close to the reference curve. The second degree methods are compared with SG-4 in Fig. 3.13b using $\delta = 0.2$ and a propagation of 100 wavelengths. In this case FEM is the most accurate, and SG-4 the least. The dispersion is minimum for SG-4 at an oblique incidence angle, and for FEM and SEM at an incidence angle parallel to the coordinate axis. In Fig. 3.13c the third-degree methods are compared with SG-4. Note the large and anisotropic grid dispersion introduced by the row-sum mass-lumped FEM. The row-sum mass-lumped FEM is equivalent to SEM for $\kappa = 1, 2$. As noted in Fig. 3.10, the numerical anisotropy introduced by the higher-degree methods is negligible.

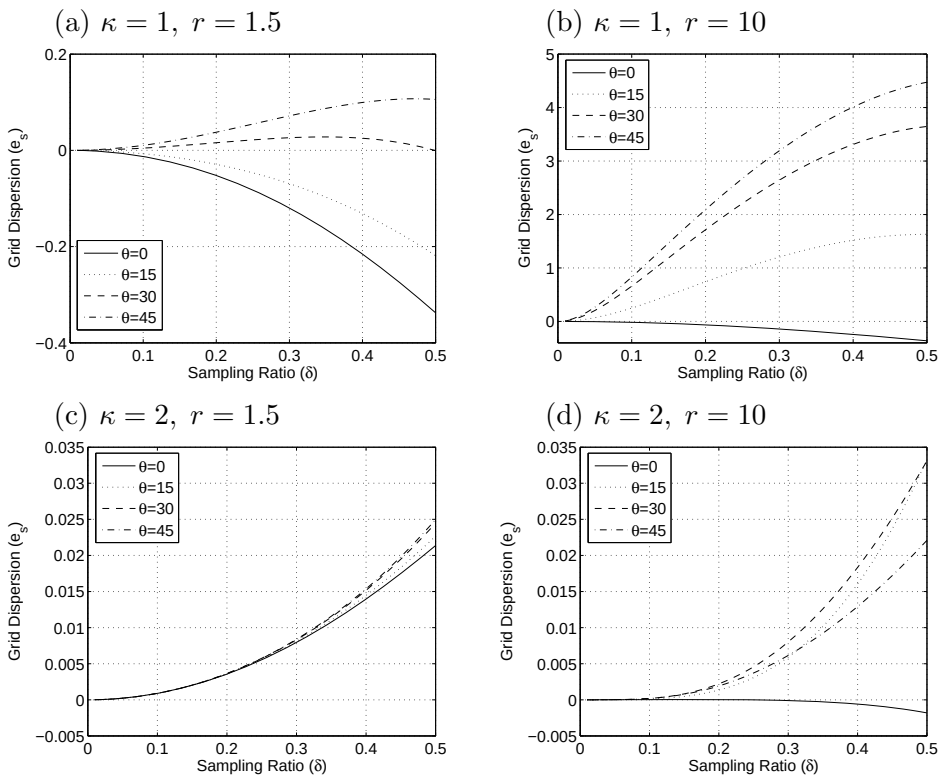

Figure 3.7: Grid dispersion in the first- and second-degree elastic SEM as a function of the sampling ratio using q = 0.7, and (a,c) $r = 1.5$, (b,d) $r = 10$. Recall that the first-degree SEM is equivalent to the standard-grid FDM. Comparing (a) and (b) reveals that the S-wave dispersion increases proportionally to r introducing large anisotropic errors in the 1st degree method.

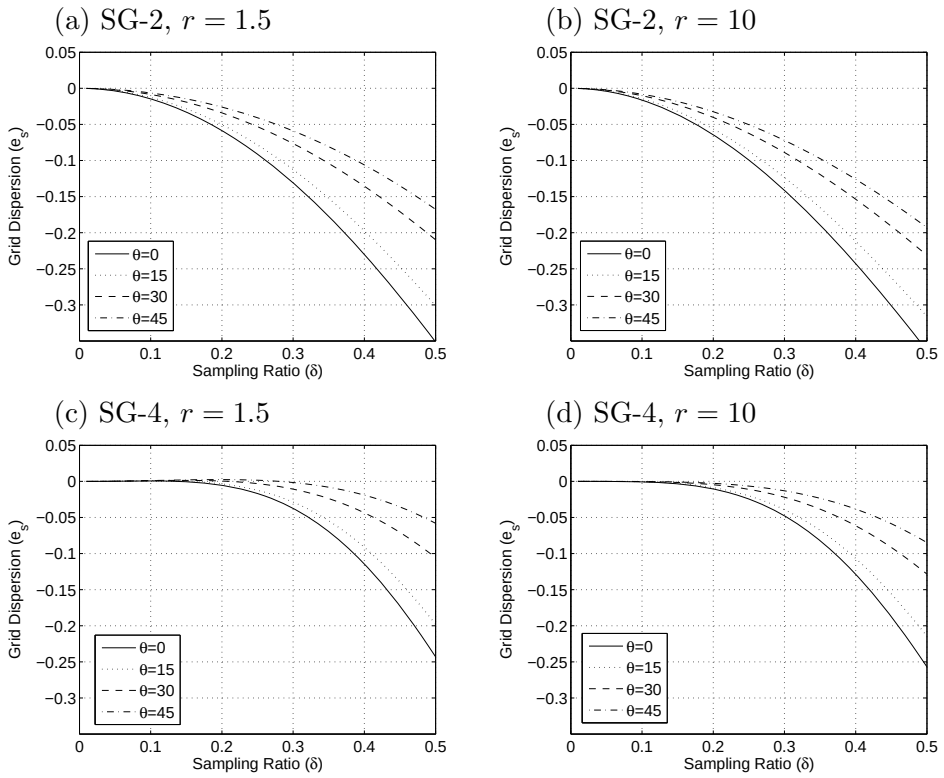

Figure 3.8: Grid dispersion in the second- and fourth-order staggered-grid FDM (SG-2 and SG-4 respectively) using q = 0.7, and (a,c) $r = 1.5$; (b,d) $r = 10$. Note that the S-wave dispersion is not as sensitive to r as in the first-degree SEM.

First-degree Elastic FEM

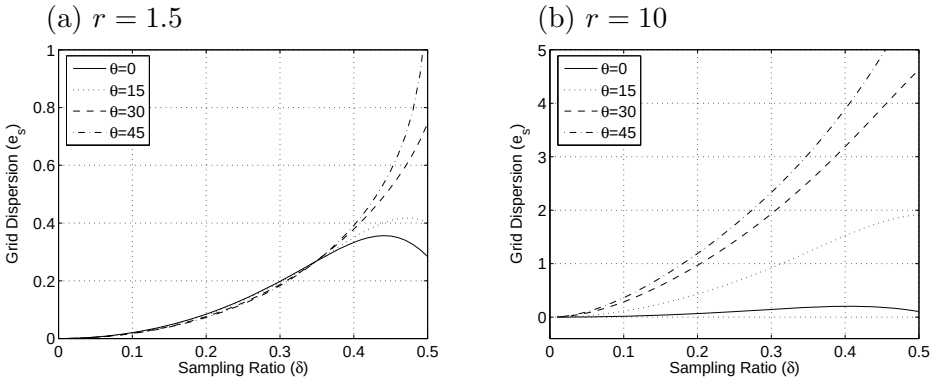

Figure 3.9: Grid dispersion for first-degree elastic FEM, with q = 0.7 and (a) $r = 1.5$, and (b) $r = 10$. Like the first-degree SEM (Figure 3.7), the S-wave dispersion increases proportionally to r and is strongly anisotropic.

Higher-degree Elastic SEM

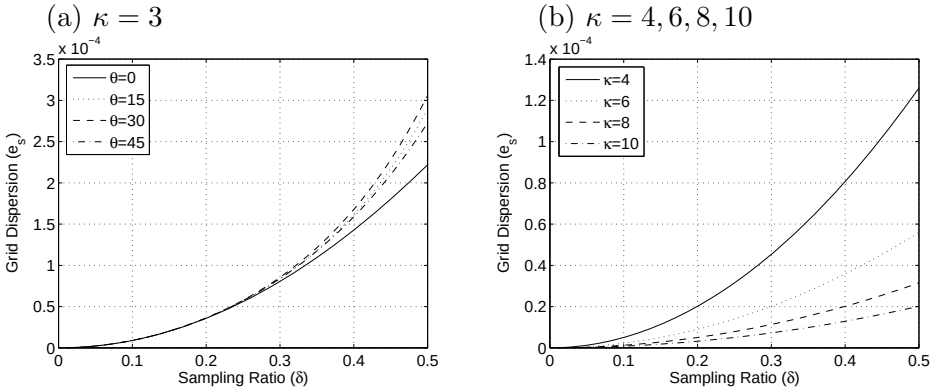

Figure 3.10: Grid dispersion as a function of the degree of the elastic SEM using q = 0.7 and $r = 10$. (a) Third-degree SEM. (b) Fourth- to tenth-degree SEM. The dispersion curves for different incidence angles are plotted in top of each other showing that the dispersion is not angle dependent for fourth-degree elements and above.

Convergence with respect to δ

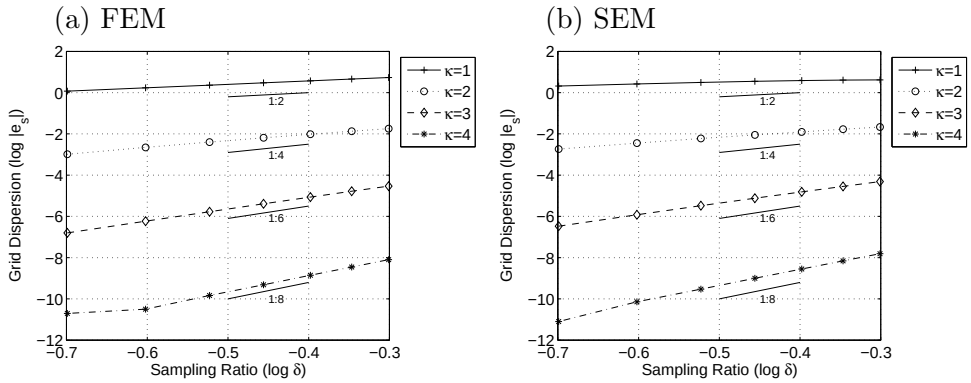

Figure 3.11: Convergence of FEM and SEM with respect to the sampling ratio for $1 \leq \kappa \leq 4$, semidiscrete case. The line segments indicate the slopes of the convergence curves. Note the super-convergence of the grid-dispersion error in both cases.

Convergence with respect to κ

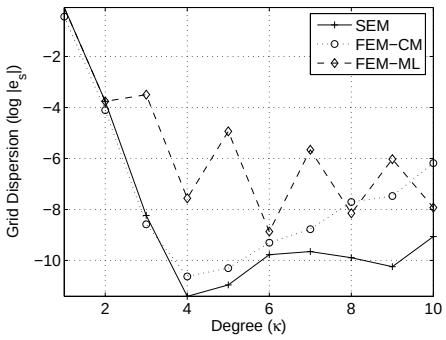

Figure 3.12: Convergence with respect to the degree of the elements of SEM, FEM with a consistent mass matrix (FEM-CM) and FEM with row-sum mass lumping (FEM-ML), semidiscrete case. Note the erratic convergence of FEM-ML.

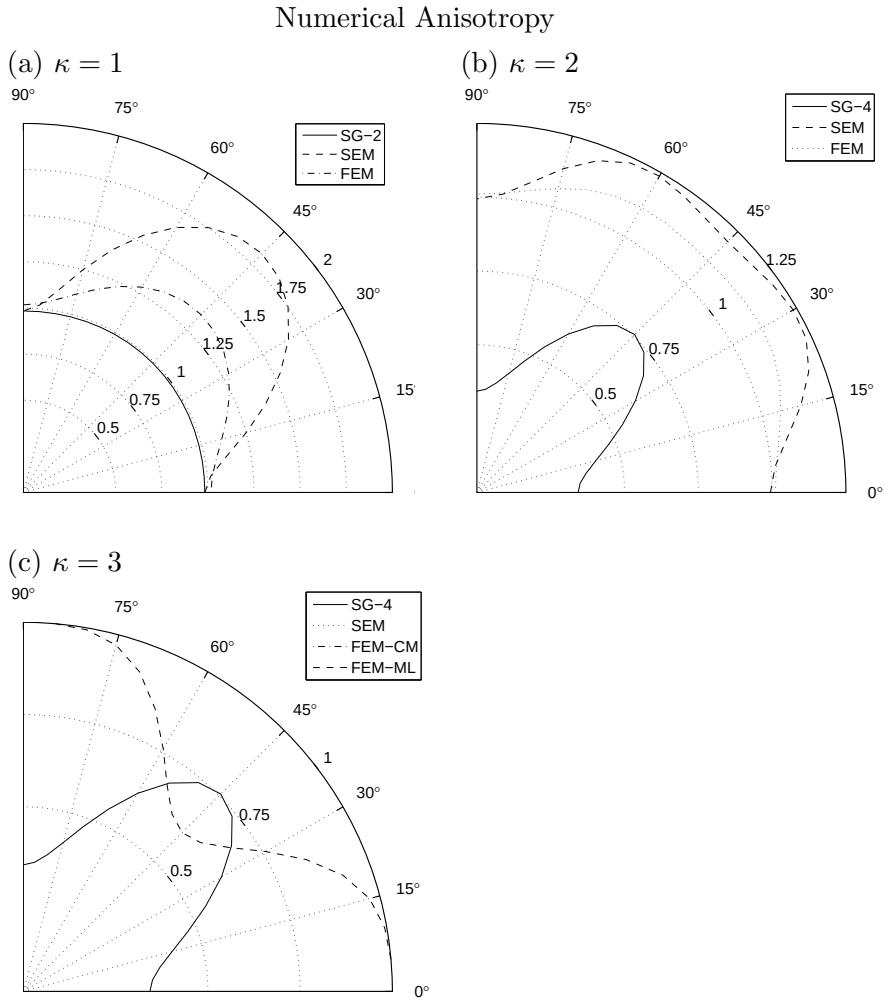

Figure 3.13: Numerical anisotropy of FEM, SEM and Staggered Grid FDM, semidiscrete case. (a) First-degree FEM and SEM compared to SG-2 using $\delta = 0.1,\ r = 10$ and a propagation of one wavelength. Note the large and anisotropic grid dispersion of FEM and SEM. (b) Second-degree FEM and SEM compared to SG-4 using $\delta = 0.2,\ r = 10$ and a propagation of 100 wavelength. The grid dispersion of SG-4 is larger than that of FEM and SEM. (c) Third-degree SEM, FEM with consistent mass and row-sum mass-lumping (FEM-CM and FEM-ML respectively), and SG-4, using $\delta = 0.2,\ r = 10$ and a propagation of 100 wavelength. The curves for FEM-CM and SEM overlap the quarter of a circle with radius one.

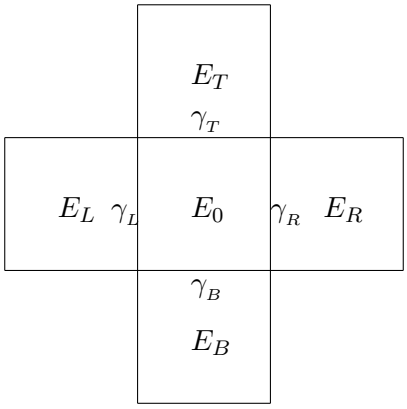

Figure 3.14: The reference element E_0 and it's surrounding elements.

3.2 Interior-Penalty Discontinuous Galerkin Method

This section applies the plane wave analysis to IP-DGM to investigate it's grid dispersion properties. It will be shown that the simplifying assumptions and the plane wave analysis lead to an eigenvalue problem of size equal to the number of degrees of freedom inside one element. A criteria will be given to select the eigenvalues that hold the relevant grid-dispersion information.

3.2.1 Acoustic Case

3.2.1.1 The Eigenvalue Problem

Introducing the assumptions of Table 3.1 into the interior penalty weak formulation of the acoustic wave equation, eq. (2.3.3), yields

$$\sum_{E\in\Omega_h} \left(\alpha^{-2}\partial_{tt}p, v\right)_E + \sum_{E\in\Omega_h} \mathcal{B}_E(p,v) + \sum_{\gamma\in\Gamma_h} \mathcal{J}_\gamma(p,v;S,R) = 0, \tag{3.2.1}$$

where

$$\mathcal{B}_E(p,v) \quad = \quad \int_E \nabla u \cdot \nabla v \; dx \; dz, \quad \text{and} \tag{3.2.2}$$

$$\begin{aligned}\mathcal{J}_\gamma(p,v;S,R) &= -\int_\gamma \{\nabla p\cdot \boldsymbol{n}^\gamma\}[v]\,d\gamma + S\int_\gamma \{\nabla v\cdot \boldsymbol{n}^\gamma\}[p]\,d\gamma \\ &+ R\int_\gamma [p][v]\,d\gamma.\end{aligned} \tag{3.2.3}$$

In order to discretize eq. (3.2.1) using IP-DGM, let us introduce the following approximation to the pressure using the basis functions:

$$p_h(x,z,t) = \sum_{E\in\Omega_h} \phi_i^E(x,z)\zeta_i^E(t), \tag{3.2.4}$$

where ζ_i^E are the coefficients of the DGM approximation to the pressure field in element E. Writing also the test function as a linear combination of the basis functions,

$$v_h(x,z) = \sum_{E\in\Omega_h} \phi_i^E(x,z)a_i^E, \tag{3.2.5}$$

where a_i^E are arbitrary coefficients. Without loss of generality, let us set $a_i^E = 1$ for $E = E_0$ and $i = j$, $a_i^E = 0$ otherwise, where E_0 and j are arbitrary, to obtain

$$\left(\alpha^{-2}\phi_i^{E_0}\partial_{tt}\zeta_i^{E_0}, \phi_j^{E_0}\right)_{E_0} + \mathcal{B}_{E_0}\left(p_h, \phi_j^{E_0}\right) + \sum_{\gamma\in\Gamma_h} \mathcal{J}_\gamma\left(p_h, \phi_j^{E_0}; S, R\right) = 0. \tag{3.2.6}$$

Note in the last term of the left-hand side of eq. (3.2.6) that there are only four elements of Γ_h for which $\mathcal{J}_\gamma$ is non-zero; call these $\gamma_{_T}$, $\gamma_{_B}$, $\gamma_{_L}$ and $\gamma_{_R}$ (see Fig. 3.14). Using the linearity of $\mathcal{B}_E$ and $\mathcal{J}_\gamma$ with respect to the first argument and computing the integrals on the master element $\hat{E}$, eq. (3.2.6) can be written as

$$\frac{h^2}{\alpha^2}M_{ij}\partial_{tt}\zeta_i^{E_0} + K_{ij}\zeta_i^{E_0} + \sum_{f\in\mathcal{S}} L_{ij}^f\zeta_i^{E_f} = 0, \tag{3.2.7}$$

where $\mathcal{S} = \{T, B, L, R\}$,

$$M_{ij} = \left(\phi_i^{\hat{E}}, \phi_j^{\hat{E}}\right)_{\hat{E}}, \tag{3.2.8}$$

$$K_{ij} = \mathcal{B}_{\hat{E}}\left(\phi_i^{\hat{E}}, \phi_j^{\hat{E}}\right), \quad \text{and} \tag{3.2.9}$$

$$L_{ij}^f = \mathcal{J}_{\gamma_f}\left(\phi_i^{\hat{E}_f}, \phi_j^{\hat{E}}; S, R\right). \tag{3.2.10}$$

Assuming that the solution is a plane wave, then

$$\zeta_i^E = A_i e^{\mathrm{i}(\boldsymbol{k}\cdot\boldsymbol{x}_i - \omega t)}, \tag{3.2.11}$$

where $\boldsymbol{k}$ is the wavenumber, $\boldsymbol{x}_i$ contains the ith node coordinates and A_i are arbitrary constants. The plane wave assumption implies that

$$\zeta_i^{E_T} = e^{-\mathrm{i}k_z h}\zeta_i^{E_0}, \qquad \zeta_i^{E_B} = e^{\mathrm{i}k_z h}\zeta_i^{E_0}, \tag{3.2.12}$$

$$\zeta_i^{E_L} = e^{-\mathrm{i}k_x h}\zeta_i^{E_0}, \quad \text{and} \quad \zeta_i^{E_R} = e^{\mathrm{i}k_x h}\zeta_i^{E_0}. \tag{3.2.13}$$

Substituting these in eq. (3.2.7) yields the following generalized eigenvalue problem of order m

$$\Lambda M_{ij}\zeta_i^{E_0} = \widetilde{K}_{ij}\zeta_i^{E_0}, \tag{3.2.14}$$

where $\Lambda = h^2\omega_h^2/\alpha^2$, ω_h is the angular frequency at which the wave travels in the grid and $\widetilde{K}_{ij}$ is the so-called dynamic stiffness matrix, given by

$$\widetilde{K}_{ij} = K_{ij} + e^{-\mathrm{i}k_z h}L_{ij}^T + e^{\mathrm{i}k_z h}L_{ij}^B + e^{-\mathrm{i}k_x h}L_{ij}^L + e^{\mathrm{i}k_x h}L_{ij}^R. \tag{3.2.15}$$

Note that no assumption has been made about the basis functions or grid nodes for the eigenvalue problem in eq. (3.2.14). The basis functions can be any of the ones described in section 2.3.3 or other. The number of eigenvalues will usually exceed the number of physical modes, therefore there is a need to identify which eigenvalues corresponds to the physical wave. This can be easily done by calculating the velocities corresponding to each eigenvalue and comparing to the known P–wave velocity. The grid-dispersion relations for the semidiscrete and finite difference cases are as in FEM, see eqs. (3.1.28) and (3.1.29).

3.2.1.2 Results

Let us consider the grid dispersion of the semidiscrete case using the method described above. The penalty used is of the form $R = \sigma(\kappa+1)(\kappa+2)/(2|\gamma|)$ (after Ainsworth et al., 2006), where $|\gamma|$ is the length of the face γ and $\sigma > 0$ is arbitrary and independent of κ. The numerical experiments indicate that $\sigma \geq 5$ to get accurate results, therefore in the following the value $\sigma = 5$ will be used.

For first degree methods, all the versions of IP-DGM yield the same dispersion, the only difference is observed if exact integration or mass lumping is used. Fig. 3.15a shows the grid dispersion curves using exact integration; this figure is very similar to the grid dispersion of the first degree FEM (Fig. 3.15c), with the difference that the dispersion is slightly smaller. Fig. 3.15b shows the grid dispersion curves using mass lumping; this figure compares exactly with the grid dispersion of the SEM (Fig. 3.15d). Note that Figs. 3.15c and d are the semidiscrete versions of Figs. 3.3(a) and 3.1.

The convergence with respect to the element size is shown in Fig. 3.16. This figure was created using the Gauss basis and $\theta = 45°$. Note that SIPG has the same convergence rate as FEM and SEM (compare Fig. 3.16a with 3.4a and b). On the other hand, NIPG and IIPG have slower convergence rates, different for even and odd degree elements. Note that the error is $O(h^{\kappa+1})$ for odd degree and $O(h^{\kappa})$ for even degree. The convergence rates of NIPG and IIPG are a remarkable result that demands further research (Sun & Wheeler, 2005). The same convergence rates are observed using the GLL basis, but slower convergence rates are observed using the Legendre basis, as shown in Fig. 3.17; this figure shows that the order of convergence of SIPG is $O(h^4)$, and for IIPG and NIPG is $O(h^2)$.

The convergence with respect to element degree is shown in Fig. 3.18. A consistent feature in Figs. 3.18a–c is that the convergence is significantly slower using

Legendre basis. The SIPG method reaches a maximum accuracy of approximately 11 significant digits at $\kappa = 4$, whereas NIPG and IIPG reach this accuracy for $\kappa = 5$. The accuracy of the three methods is compared in Fig. 3.18d. Note the faster convergence of SIPG, and that IIPG is slightly more accurate than NIPG. For $\kappa \geq 5$ the three versions are indistinguishable because machine accuracy is reached.

The numerical anisotropy introduced by the grid dispersion of the three versions of IP-DGM and the three types of basis functions using $\kappa = 2$ is compared in Fig. 3.19. Comparing the three methods, it is clear that SIPG introduced the least anisotropy and NIPG the most anisotropy. Also, comparing the three types of basis functions, using the Legendre basis the waves are delayed, whereas using the GLL or Gauss basis the waves are hastened, except for SIPG in which case the waves are delayed using the GLL basis and hastened using the Legendre basis. A consistent feature in all the methods and all the basis is that the dispersion is minimum at an oblique incidence angle. All the methods using any of the basis functions are isotropic for $\kappa \geq 3$, their anisotropy curves overlap the circle with radius one even at a propagation of 500 wavelengths. The exception to this are the NIPG and IIPG cases using Legendre basis and $\kappa = 3$ and 4 (see Fig. 3.20).

First-degree Acoustic IP-DGM

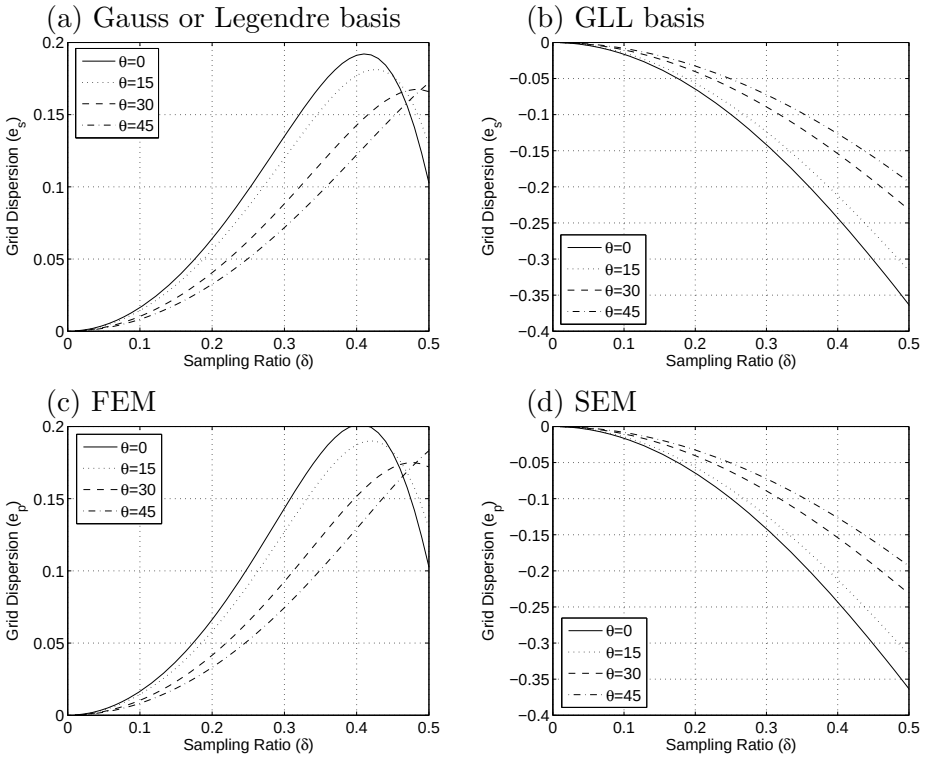

Figure 3.15: Grid dispersion of the first degree acoustic IP-DGM. (a) Using either the Gauss or Legendre basis; (b) using the GLL basis. For comparison purposes, the corresponding figures are shown for (c) FEM and (d) SEM.

Convergence with respect to δ – Nodal Basis

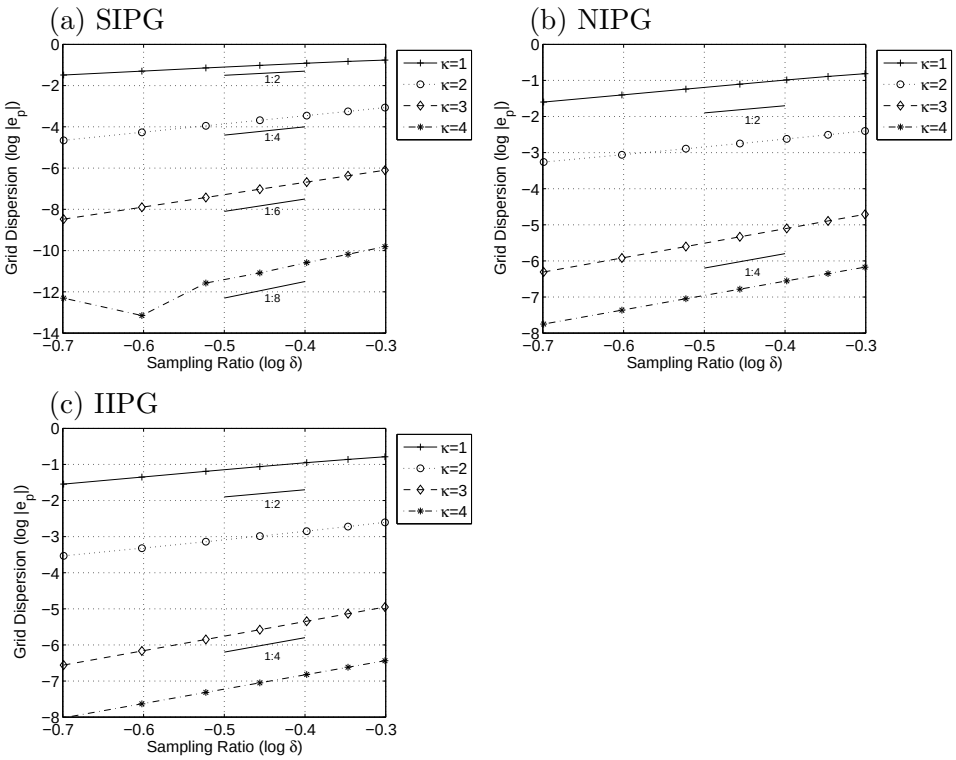

Figure 3.16: Convergence with respect to the element size using GLL or Gauss basis. SIPG using nodal basis exhibits the super-convergence observed in FEM and SEM.

Convergence with respect to δ – Modal Basis

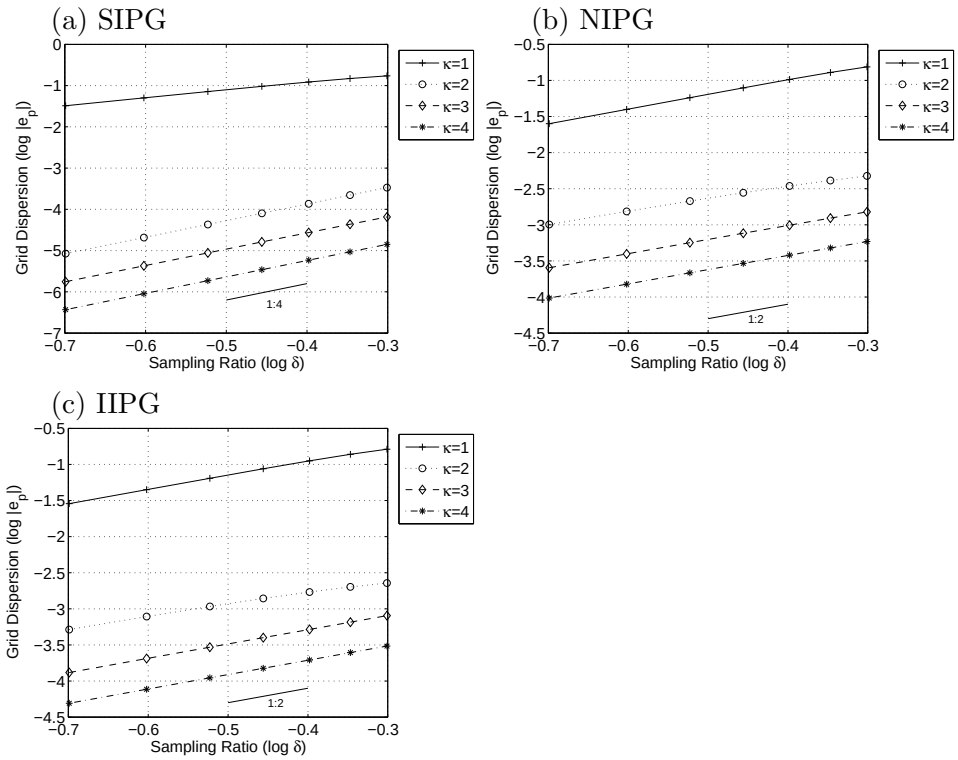

Figure 3.17: Convergence with respect to the element size using Legendre basis. The convergence of all methods is slower than that of using nodal basis.

Convergence with respect to κ

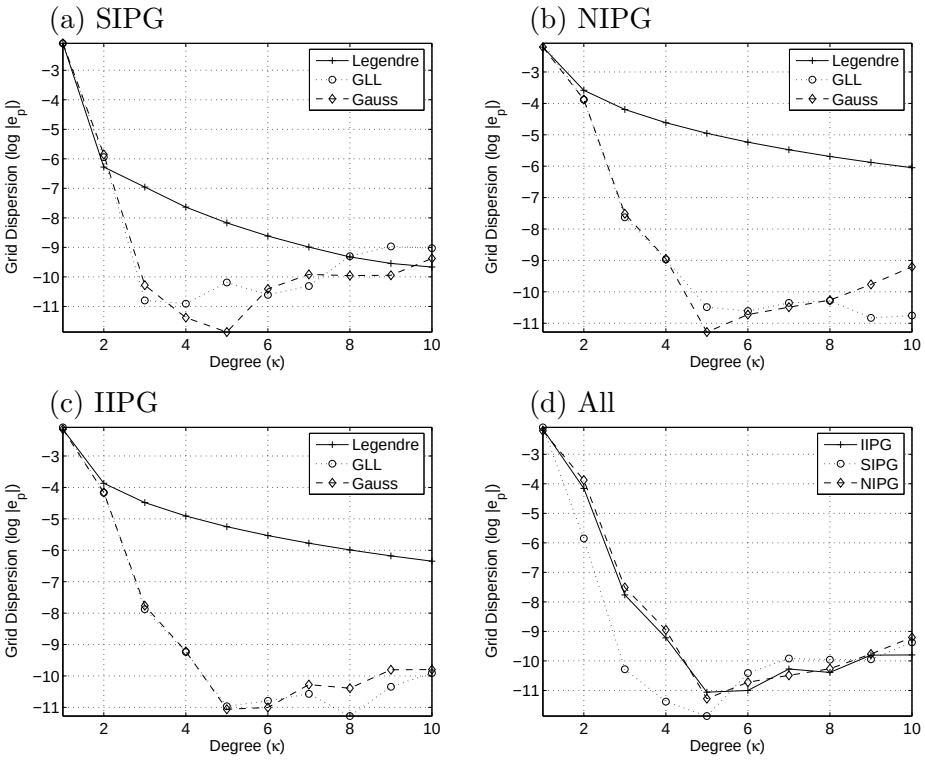

Figure 3.18: Convergence with respect to the elements' order. For comparison purposes, the convergence of the three methods is shown in (c) using the Gauss basis. The Legendre basis exhibit a slower convergence than the nodal basis.

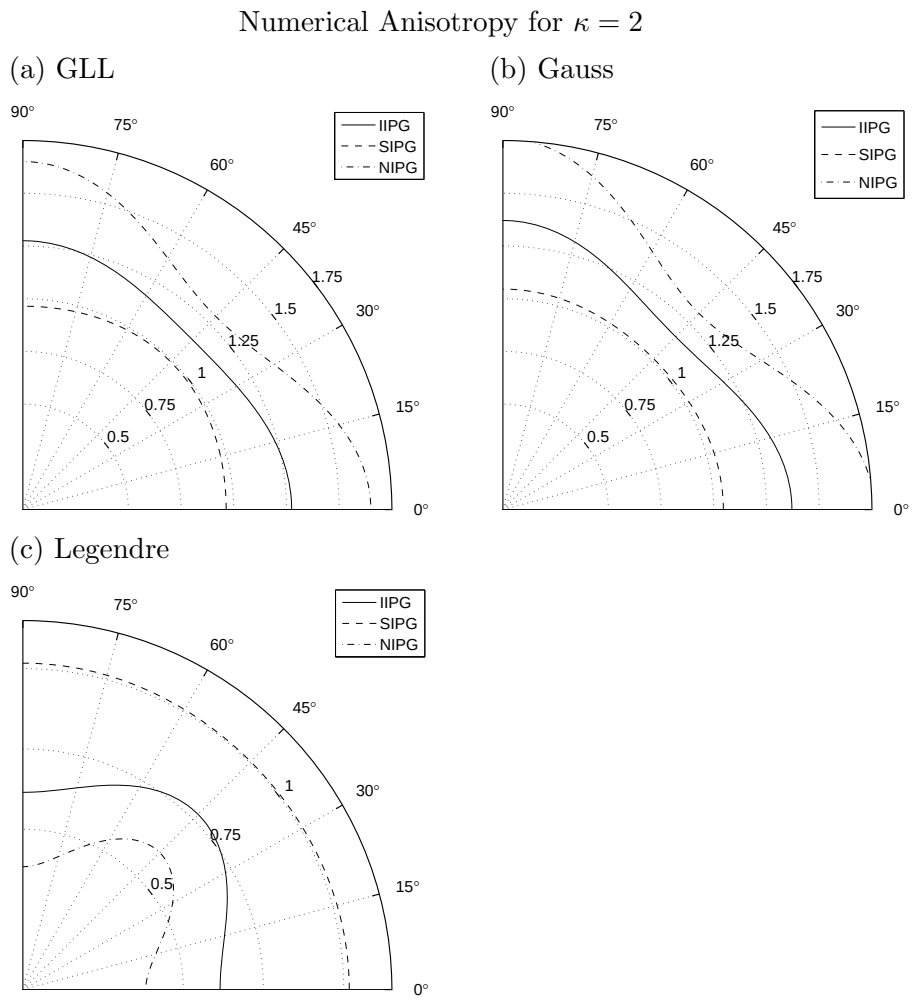

Figure 3.19: Numerical anisotropy introduced by the grid dispersion using the three versions of IP-DGM and three types of basis functions. Each figure considers $\kappa = 2$, a propagation of 500 wavelengths, and $\delta = 0.2$.

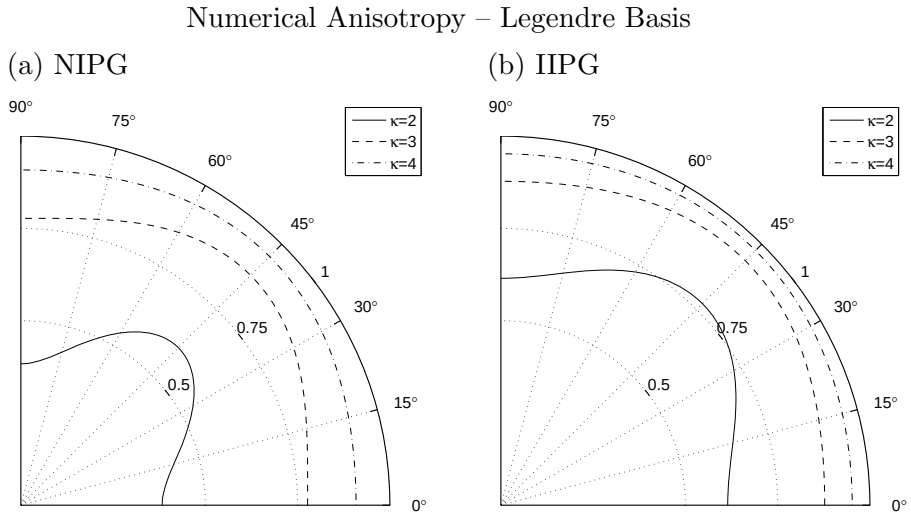

Figure 3.20: Numerical anisotropy introduced by the grid dispersion using the Legendre basis functions. Each figure considers $\kappa = 2, 3, 4$, a propagation of 500 wavelengths, and $\delta = 0.2$.

3.2.2 Elastic Case

3.2.2.1 The Eigenvalue Problem

This section extends the analysis to the elastic case. Introducing the assumptions of Table 3.1 into the interior-penalty weak formulation of the elastic wave equation, eq. (2.2.9), yields

$$\sum_{E\in\Omega_h} \left(\beta^{-2}\partial_{tt}\boldsymbol{u}, \boldsymbol{v}\right)_E + \sum_{E\in\Omega_h} \boldsymbol{\mathcal{B}}_E(\boldsymbol{u}, \boldsymbol{v}) + \sum_{\gamma\in\Gamma_h} \boldsymbol{\mathcal{J}}_\gamma(\boldsymbol{u}, \boldsymbol{v}; S, R) = 0, \quad (3.2.16)$$

where

$$\boldsymbol{\mathcal{B}}_E(\boldsymbol{u}, \boldsymbol{v}) = \int_E \left((r^2 - 2)\nabla\cdot\boldsymbol{u}\nabla\cdot\boldsymbol{v} + (\nabla\boldsymbol{u} + \nabla\boldsymbol{u}^T) : \nabla\boldsymbol{v}\right)\, dx\, dz, \quad (3.2.17)$$

and

$$\begin{aligned}\boldsymbol{\mathcal{J}}_\gamma(\boldsymbol{u},\boldsymbol{v};S,R) &= -\int_\gamma \{(r^2-2)u_{k,k}n_i + (u_{i,j}+u_{j,i})n_j\}[v_i]\,d\gamma \\ &+ S\int_\gamma \{(r^2-2)v_{k,k}n_i + (v_{i,j}+v_{j,i})n_j\}[u_i]\,d\gamma \\ &+ r^2R\int_\gamma [u_i][v_i]\,d\gamma.\end{aligned} \tag{3.2.18}$$

In order to discretize eq. (3.2.16) using IP-DGM, let us introduce the following approximation to the displacement vector using the basis functions:

$$\boldsymbol{u}_h(x,z,t) = \sum_{E\in\Omega_h} \left(\phi_i^E(x,z)\zeta_i^E(t), \phi_i^E(x,z)\eta_i^E(t)\right)^T, \tag{3.2.19}$$

where ξ_i^E and η_i^E are the coefficients of the x and z components of displacement in element E. Also writing the test function as a linear combination of the basis functions,

$$\boldsymbol{v}_h(x,z) = \sum_{E\in\Omega_h} \left(\phi_i^E(x,z)a_i^E, \phi_i^E(x,z)b_i^E\right)^T, \tag{3.2.20}$$

where a_i^E and b_i^E are arbitrary coefficients. Without loss of generality, set $a_i^E = 1$ for $E = E_0$ and $i = j$, $a_i^E = 0$ otherwise, where E_0 and j are arbitrary, and $b_i^E = 0$, to obtain

$$\begin{aligned}&\left(\beta^{-2}\phi_i^{E_0}\partial_{tt}\zeta_i^{E_0}, \phi_j^{E_0}\right)_{E_0} + \boldsymbol{\mathcal{B}}_{E_0}\left(\boldsymbol{u}_h, (\phi_j^{E_0},0)^T\right) \\ &+ \sum_{\gamma\in\Gamma_h} \boldsymbol{\mathcal{J}}_\gamma\left(\boldsymbol{u}_h, (\phi_j^{E_0},0)^T; S, R\right) = 0.\end{aligned} \tag{3.2.21}$$

Setting now $a_i^E = 0$ and $b_i^E = 1$ for $E = E_0$ and $i = j$, $b_i^E = 0$ otherwise, and substituting in eq. (3.2.16) yields

$$\begin{aligned}&\left(\beta^{-2}\phi_i^{E_0}\partial_{tt}\eta_i^{E_0}, \phi_j^{E_0}\right)_{E_0} + \boldsymbol{\mathcal{B}}_{E_0}\left(\boldsymbol{u}_h, (0,\phi_j^{E_0})^T\right) \\ &+ \sum_{\gamma\in\Gamma_h} \boldsymbol{\mathcal{J}}_\gamma\left(\boldsymbol{u}_h, (0,\phi_j^{E_0})^T; S, R\right) = 0.\end{aligned} \tag{3.2.22}$$

Note in the last term of the left-hand side of eqs. (3.2.21) and (3.2.22) that there are only four elements of Γ_h for which $\boldsymbol{\mathcal{J}}_\gamma$ is non-zero, call these γ_T, γ_B, γ_L and γ_R (see Fig. 3.14). Using the linearity of $\boldsymbol{\mathcal{B}}_E$ and $\boldsymbol{\mathcal{J}}_\gamma$ with respect to the first argument and computing the integrals on the master element $\hat{E}$, eqs. (3.2.21) and (3.2.22) can be written as

$$\frac{h^2}{\alpha^2} M_{ij} \partial_{tt} \zeta_i^{E_0} + K_{ij}^1 \zeta_i^{E_0} + K_{ij}^2 \eta_i^{E_0} + \sum_{f \in \mathcal{S}} \left(L_{ij}^{1,f} \zeta_i^{E_f} + L_{ij}^{2,f} \eta_i^{E_f} \right) = 0, \tag{3.2.23}$$

$$\frac{h^2}{\alpha^2} M_{ij} \partial_{tt} \eta_i^{E_0} + K_{ij}^3 \zeta_i^{E_0} + K_{ij}^4 \eta_i^{E_0} + \sum_{f \in \mathcal{S}} \left(L_{ij}^{3,f} \zeta_i^{E_f} + L_{ij}^{4,f} \eta_i^{E_f} \right) = 0, \tag{3.2.24}$$

where $\mathcal{S} = \{T, B, L, R\}$,

$$M_{ij} = \left(r^2 \phi_i^{\hat{E}}, \phi_j^{\hat{E}} \right)_{\hat{E}}, \tag{3.2.25}$$

$$K_{ij}^1 = \boldsymbol{\mathcal{B}}_{\hat{E}} \left((\phi_i^{\hat{E}}, 0)^T, (\phi_j^{\hat{E}}, 0)^T \right) + \sum_{f \in \mathcal{S}} \boldsymbol{\mathcal{J}}_{\gamma_f} \left((\phi_i^{\hat{E}}, 0)^T, (\phi_j^{\hat{E}}, 0)^T \right), \tag{3.2.26}$$

$$K_{ij}^2 = \boldsymbol{\mathcal{B}}_{\hat{E}} \left((0, \phi_i^{\hat{E}})^T, (\phi_j^{\hat{E}}, 0)^T \right) + \sum_{f \in \mathcal{S}} \boldsymbol{\mathcal{J}}_{\gamma_f} \left((0, \phi_i^{\hat{E}})^T, (\phi_j^{\hat{E}}, 0)^T \right), \tag{3.2.27}$$

$$K_{ij}^3 = \boldsymbol{\mathcal{B}}_{\hat{E}} \left((\phi_i^{\hat{E}}, 0)^T, (0, \phi_j^{\hat{E}})^T \right) + \sum_{f \in \mathcal{S}} \boldsymbol{\mathcal{J}}_{\gamma_f} \left((\phi_i^{\hat{E}}, 0)^T, (0, \phi_j^{\hat{E}})^T \right), \tag{3.2.28}$$

$$K_{ij}^4 = \boldsymbol{\mathcal{B}}_{\hat{E}} \left((0, \phi_i^{\hat{E}})^T, (0, \phi_j^{\hat{E}})^T \right) + \sum_{f \in \mathcal{S}} \boldsymbol{\mathcal{J}}_{\gamma_f} \left((0, \phi_i^{\hat{E}})^T, (0, \phi_j^{\hat{E}})^T \right), \tag{3.2.29}$$

$$L_{ij}^{1,f} = \boldsymbol{\mathcal{J}}_{\gamma_f} \left((\phi_i^{\hat{E}_f}, 0)^T, (\phi_j^{\hat{E}}, 0)^T \right), \tag{3.2.30}$$

$$L_{ij}^{2,f} = \boldsymbol{\mathcal{J}}_{\gamma_f} \left((0, \phi_i^{\hat{E}_f})^T, (\phi_j^{\hat{E}}, 0)^T \right), \tag{3.2.31}$$

$$L_{ij}^{3,f} = \boldsymbol{\mathcal{J}}_{\gamma_f} \left((\phi_i^{\hat{E}_f}, 0)^T, (0, \phi_j^{\hat{E}})^T \right), \quad \text{and} \tag{3.2.32}$$

$$L_{ij}^{4,f} = \boldsymbol{\mathcal{J}}_{\gamma_f} \left((0, \phi_i^{\hat{E}_f})^T, (0, \phi_j^{\hat{E}})^T \right). \tag{3.2.33}$$

Assuming that the displacement is a plane wave, then (no summation over i)

$$\zeta_i^E = A_i e^{\mathrm{i}(\boldsymbol{k} \cdot \boldsymbol{x}_i - \omega t)} \quad \text{and} \quad \eta_i^E = B_i e^{\mathrm{i}(\boldsymbol{k} \cdot \boldsymbol{x}_i - \omega t)}, \tag{3.2.34}$$

where $\boldsymbol{k}$ is the wavenumber, $\boldsymbol{x}_i$ contains the ith node coordinates and A_i and B_i are arbitrary constants. The plane wave assumption implies that

$$\zeta_i^{E_T} = e^{-\mathrm{i}k_z h}\zeta_i^{E_0}, \qquad \zeta_i^{E_B} = e^{\mathrm{i}k_z h}\zeta_i^{E_0}, \tag{3.2.35}$$

$$\zeta_i^{E_L} = e^{-\mathrm{i}k_x h}\zeta_i^{E_0}, \qquad \text{and} \qquad \zeta_i^{E_R} = e^{\mathrm{i}k_x h}\zeta_i^{E_0}. \tag{3.2.36}$$

and similar expressions for $\eta_i^{E_f}$, $f \in \mathcal{S}$. Substituting these in eqs. (3.2.23) and (3.2.24) obtains the following generalized eigenvalue problem of order $2m$:

$$\Lambda M_{ij}\zeta_i^{E_0} = \widetilde{K}_{ij}^1\zeta_i^{E_0} + \widetilde{K}_{ij}^2\eta_i^{E_0} \tag{3.2.37}$$

$$\Lambda M_{ij}\eta_i^{E_0} = \widetilde{K}_{ij}^3\zeta_i^{E_0} + \widetilde{K}_{ij}^4\eta_i^{E_0}, \tag{3.2.38}$$

where $\Lambda = h^2\omega_h^2/\alpha^2$, ω_h is the angular frequency at which the wave travels in the grid and $\widetilde{K}_{ij}^\nu, \nu = 1, \ldots, 4$, are the so-called dynamic stiffness matrices, given by

$$\widetilde{K}_{ij}^\nu = K_{ij}^\nu + e^{-\mathrm{i}k_z h}L_{ij}^{\nu,T} + e^{\mathrm{i}k_z h}L_{ij}^{\nu,B} + e^{-\mathrm{i}k_x h}L_{ij}^{\nu,L} + e^{\mathrm{i}k_x h}L_{ij}^{\nu,R}. \tag{3.2.39}$$

The number of eigenvalues will usually exceed the number of physical modes, therefore there is a need to identify which eigenvalues corresponds to the P- and S-waves. We can easily do this by calculating the velocities corresponding to each eigenvalue and comparing to the known P- and S-wave velocities. The grid-dispersion relations are given as in the continuous case, eqs. (3.1.76) and (3.1.77) or eqs. (3.1.78) and (3.1.79).

3.2.2.2 Results

The accuracy of IP-DGM is now discussed from four different perspectives. First, the first-degree methods are considered and compared to the continuous case, then the convergence of the methods with respect to the sampling ratio, and the convergence with respect to the polynomial degree of the basis functions are considered, and finally the anisotropy introduced by the grid dispersion is presented.

The following results focus on the grid dispersion of the S-wave since it is always larger than the dispersion of the P-wave and thus it is of more concern. The penalty used is of the same form used in the acoustic case, $R = \sigma(\kappa+1)(\kappa+2)/(2|\gamma|)$. The numerical experiments indicate that $\sigma \geq 10$ to get accurate results, therefore in the following the value $\sigma = 10$ will be used.

The grid dispersion of the first-degree methods for $r = 1.5$ and $r = 10$ is shown in Fig. 3.21. As noted in the acoustic case, all the formulations yield the same grid dispersion; the only difference is whether the mass matrix is consistent or lumped. The dispersion using a consistent mass matrix (Gauss or Legendre basis) is very similar to that of FEM (compare Figs. 3.21c and e), and the dispersion using mass lumping (GLL basis) is very similar to that of the SEM (compare Figs. 3.21d and f). Also, the grid dispersion using a low value of r is very similar to that of the acoustic case; in fact they become identical for $r = 1$ (compare Figs. 3.21a and b to Figs. 3.15a and b).

The convergence with respect to the sampling ratio of IP-DGM of orders 1 to 4 using the Gauss basis functions, $r = 10$ and an incidence angle of $\theta = 45$ is shown in Fig. 3.22. As a visual aid, line segments are displayed in Fig. 3.22a to indicate the slopes of the convergence curves of different degrees. It is clear that the convergence rate of SIPG is $O(h^{2\kappa})$; recall that this convergence rate was also observed for SEM and for the acoustic SIPG using nodal basis functions. The same convergence rates are achieved for the GLL basis functions, but that is not the case for the NIPG and IIPG methods and for the Legendre basis functions, in which cases slower convergence rates are observed, with no clear relation to κ (see Figs. 3.22b and c, and Fig. 3.23).

The convergence of the methods with respect to the degree of the basis functions is shown in Fig. 3.24. This figure uses the following parameters: $\delta = 0.1$,

$\theta = 45$, and $r = 10$. A consistent feature in this figure is that the convergence rate is slower when the Legendre basis functions are used. I conjecture that this is because the condition number of the mass matrix increases rapidly when the degree of the basis functions is increased (see Appendix 3). On the other hand, the GLL and Gauss basis functions have faster and similar convergence rates. The three formulations are compared using the Gauss basis in Fig. 3.24d. The SIPG method reaches a maximum accuracy of approximately 10 significant digits at $\kappa = 4$, and after this point no further improvement is observed. For the NIPG and IIPG methods the maximum accuracy is achieved at approximately $\kappa = 5$.

The anisotropy introduced by the numerical schemes is displayed in Figs. 3.25 and 3.26. In Fig. 3.25 the three methods and three basis functions are compared using $\kappa = 2$, $r = 10$, $\delta = 0.2$ and a propagation of 100 wavelengths. For this degree, the GLL basis yield the largest dispersion and the Legendre basis the smallest. Also, a consistent feature is that SIPG yields the smallest dispersion and NIPG the largest. The largest dispersion error is observed at an oblique incidence angle, this is opposed to the acoustic case where the largest dispersion was observed parallel to the grid axes. The numerical anisotropy of the higher-degree methods is negligible, except for the Legendre basis. The anisotropy introduced by the grid dispersion using the Legendre basis is shown in Fig. 3.26 using $\kappa = 2, \ldots, 4$. For visualization purposes, a propagation of 200 wavelengths is used. Note that the dispersion for $\kappa = 3, 4$ is quite small even with the high magnification factor. Comparing Figs. 3.13b and 3.25, the grid dispersion of the SEM for this degree is similar to that of using the GLL basis, which is the case that produces the largest dispersion.

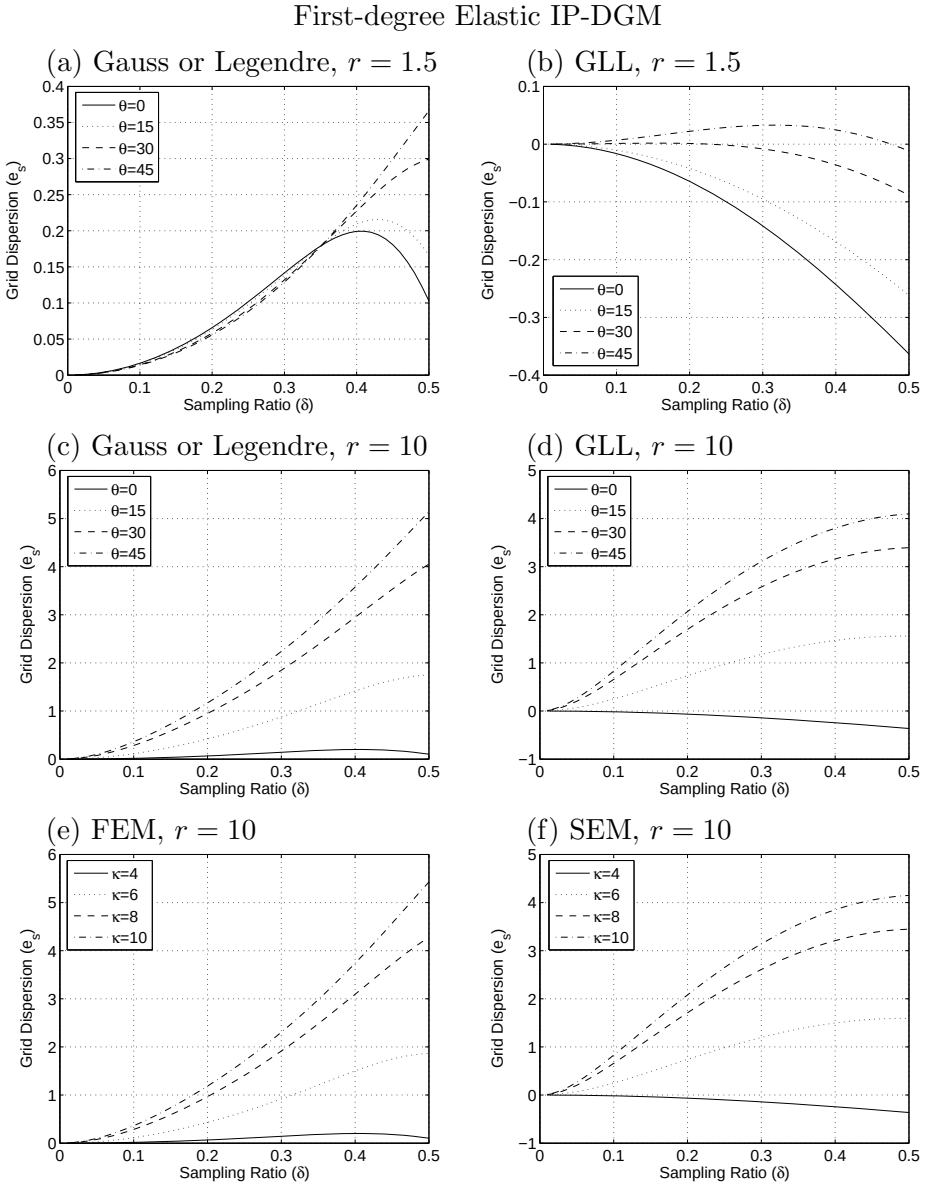

Figure 3.21: Grid dispersion of the first degree elastic IP-DGM. Using either the Gauss or Legendre basis and (a) $r = 1.5$, (c) $r = 10$; Using the GLL basis and (b) $r = 1.5$, (d) $r = 10$. For comparison purposes, the corresponding figures are shown for $r = 10$ and (e) FEM, (f) SEM.

Convergence with respect to δ – Nodal Basis

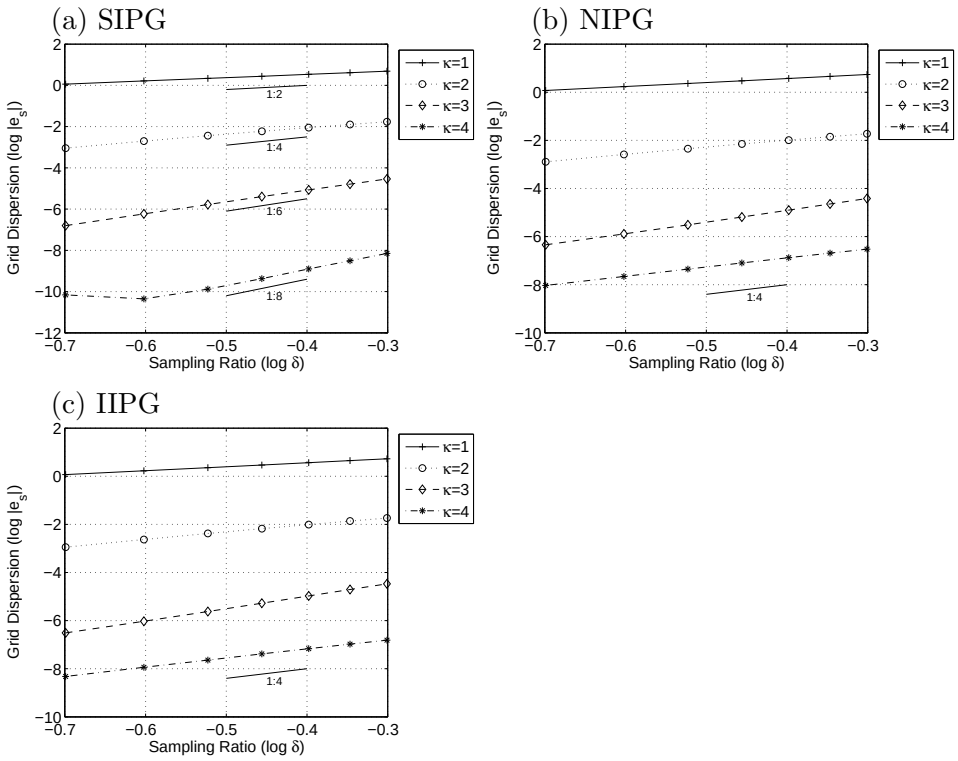

Figure 3.22: Convergence of the elastic IP-DGM with respect to the sampling ratio using the Gauss basis functions, $r = 10$ and $\theta = 45°$. Similar convergence rates are achieved with the GLL basis functions.

Convergence with respect to δ – Modal Basis

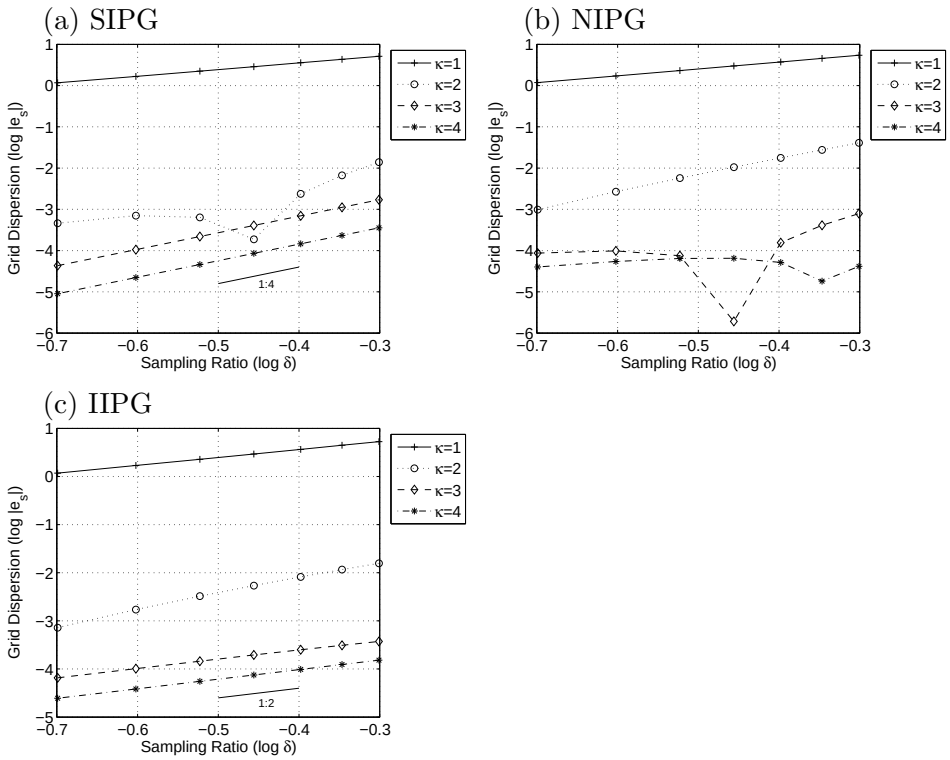

Figure 3.23: Convergence of the elastic IP-DGM with respect to the sampling ratio using the Legendre basis functions, $r = 10$ and $\theta = 45°$.

Convergence with respect to κ

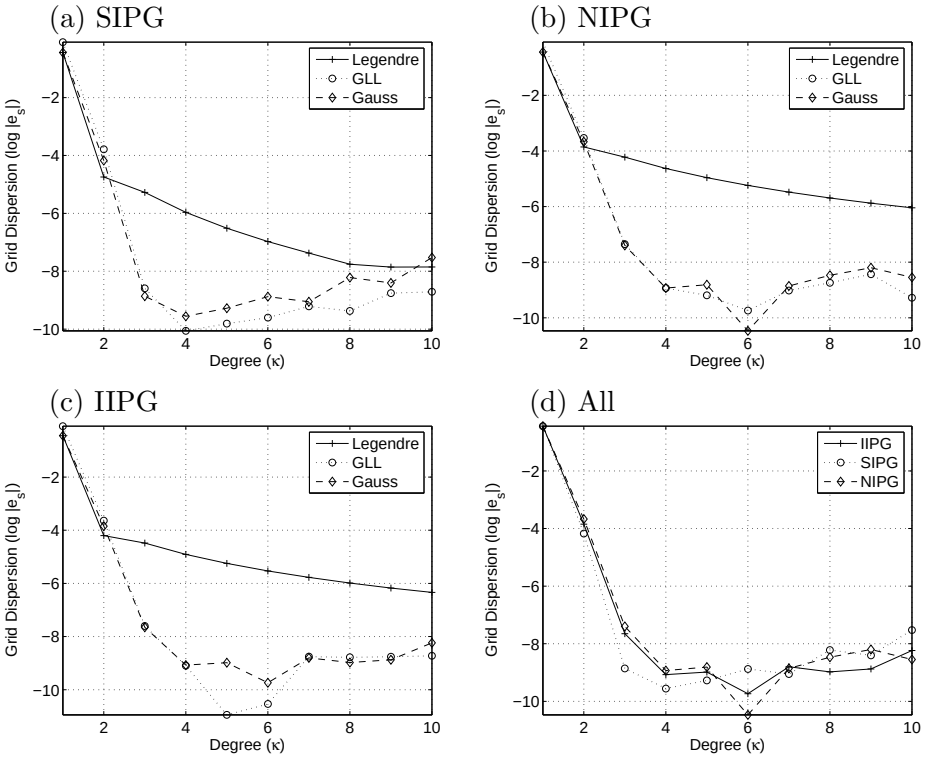

Figure 3.24: Convergence of IP-DGM with respect to the degree of the polynomials using $r = 10$, $\delta = 0.1$, $\theta = 45°$ and (a) SIPG, (b) NIPG, (c) IIPG. For comparison purposes, the three formulations are compared in (c) using the Gauss basis functions. The convergence is slower in the three methods when the Legendre basis functions are used. Using the GLL or Gauss basis functions the convergence is faster, flatting down after an accuracy of approximately 10 significant digits is reached.

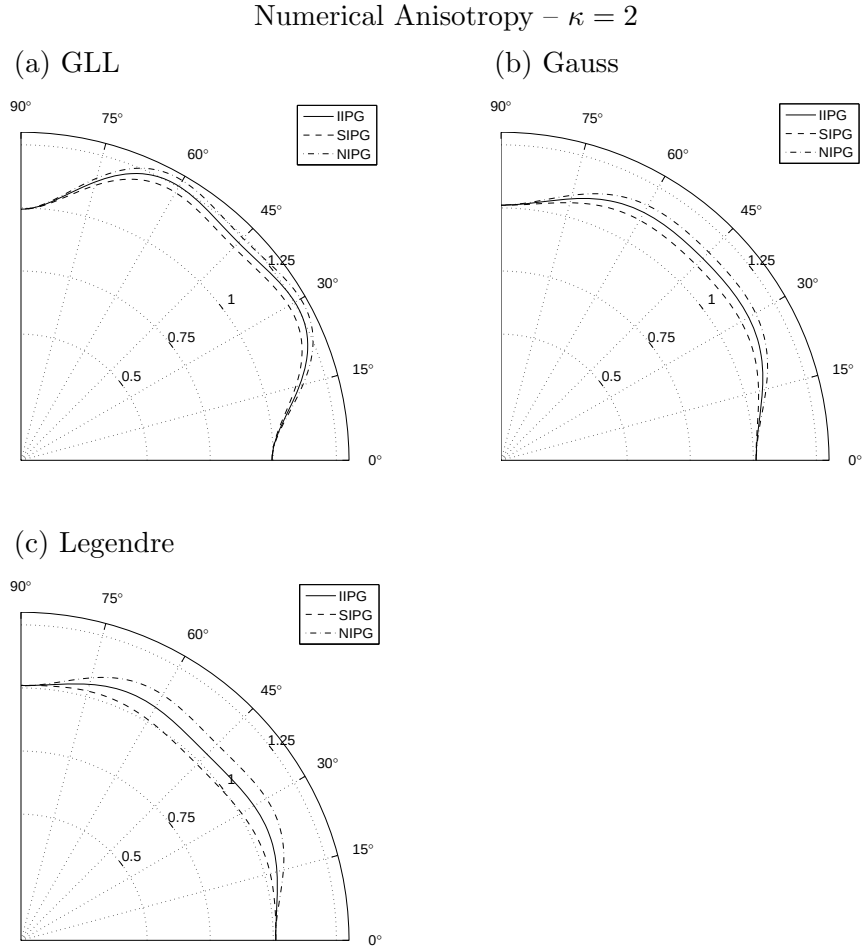

Figure 3.25: Anisotropy curves of IP-DGM using $\kappa = 2$, $r = 10$, $\delta = 0.2$, a propagation of 100 wavelengths and (a) the GLL basis, (b) the Gauss basis, (c) the Legendre basis.

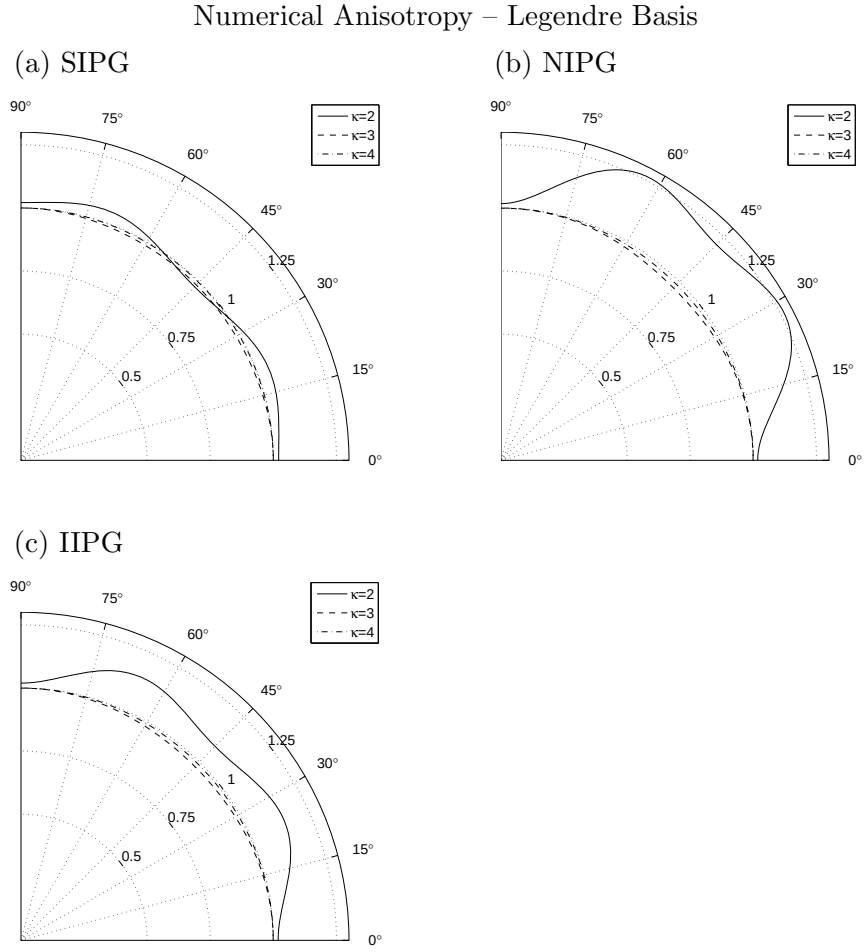

Figure 3.26: Anisotropy curves of IP-DGM using the Legendre basis, $\kappa = 2 \dots 4$, $r = 10$, $\delta = 0.2$, a propagation of 200 wavelengths and (a) SIPG, (b) NIPG, (c) IIPG.

3.3 Stability Conditions

This section gives the stability conditions for the SEM and IP-DGM and for the acoustic and elastic cases using the eigenvalues from the previous sections. It first considers the leap-frog FDM for time stepping and then generalize the results for the LWM. For concreteness, the specific stability bounds for degrees 1 to 10 and an example on how to apply them in practice are given.

Let us consider the eigenvalues of (3.1.27). Using the definition of the eigenvalues for the finite-difference in time case yields

$$\frac{\mathrm{q}^2}{4}\Lambda' = \sin^2 \frac{\omega_h \Delta t}{2} \leq 1, \tag{3.3.1}$$

where $\mathrm{q} = \alpha \Delta t / h$ is the *stability parameter*. Equivalently, the inequality (3.3.1) can be written as $\mathrm{q} \leq 2/\sqrt{\Lambda'}$. Note that Λ' is a function of the wavenumber through eqs. (3.1.10) and (3.1.11), and that the above inequality must be satisfied for all the eigenvalues and all the wavenumbers, thus the *stability condition* for the acoustic case is given by

$$\mathrm{q} \leq \min_{1 \leq j \leq \nu} \min_{0 \leq \theta \leq 2\pi} 2\Lambda'_j(\theta)^{-1/2}, \tag{3.3.2}$$

where $\nu = \kappa^2$ is the number of eigenvalues and θ is the incidence angle. The above stability condition is also applicable to IP-DGM, in which case the number of eigenvalues would be $\nu = m$ and the matrices would be those of eq. (3.2.14). Upper bounds for the stability parameter for degrees from 1 to 10 are given in Table 3.2 using the GLL basis functions. These bounds represent necessary but not sufficient conditions for stability. The numerical experiments indicate that these bounds are as much as 1% higher than the stability limit. The constants are independent of the sampling ratio in the sense that changing it would produce changes in the 4th or 5th significant digit. Note that the constants for SIPG are roughly 4 times smaller than

those for SEM, and that IIPG and NIPG have constants slightly more restrictive than those for SIPG. For completeness, the constants for SIPG using the Gauss and Legendre basis functions are shown in the last two columns. Note that this are slightly smaller than those for the GLL basis, coinciding in most cases and differing in as much as 10% in others.

The stability condition for the elastic case is similar to the one for the acoustic scheme:

$$\mathrm{q} \leq \min_{1\leq j\leq 2\nu} \min_{0\leq\theta\leq 2\pi} 2\Lambda'_j(\theta)^{-1/2} \tag{3.3.3}$$

where $\Lambda'_j(\theta)$ are the eigenvalues of the system (3.1.65) and (3.1.66) or (3.2.37) and (3.2.38), using $h = 1$, $k_x h = \pi s \cos\theta$ and $k_z h = \pi s \sin\theta$ to compute $\widetilde{M}_{m_1 m_2 l_1 l_2}$, $\widetilde{K}^1_{m_1 m_2 l_1 l_2}$, $\widetilde{K}^2_{m_1 m_2 l_1 l_2}$ and $\widetilde{K}^4_{m_1 m_2 l_1 l_2}$. Upper bounds for the stability parameter are given in Table 3.3 using the GLL basis functions and $r = 2$. Note that the constants for SIPG are roughly 6 times smaller than those for the SEM, and that IIPG and NIPG have constants slightly more restrictive than those for the SIPG. The stability conditions for a larger value of r are similar to those shown in Table 3.3. For example, for $r = 10$ they are no more than 20% more restrictive.

The stability conditions given above are related to those for the LWM by very simple relations. Recall from last chapter that the time-stepping scheme of the LWM is based on the expression (ignoring the source term)

$$\mathbf{x}^{n+1} - 2\mathbf{x}^n + \mathbf{x}^{n-1} = 2\sum_{k=1}^{N} \frac{\Delta t^{2k}}{2k!} \left(-A^{-1}B\right)^k \mathbf{x}^n. \tag{3.3.4}$$

Introducing the simplifying assumptions and plane wave analysis, yields

$$\sin^2 \frac{\omega_h \Delta t}{2} = 2\sum_{k=1}^{N} \frac{\mathrm{q}^{2k}}{2k!} \left(\Lambda'\right)^k, \tag{3.3.5}$$

where Λ' are the same as above. The right-hand side is a polynomial in q of degree $2N$, thus the stability parameter needs to satisfy

$$0 \leq \sum_{k=1}^{N} \frac{\mathrm{q}^{2k}}{2k!} \left(\Lambda'\right)^k \leq 2. \tag{3.3.6}$$

As in the finite-difference case, the inequality needs to be satisfied for all the eigenvalues and all incidence angles, therefore the stability condition is

$$\mathrm{q} \leq C_N \min_{1 \leq j \leq \nu} \min_{0 \leq \theta \leq 2\pi} 2\Lambda'_j(\theta)^{-1/2}, \tag{3.3.7}$$

for the acoustic case, and for the elastic case:

$$\mathrm{q} \leq C_N \min_{1 \leq j \leq 2\nu} \min_{0 \leq \theta \leq 2\pi} 2\Lambda'_j(\theta)^{-1/2}, \tag{3.3.8}$$

where C_N is a constant that depends only on the order of the LWM, and its values are given in Table 3.4. Note that the approximation order is $2N$, and that $N = 1$ corresponds to the leap-frog FDM. Since the number of operations required are approximately N times those of the leap-frog scheme, the constants for the higher-order cases are not large enough to upset the extra cost (Cohen, 2002). In particular, the 6th order method allow for a time step only 37% larger than the 2nd order, but requires 3 times as many operations. The 4th order method is the one closest to optimal and the most useful in practice.

The stability constant for a given method, degree and order is given by the product of the corresponding constant in either Table 3.2 or 3.3, and the one from Table 3.4. For example, for the 4th degree acoustic SEM using the leap-frog FDM, the stability condition is given by $\mathrm{q} \leq 0.104$. If the P-wave velocity and size of the elements are given by $\alpha = 1.5\ Km/s$ and $h = 0.04\ Km$, then the time step would be bounded by $\Delta t \leq 0.0027$. If the 4th order LWM is used for the time stepping instead, then $\Delta t \leq 0.0027 \times 1.732 = 0.0048$.

Degree	SEM	SIPG	IIPG	NIPG	Gauss	Legendre
1	0.789	0.188	0.182	0.177	0.110	0.110
2	0.289	0.0758	0.0745	0.0733	0.0753	0.0751
3	0.182	0.0428	0.0413	0.0399	0.0335	0.0307
4	0.104	0.0268	0.0260	0.0252	0.0268	0.0253
5	0.0725	0.0188	0.0180	0.0174	0.0160	0.0145
6	0.0516	0.0136	0.0131	0.0127	0.0136	0.0127
7	0.0392	0.0105	0.0101	0.00971	0.0939	0.00850
8	0.0304	0.00828	0.00795	0.00765	0.00828	0.00765
9	0.0244	0.00674	0.00645	0.00619	0.00615	0.00556
10	0.0200	0.00555	0.00531	0.00511	0.00555	0.00510

Table 3.2: Upper bounds for the stability parameter in the acoustic case. The constants for SIPG, IIPG and NIPG are computed using the GLL basis functions. The last two columns correspond to SIPG using the Gauss and Legendre basis functions.

Degree	SEM	SIPG	IIPG	NIPG
1	0.943	0.151	0.149	0.147
2	0.365	0.0612	0.0608	0.0604
3	0.210	0.0340	0.0335	0.0330
4	0.132	0.0214	0.0211	0.0208
5	0.0886	0.0148	0.0146	0.0144
6	0.0651	0.0108	0.0106	0.0105
7	0.0486	0.00832	0.00818	0.00804
8	0.0383	0.00655	0.00644	0.00634
9	0.0305	0.00531	0.00522	0.00513
10	0.0251	0.00438	0.00430	0.00423

Table 3.3: Upper bounds for the stability parameter in the elastic case using $r = 2$. The constants for SIPG, IIPG and NIPG are computed using the GLL basis functions.

N	Order	C_N
1	2	1
2	4	1.732
3	6	1.375
4	8	2.317
5	10	2.783

Table 3.4: Constants for the stability of LWM.

Chapter 4

Synthetic Seismograms

This chapter describes the software developed to solve the wave propagation problem and shows examples that demonstrate the accuracy of SEM and IP-DGM. The first section describes the seismic wave propagation software. In the second section, some benchmark problems for homogeneous elastic media are considered, and in the third section, a realistic heterogeneous model from exploration geophysics is considered.

4.1 Seismic Wave Propagation Software

The Seismic Wave Propagation software (SWP) is a computer code written in C++ designed to simulate acoustic or elastic wave propagation in 2D. The main characteristic of this software is that it encapsulates many methods for the discretizations in space and time of the acoustic or elastic wave equation and, therefore, it is useful to compare the accuracy and performance of the methods. The available methods for the spatial discretization with their corresponding available methods for time stepping are shown in Table 4.1. IP-DGM includes all possible combinations of the three methods, SIPG, NIPG and IIPG, and the three basis functions, Legendre, Gauss and GLL. IP-DGM also has the option to include an additional penalty term for the velocity (as in Theorem 2.3.2). The polynomial degree of the basis functions used in SEM and IP-DGM can be between 1 and 10.

The source functions available are a vector and a moment tensor applied at

a point, or a combination of them. These are the usual sources in seismic modeling. The vector source represents a directional impulse, and the moment tensor is used to simulate an explosion or a point dislocation. They are implemented as a 2D Gaussian in space for well posedness. The time function of the source can be a Gaussian of specific peak frequency or any of it's derivatives. These are the usual time functions used in seismology, the most common one being the Ricker wavelet which is similar to the second derivative of the Gaussian.

There are three types of output from SWP: the snapshots, the seismograms and the traces. Examples of which are found in the following sections of this chapter. The snapshots represent the wavefield at a given time; these are saved as binary files that represent a 2D image of the wave field at fixed time intervals. The image resolution and the time intervals are configurable through the input file. The snapshots can be visualized as static images or as movies in the time domain using standard geophysical packages, like Seismic Unix (Stockwell, 1999). The seismograms are time functions that record the wave field at a point. The number and location of the points can be easily configured in the input file. Finally, the traces are seismograms recorded at a set of aligned points and are usually displayed as 2D images. The parameters required to configure the traces are the starting points, the increments in the x and z directions and the total number of traces.

The physical domain is a rectangle and there are two ways to specify the media parameters: using a binary or a text file that specifies the values at equispaced points or defining homogeneous horizontal layers. The finite-element mesh can be defined using an input file or, if an input file is not provided, the software generates a rectangular mesh given the number of elements in the x and z directions.

Finally, the following are other technical characteristics of the software:

- The stiffness matrices are implemented as sparse matrices to save computer memory and time;
- There is an experimental multiphysics model for fluid-solid media in which the acoustic wave equation is modeled in the fluid layer and the elastic wave equation in the solid layer;
- The software uses Open MP to take advantage of multiprocessor systems when available;
- The coding style is platform and compiler independent, it has been successfully compiled using Microsoft, GNU, Sun and Intel compilers; and
- The software does not require any external libraries for compiling or running, all the source code was implemented as an integral part of the project.

Method	Version	Time-stepping Methods
SEM	Acoustic	FDM, RK-4, LWM-4
	Elastic	FDM, RK-4, LWM-4
	Acoustic-Elastic	FDM, RK-4
IP-DGM	Acoustic	FDM, RK-4, LWM-4
	Elastic	FDM, RK-4, LWM-4
	Acoustic-Elastic	FDM, RK-4
SG-FDM	Elastic	FDM

Table 4.1: Methods available in SWP. SG-FDM is the 4th order staggered grid FDM, RK-4 is the 4th order Runge-Kutta method and LWM-4 is the 4th order LWM.

4.2 Lamb's Problem

Lamb's problem is a classical benchmark test in numerical seismology. The original problem studied in Lamb (1904) consists of an elastic semispace with a free surface and a point source applied normal to the surface. The name is now used

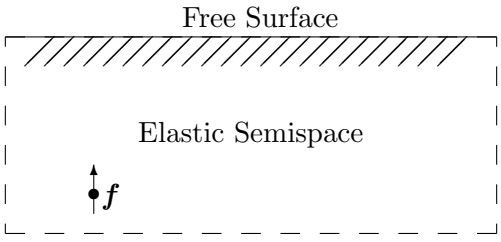

Figure 4.1: Geometry of Lamb's problem. The problem consists of an elastic semispace with a free surface and a vector point source. The dashed lines represent the artificial boundary for the numerical simulations.

for a more general problem in which the source is located anywhere in the elastic semispace and it has an arbitrary direction (see Figure 4.1). The analytic solution for this problem is obtained using Cagniard–De Hoop's method; the details of the solution and references are given in Chapter 6 of Aki & Richards (2002). Source code to compute the analytic solution is available from SPICE. [1]

This section gives the numerical results from two experiments performed using an elastic, isotropic and homogeneous semispace. The first experiment shows how the waves propagate in the subspace without interaction with the boundary. The purpose of this experiment is to give a graphical intuition on the concepts of dispersion and anisotropy discussed in Chapter 3 and to illustrate one of the main conclusions, namely that, for a fixed sampling ratio, increasing the degree diminishes the dispersion. The physical model is a homogeneous rectangle of 1 Km by 1 Km with density, P- and S-wave velocities given by $\rho = 4$ g/cm^3, $\alpha = 3.4$ Km/s and $\beta = 1.7$ Km/s; the source is located at the center and has a peak frequency of 25 Hz. Figures 4.2 and 4.3 show the x and z components of displacement for $\kappa = 1, 2, 4, 8$ using SEM. Figures 4.4 and 4.5 are the ones corresponding to SIPG

[1] Seismic wave Propagation and Imaging in Complex media: a European network (SPICE) http://www.spice-rtn.org/library/software/EX2DDIR

	SEM			IP-DGM		
κ	Δt	N_t	Nodes	Δt	N_t	Nodes
1	0.0025	80	6,561	0.0004	500	25,600
2	0.002	100	6,561	0.00025	800	14,400
4	0.0016	125	6,561	0.00025	800	10,000
8	0.0008	250	6,561	0.00016	1,250	8,100

Table 4.2: Number of nodes and time steps required for SEM and IP-DGM for the experiments in Figures 4.2–4.5.

with GLL basis. All the snapshots are taken at $t = 0.2$ s, the sampling ratio is 5.44 nodes per wavelength and the leap-frog scheme was used for time-stepping. A consistent feature in all the figures is that there is a large amount of dispersion and anisotropy for $\kappa = 1$. Note that, for a constant sampling ratio, increasing the order of the elements improves the isotropy and reduces the dispersion. The simulation parameters used in this experiment are shown in Table 4.2. The size of the time steps, Δt, in the table are approximately 80% of the stability limit given in Chapter 3. Allthough the higher-degree methods require a smaller time step, the lower-degree methods require a higher sampling ratio. This tradeoff makes the higher-degree methods a better choice in terms of accuracy and performance. Note that the number of nodes is constant in SEM but not in IP-DGM because the nodes are duplicated at the elements faces, and that the time steps for IP-DGM are much smaller than those for SEM.

The second experiment shows the interaction of the elastic waves with the free surface. This experiment is suitable to evaluate the accuracy of the different methods for the discretizations in space and in time because the results can be compared with the analytic solution. The density, P- and S-wave velocities of the media are given by $\rho = 2.5$ g/cm^3, $\alpha = 3$ Km/s and $\beta = 1.73$ Km/s respectively, the source is a vertical point force at (0 m, 50 m), and there are two receivers at (1000 m, 0 m) and (707.1 m, 707.1 m). The source function is the first derivative of

a Gaussian with peak frequency of 17.3 Hz. The first part of this experiment is to compare the accuracy of SEM and IP-DGM of different degrees. In order to do that, the simulations use the 4th order LWM for time-stepping and $\Delta t = 0.0005$ s in all the cases. The synthetic seismograms obtained using SEM and SIPG (using the GLL basis) are shown in Figures 4.6 to 4.9. For visualization purposes, the sampling ratio is fixed at 5 nodes per wavelength for the peak frequency; increasing the sampling ratio yields an exact match between the numerical and analytic solutions. Note that even using this low sampling ratio the numerical results are remarkably close to the analytic solution. A consistent feature in all the figures is that the amplitude of the dispersion is inversely proportional to the degree of the methods, as expected from the analysis in Chapter 3. The 8th degree methods, because of their low dispersion, capture all the features of the waveform. In particular, for the 2nd receiver, the 8th degree solutions practically overlap the exact solution. For comparison purposes, Figure 4.10 shows the 6th and 8th degree synthetic seismograms using SEM and SIPG. The differences between the results from the two methods are negligible.

The second part of this experiment is to compare the three formulations and three basis functions of IP-DGM. Figures 4.11 and 4.12 show the seismograms using the 4th degree SIPG and the three types of basis functions. The seismograms from receiver 1 show that the dispersion introduced by the Legendre and Gauss basis arrives before the main S-wave, whereas the dispersion introduced by the GLL basis arrives after the main S-wave. In receiver 1, the amplitude of the dispersion introduced by the GLL basis is smaller than that of the other basis, but in receiver 2 the dispersion is not significatively different in any of the three cases. Also a comparison of the three formulations of the IP-DGM, using the GLL basis, reveals that they are not significatively different, as shown in Figure 4.13.

Finally, the accuracy of three time-stepping methods is compared, namely,

2nd order FDM, 4th order LWM and 4th order RK. Figure 4.14 shows the seismograms from receiver 1 using 4th degree SEM and different time-stepping methods. The size of the time steps used are $\Delta t = 0.003$ s for FDM, $\Delta t = 0.005$ s for LWM and $\Delta t = 0.0045$ s for RK. The LWM yields a smaller dispersion and allows for a larger time step, whereas RK yields a larger dispersion an phase shift and requires a time step slightly smaller than that of LWM.

4.3 The SEG/EAGE Salt-Dome Model

This section considers a more realistic example using the SEG/EAGE salt-dome model. Figure 4.15 shows the density, P- and S-wave velocities of this model. The upper layer is a liquid medium representing the sea and at the center there is a salt dome with a large velocity contrast. The physical domain is 12 Km by 4 Km and it has been discretized using a mesh of 600 by 200 elements. The receivers are located at the sea floor depicting an OBC[2] geometry in order to be able to record the x and z components of displacement.

Figures 4.16 and 4.17 shows the x and z components of displacement for the synthetic traces obtained using the 4th degree SEM and the 4th order LWM. Different phases in the seismograms are clearly visible in the figures.

[2]Ocean Bottom Cable: a common data acquisition configuration in exploration geophysics.

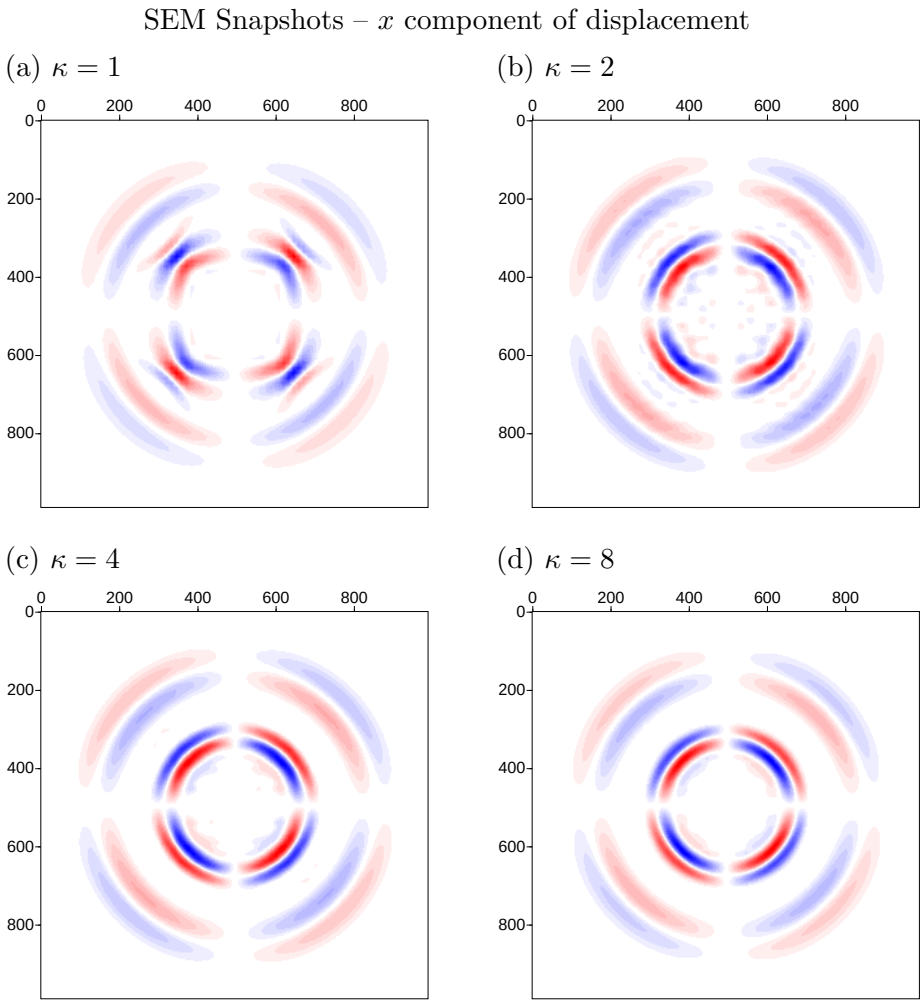

Figure 4.2: Snapshots of the x component of displacement at $t = 0.2$ using SEM and $\kappa = 1, 2, 4, 8$.

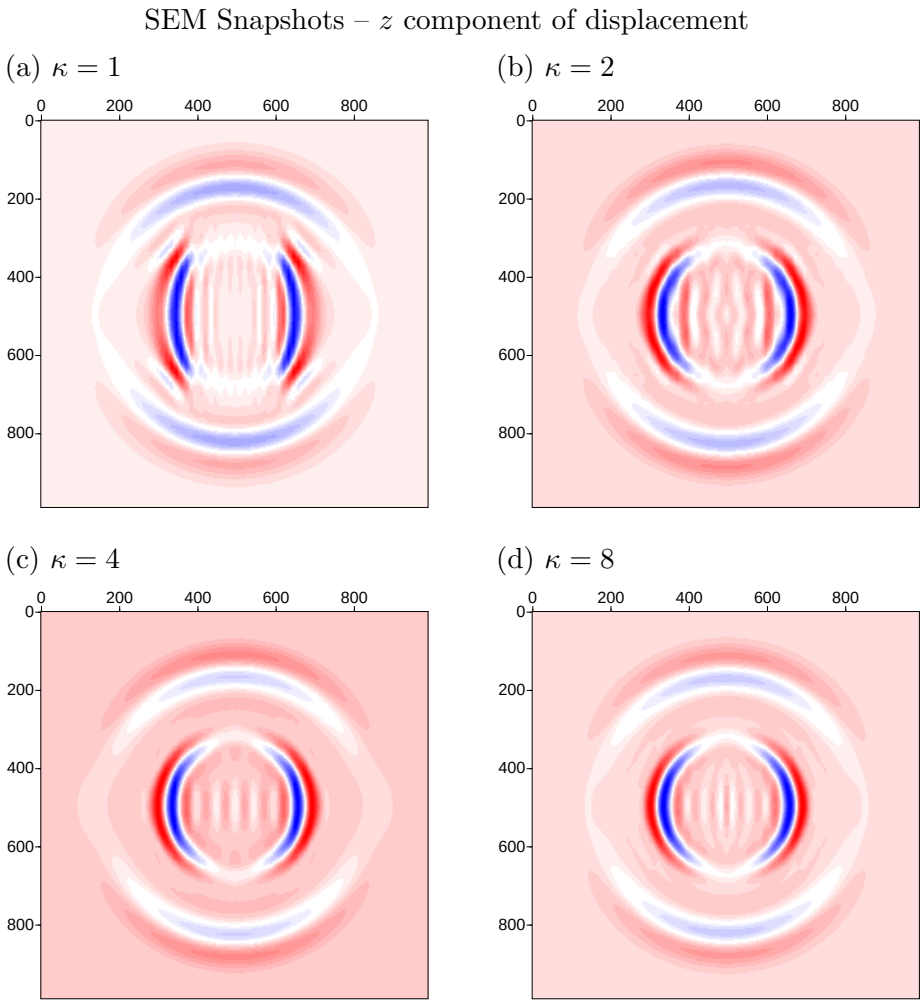

Figure 4.3: Snapshots of the z component of displacement at $t = 0.2$ using SEM and $\kappa = 1, 2, 4, 8$.

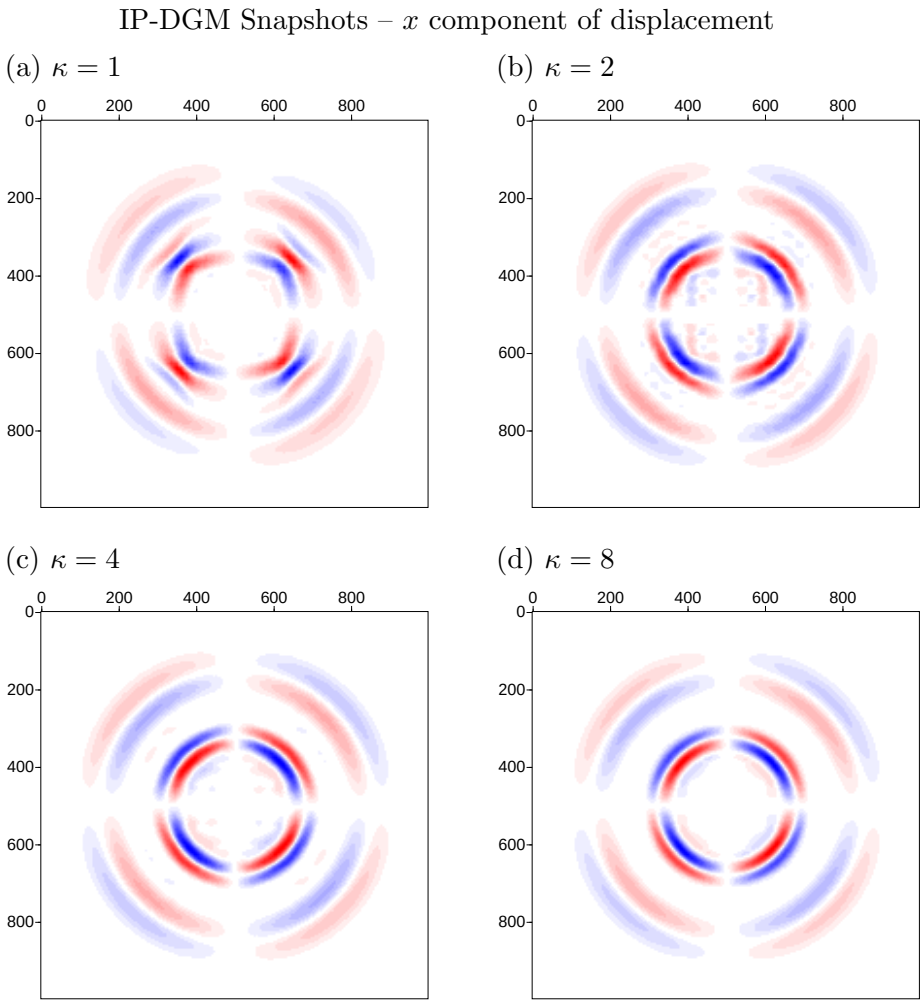

Figure 4.4: Snapshots of the x component of displacement at $t = 0.2$ using IP-DGM and $\kappa = 1, 2, 4, 8$.

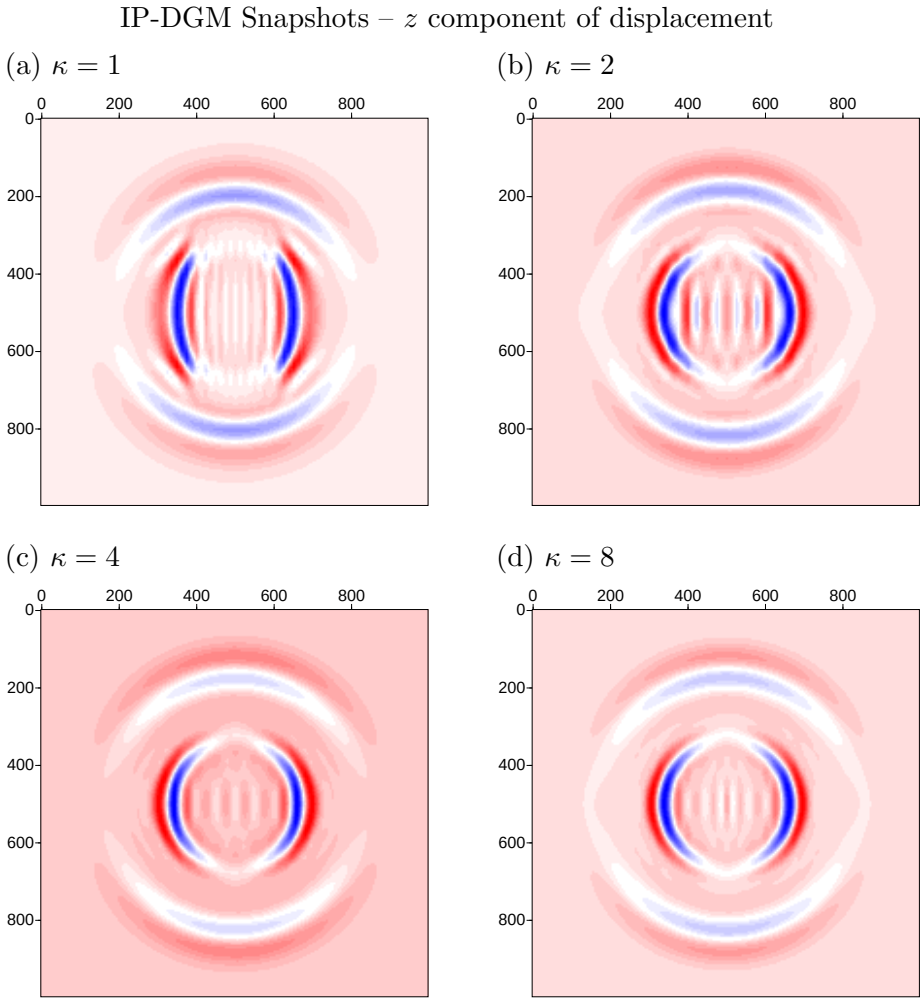

Figure 4.5: Snapshots of the z component of displacement at $t = 0.2$ using IP-DGM and $\kappa = 1, 2, 4, 8$.

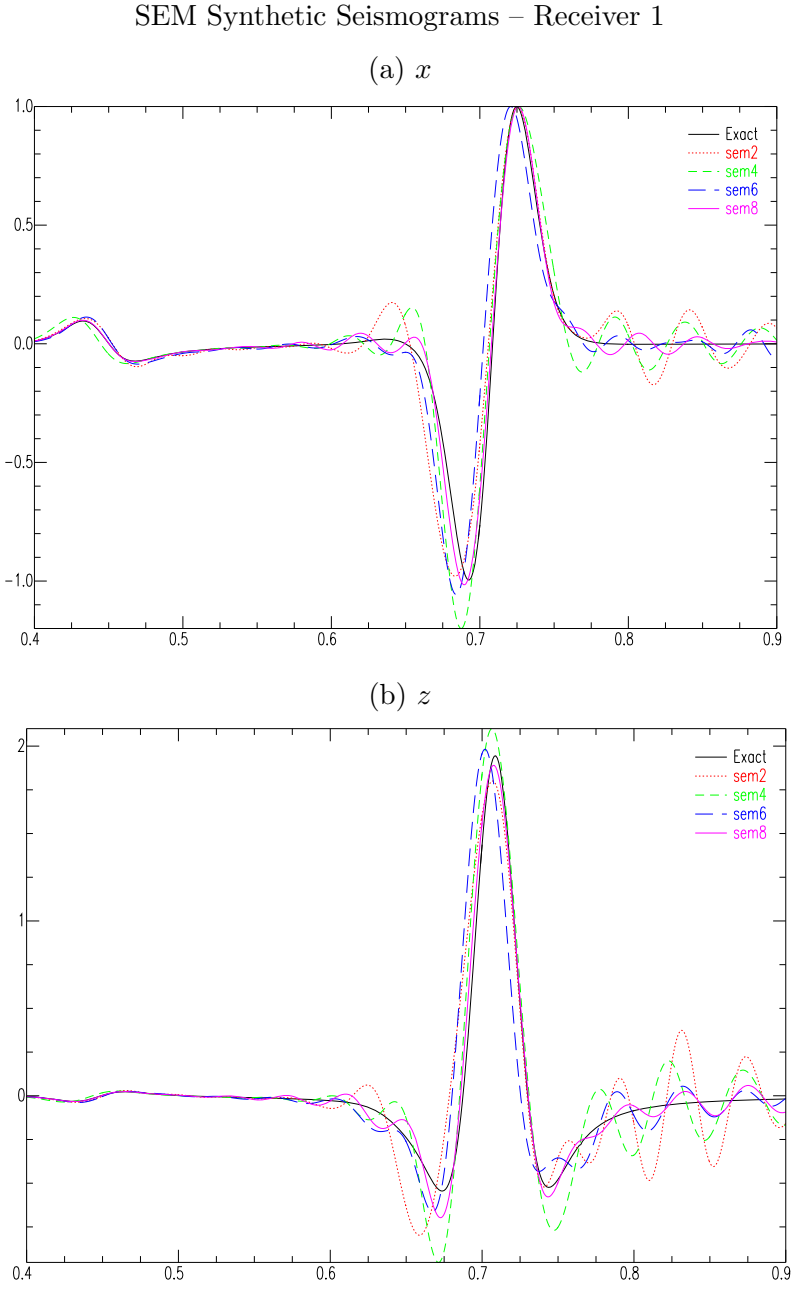

Figure 4.6: Comparison of synthetic seismograms from receiver 1 for Lamb's problem obtained using SEM of different degrees.

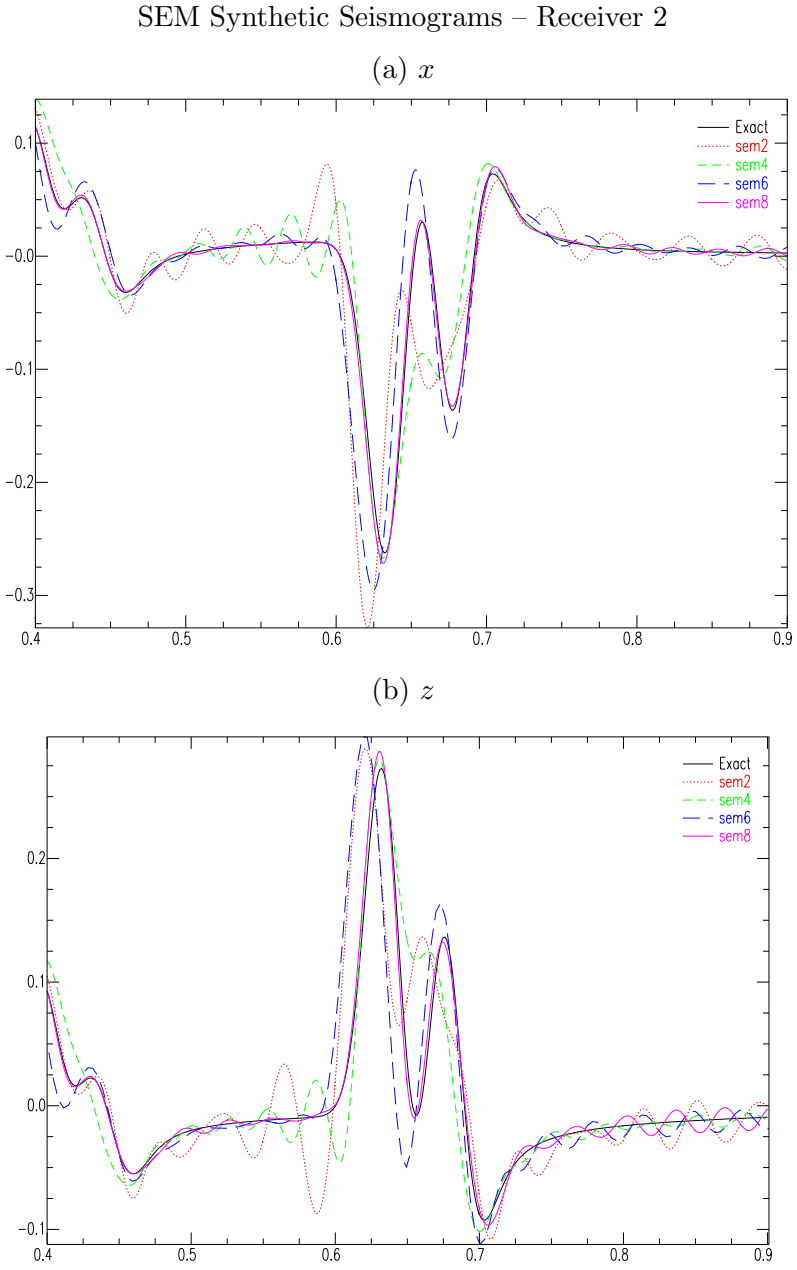

Figure 4.7: Comparison of synthetic seismograms from receiver 2 for Lamb's problem obtained using SEM of different degrees.

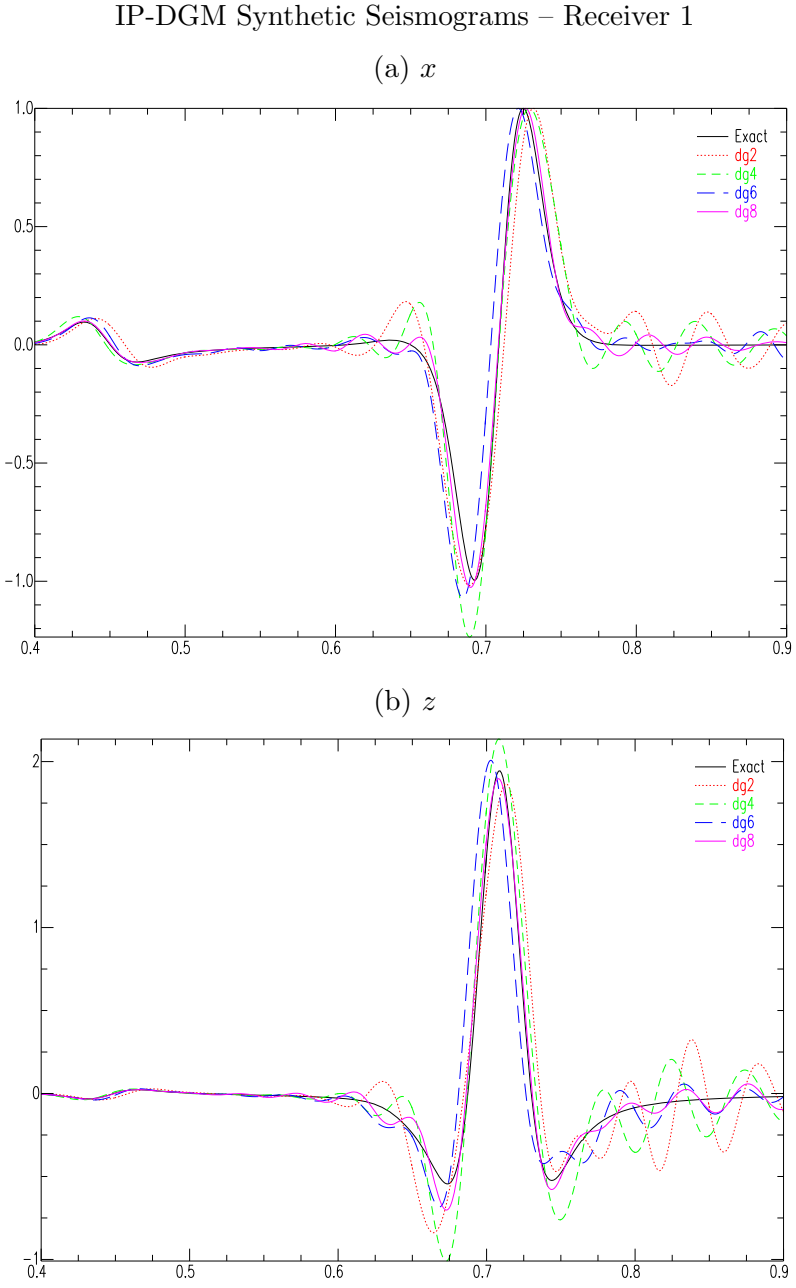

Figure 4.8: Comparison of synthetic seismograms from receiver 1 for Lamb's problem obtained using SIPG and the GLL basis of different degrees.

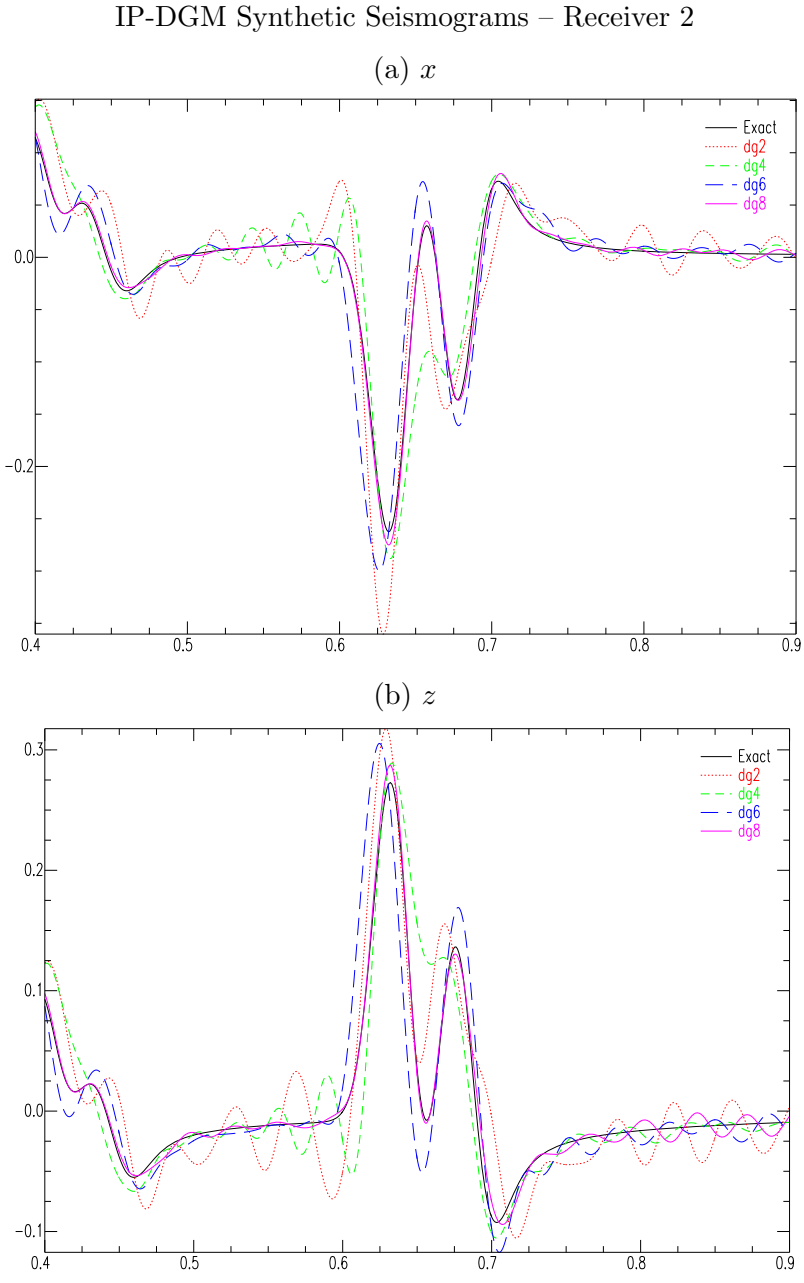

Figure 4.9: Comparison of synthetic seismograms from receiver 2 for Lamb's problem obtained using SIPG and the GLL basis of different degrees.

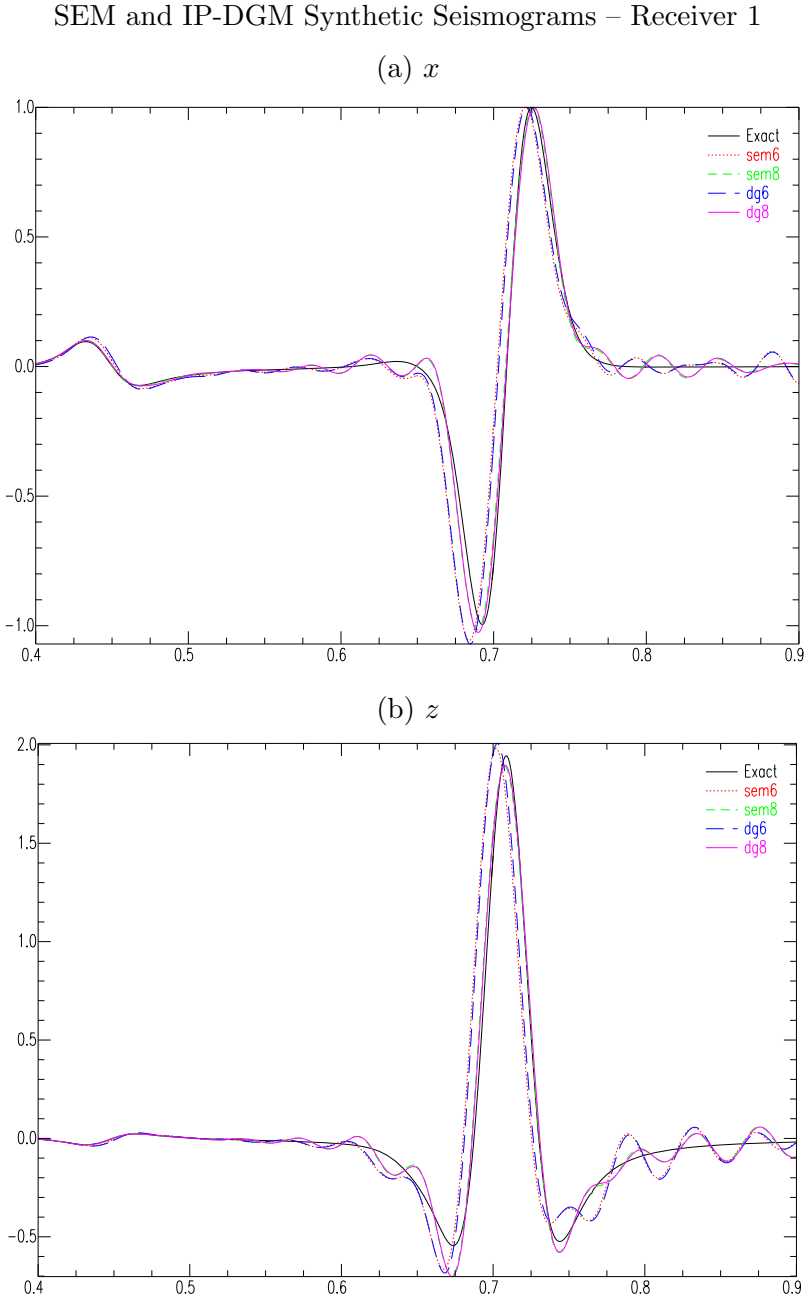

Figure 4.10: Comparison of synthetic seismograms from receiver 1 for Lamb's problem obtained using SEM and IP-DGM.

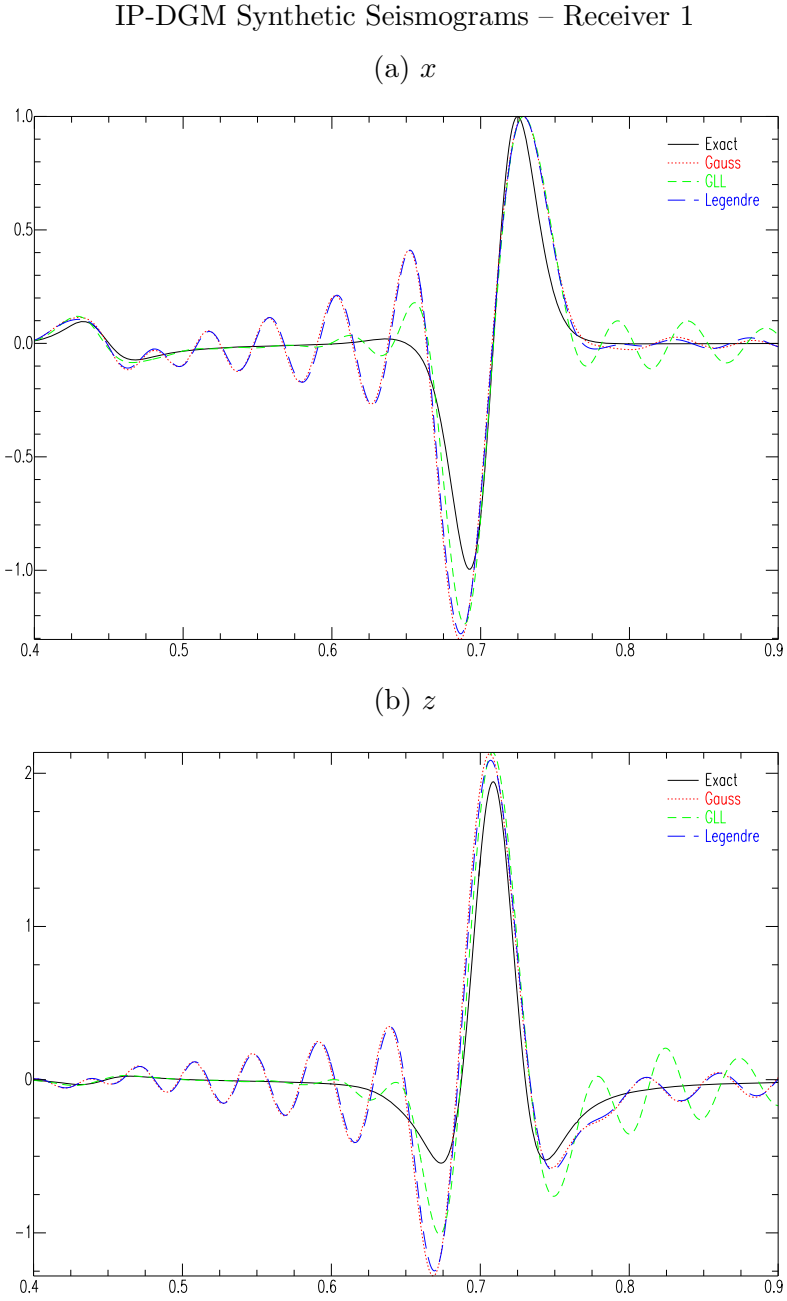

Figure 4.11: Comparison of synthetic seismograms from receiver 1 for Lamb's problem obtained using the 4th degree SIPG and the three types of basis functions.

IP-DGM Synthetic Seismograms – Receiver 2

(a) x

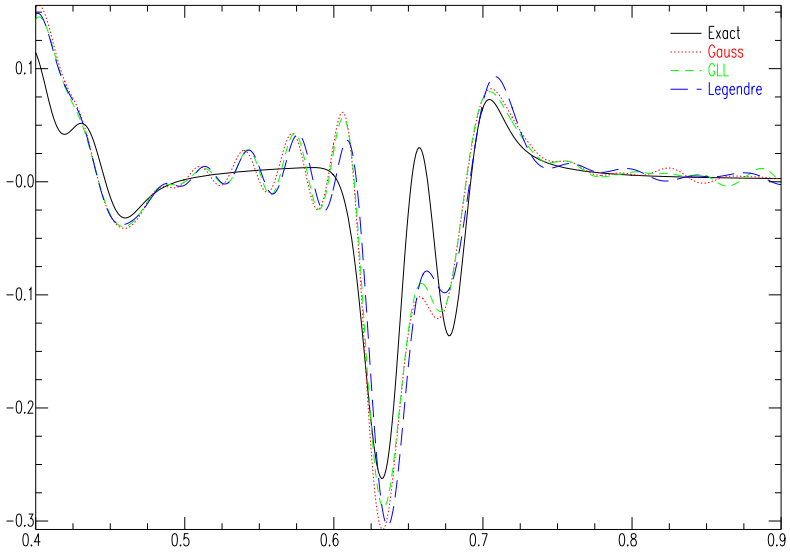

(b) z

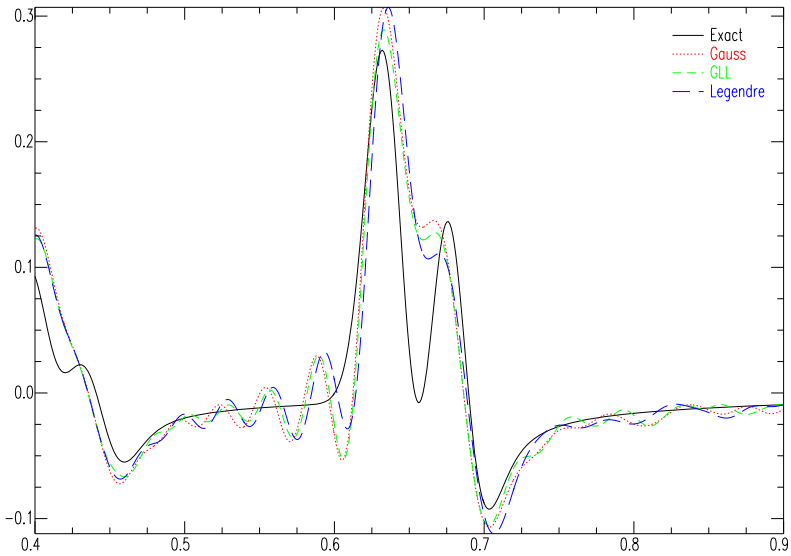

Figure 4.12: Comparison of synthetic seismograms from receiver 2 for Lamb's problem obtained using the 4th degree SIPG and the three types of basis functions.

IP-DGM Synthetic Seismograms – Comparison of the Formulations

(a) x

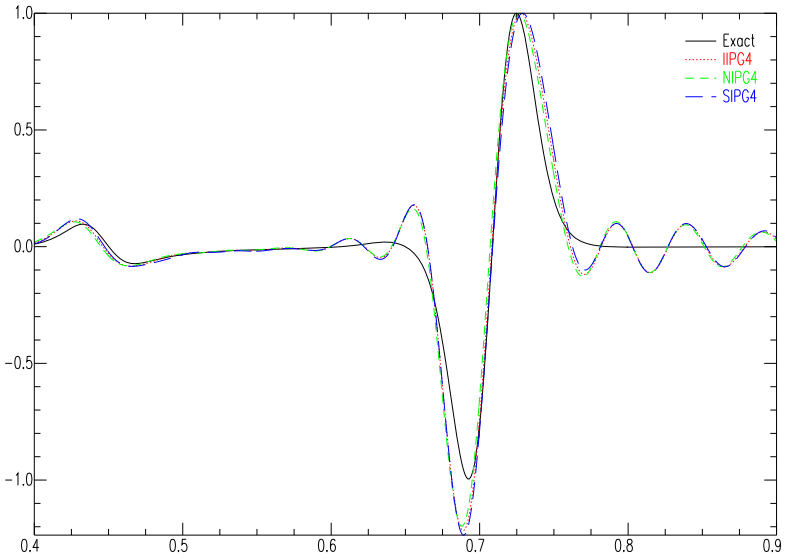

(b) z

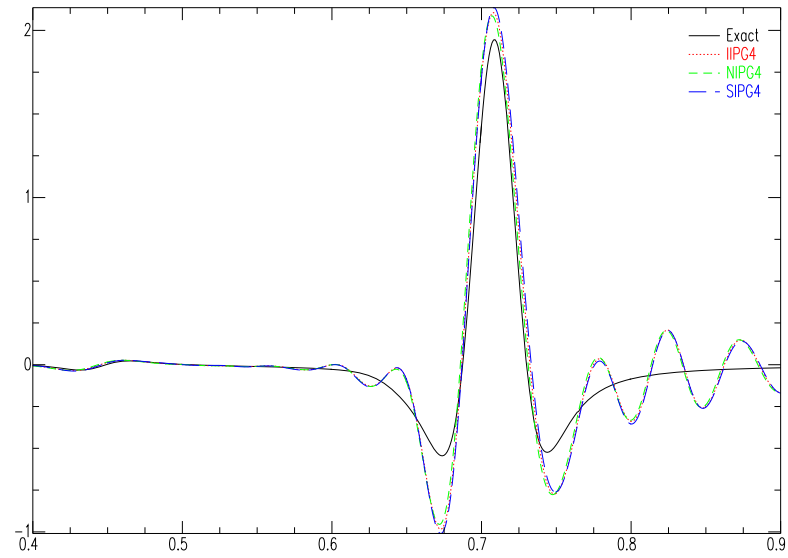

Figure 4.13: Comparison of synthetic seismograms from receiver 1 for Lamb's problem obtained using the different formulations of IP-DGM.

Synthetic Seismograms – Comparison of Time-Stepping Methods

(a) x

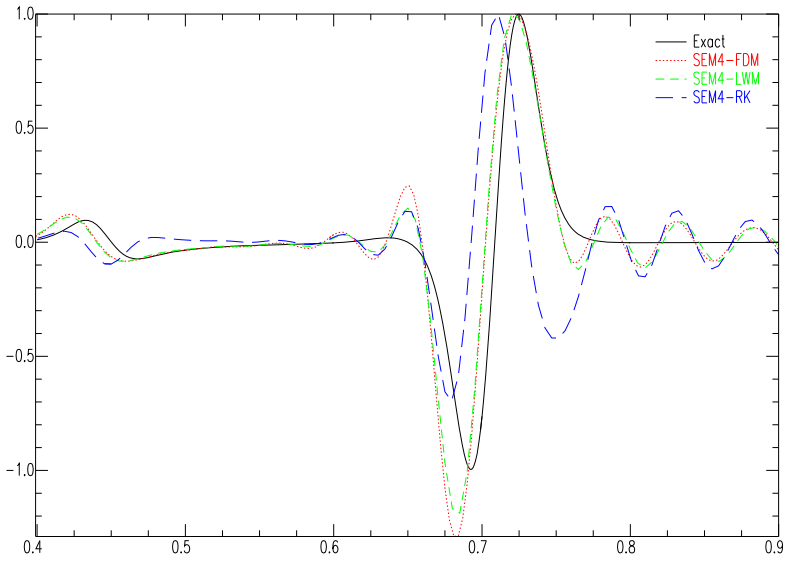

(b) z

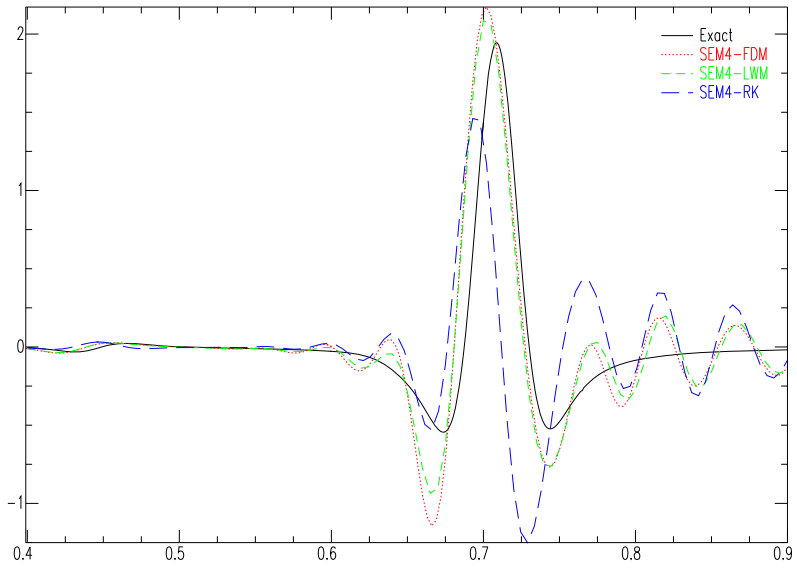

Figure 4.14: Synthetic seismograms from receiver 1 obtained using 4th degree SEM and three time-stepping methods: FDM, 4th order LWM and 4th order RK.

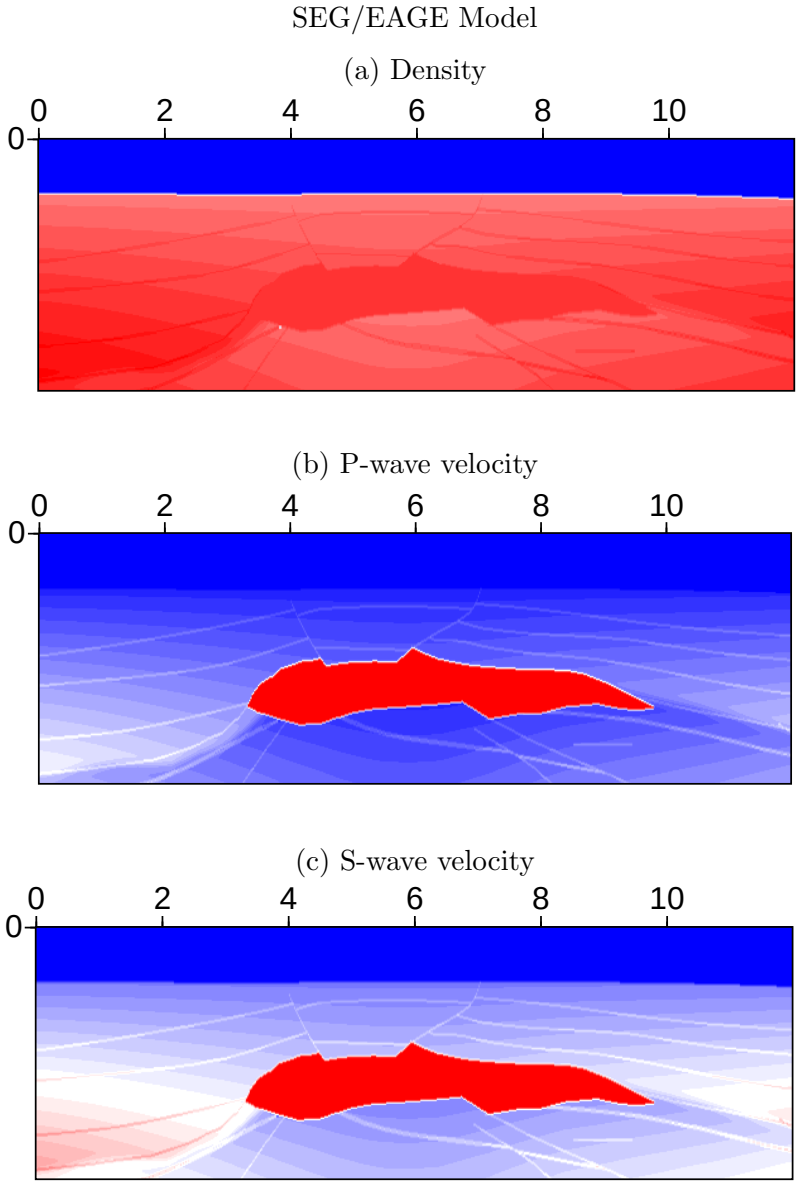

Figure 4.15: SEG/EAGE salt-dome model. The upper layer is an acoustic medium, and at the center of the domain there is a salt dome with a higher density, P- and S-wave velocities.

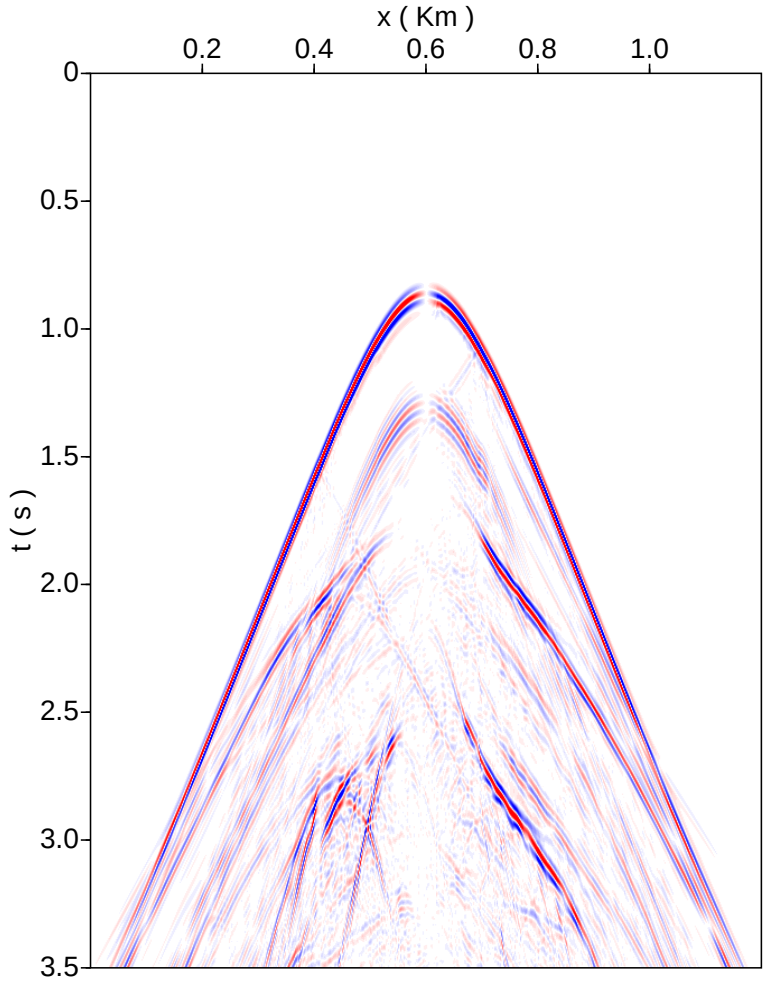

Figure 4.16: Synthetic traces using SEM of degree 4 for the SEG salt model, x component of displacement.

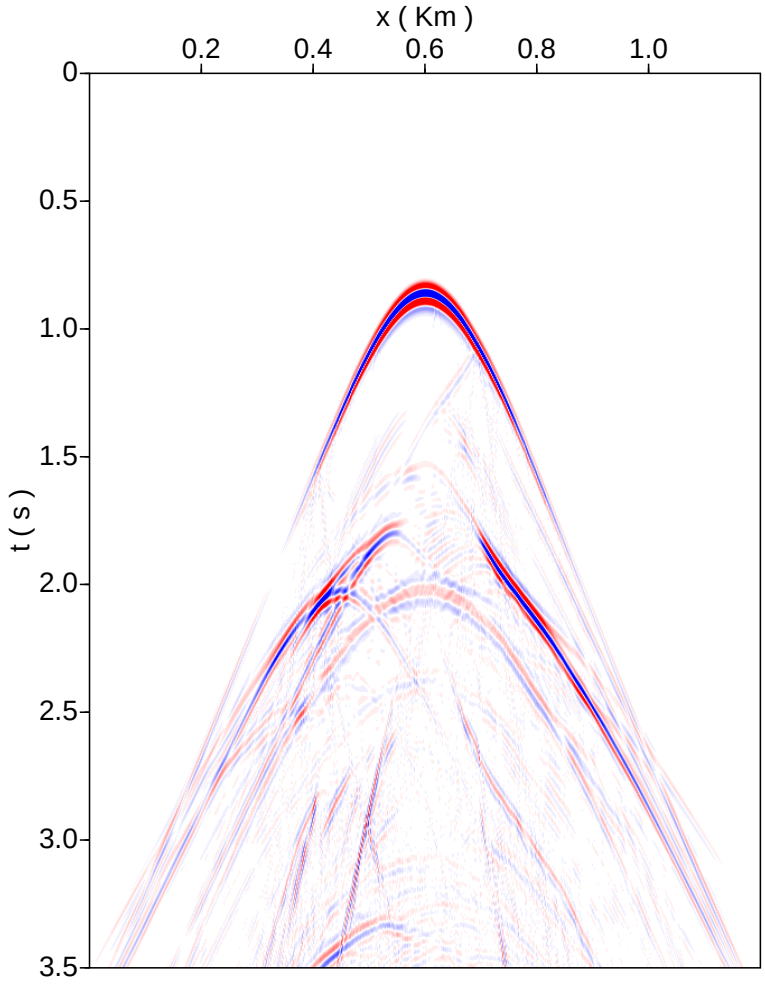

Figure 4.17: Synthetic traces using SEM of degree 4 for the SEG salt model, z component of displacement.

Chapter 5

Conclusions and Future Work

5.1 Conclusions

The SEM and IP-DGM were formulated and implemented for the numerical simulation of propagation of acoustic and elastic waves. The accuracy and stability of these methods were analyzed using a general formulation that allows for high-order basis functions and overcomes the difficulties due to irregular node spacing. The approach includes previous results of FEM for quadrilateral tensor-product elements and standard grid FDM as special cases. Furthermore, this approach can be used to analyze the grid dispersion in the semidiscrete case or the dispersion including the effects of the time stepping. However, the limitation of the grid dispersion analysis is that it assumes regular quadrilateral elements and it does not take into account the boundary conditions. Other restrictions of the analysis are that analytic solutions for arbitrary-order elements are not provided and that it was limited to the 2D case for tensor-product rectangular elements. Finally, the grid-dispersion results presented here are the minimum dispersion for each of the methods. In practical applications more dispersion may arise from boundary conditions, irregular elements or heterogeneities in the medium. The following remarks summarize the overall analysis:

- First-degree elastic FEM-CM and SEM introduce anisotropic errors and are very sensitive to Poisson's ratio.
- SEM, using the GLL nodes and quadrature rules, is an efficient way to lump

the mass matrix; it has the same accuracy or better than FEM-CM. FEM-ML introduces large and anisotropic errors for $\kappa \geq 3$; For $\kappa = 1, 2$ it is equivalent to SEM.

- SEM of order 4 or greater is an accurate and efficient method for propagating acoustic and elastic waves. Because of its low dispersion, the sampling ratio can be reduced to 4–5 nodes per wave length with a negligible loss of accuracy.

- A comparison of the high-order SEM with the staggered-grid FDM reveals that they are both suitable for models with liquid-solid interfaces. SEM has the advantages that it requires a lower sampling ratio, has a smaller dispersion and is isotropic.

- Among the different versions of IP-DGM, SIPG has attractive advantages over the other formulations. Namely, it allows for lower polynomial degree and sampling ratio to be used to get high accuracy. The results indicate that high accuracy and isotropy can be obtained using SIPG of degree 4 or greater with nodal basis functions and 4–5 grid-points per wave length.

- A comparison of the effect that different basis functions have on the accuracy of IP-DGM reveals that nodal basis functions using the GLL or Gauss nodes yield faster convergence rates than modal basis functions using the Legendre polynomials.

- The accuracy of IP-DGM and SEM were also compared. The SIPG method with nodal basis functions performs with practically the same accuracy as SEM. It should be noted that IP-DGM has the further advantage over SEM that it can handle non-conforming finite-element meshes (e.g. Sun & Wheeler, 2005; Käser & Dumbser, 2006).

- The time step required by the high-degree methods is slightly smaller that that of the lower-degree methods, taking into account that the high-degree methods require a smaller sampling ratio.

- IP-DGM require a time step approximately 4 times smaller than that of SEM in the acoustic case, and 6 times smaller in the elastic case. This, in addition to the fact that it requires more degrees of freedom for a given sampling ratio, makes IP-DGM much more expensive than SEM.

The above conclusions underline the potential of the FEM for seismic wave propagation, in particular SEM and SIPG of degree 4 or greater. These methods have negligible numerical dispersion and anisotropy, which makes them suitable for simulations of long propagation times.

5.2 Future Work

The analysis developed in this dissertation has provided answers to important questions in numerical wave propagation, however there are many open questions that deserve attention. Examples of the logical continuation of the analysis are the following:

- Extend the analysis to triangular elements in 2D and to cubic elements in 3D.

- Investigate the dispersion of other methods, for example, the flux formulation DGM and the Mixed FEM.

- Investigate further the generalized eigenvalue problem to understand the behavior of the spurious modes.

Furthermore, the development of the methods is an ongoing research effort. Some immediate goals include the implementation of the following features in the wave propagation code:

- Absorbing boundary conditions,
- Parallelization using MPI, and
- A more general description of the physical model, including topography and 3D.

Appendix

Appendix 1

Notation

Symbol	Description	Where it is defined
σ_{ij}	Stress tensor	eq. (2.1.2)
C_{ijkl}	Elastic tensor	eq. (2.1.2)
ε_{ij}	Strain tensor	eq. (2.1.2)
u_i	Displacement vector field	eq. (2.1.1)
p	Pressure field	eq. (2.1.5)
Ω	Physical domain of the wave equation	eq. (2.1.1)
$\partial\Omega$	Boundary of Ω	eq. (2.1.7)
Ω_h	Finite element partition of Ω	sec. 2.3
Γ_h	Set of faces between elements of Ω_h	sec. 2.3
Γ_D, Γ_N	Dirichlet and Neumann boundaries of Ω	eq. (2.1.7)
κ	Polynomial degree of the basis functions	sec. 2.2.3
m	Number of nodes in the elements	sec. 2.3.3
λ, μ	Lamé parameters	eq. (2.1.4)
α	P-wave velocity	eqs. (3.1.3) and (3.1.39)
β	S-wave velocity	eq. (3.1.39)
r	P- to S-wave velocity ratio	eq. (3.1.39)
ω_h	Angular frequency in the grid	eq. (3.1.5)
q	Stability parameter	eq. (3.3.1)
δ	Sampling ratio	eq. (3.1.28)
L	Wavelength	eq. (3.1.28)
θ	Incidence angle	eq. (3.3.2)
S	DGM parameter	eq. (2.3.6)
R	DGM penalty	eq. (2.3.6)
X^C, $\boldsymbol{X}^C$	Exact-solution spaces, continuous case	sec. 2.2.1 and 2.2.2
X^D, $\boldsymbol{X}^D$	Exact-solution spaces, discontinuous case	sec. 2.3.1 and 2.3.2
X_h^C, $\boldsymbol{X}_h^C$	FEM spaces	sec. 2.2.1 and 2.2.2
X_h^D, $\boldsymbol{X}_h^D$	DGM spaces	sec. 2.3.1 and 2.3.2

Table A1.1: Description of the symbols used.

Appendix 2

Grid Dispersion of the Finite Difference Methods

2.1 Acoustic Scheme

This scheme was described and analyzed in Alford et al. (1974); their results are revisit here for completeness. Substituting the derivatives in eq. (2.1.7) for second order finite difference operators yields

$$P_{l+1,m,n} - 2P_{l,m,n} + P_{l-1,m,n} = \frac{\alpha^2 \Delta t^2}{h^2} \left(P_{l,m+1,n} + P_{l,m-1,n} - 4P_{l,m,n} + P_{l,m,n+1} + P_{l,m,n-1} \right), \tag{A2.1.1}$$

where $P_{l,m,n} \approx p(t_l, x_m, z_n)$, $h = \Delta x = \Delta z$ is the grid spacing and Δt is the time step size. Using the plane wave assumption, then $P_{l,m,n} = AE_{l,m,n}$, where

$$E_{l,m,n} = \exp\left\{ i \left(k_x m h + k_z n h - \omega l \Delta t \right) \right\}, \tag{A2.1.2}$$

A is an arbitrary constant, ω is the angular frequency and $(k_x, k_z)^T$ is the wavenumber. Substituting in the finite difference scheme and making some simplifications yields

$$\sin\left(\frac{\omega_h \Delta t}{2} \right) = \frac{\alpha \Delta t}{h} \sqrt{ \sin^2\left(\frac{k_x h}{2} \right) + \sin^2\left(\frac{k_z h}{2} \right) }. \tag{A2.1.3}$$

Therefore, for this scheme to be stable, the following conditions needs to be satisfied

$$\frac{\alpha \Delta t}{h} \sqrt{ \sin^2\left(\frac{k_x h}{2} \right) + \sin^2\left(\frac{k_z h}{2} \right) } \leq \frac{\alpha \Delta t}{h} \sqrt{2} \leq 1 . \tag{A2.1.4}$$

Introducing the stability parameter, the stability condition can be written as $\mathrm{q} \leq 2^{-1/2}$. From eq. (A2.1.3), the angular frequency in the grid is given by

$$\omega_h = \frac{2}{\Delta t} \sin^{-1}\left(\mathrm{q}\sqrt{\sin^2\left(\frac{k_x h}{2}\right) + \sin^2\left(\frac{k_z h}{2}\right)}\right). \tag{A2.1.5}$$

Recall that $\omega_h = 2\pi\alpha_h/L$, where L is the wavelength and α_h is the velocity at which the wave travels in the grid. Defining the sampling ratio $s = h/L$, the dispersion relation is given by

$$\frac{\alpha_h}{\alpha} = \frac{1}{\pi s\ \mathrm{q}} \sin^{-1}\left(\mathrm{q}\sqrt{\sin^2(\pi s\cos\theta) + \sin^2(\pi s\sin\theta)}\right). \tag{A2.1.6}$$

2.2 Elastic Scheme

Following Kelly et al. (1976), substituting second order differential operators in eq. (2.1.8) yields

$$\begin{aligned} U^x_{l+1,m,n} - 2U^x_{l,m,n} + U^x_{l-1,m,n} &= \frac{\alpha^2\Delta t^2}{h^2}\left(U^x_{l,m+1,n} - 2U^x_{l,m,n} + U^x_{l,m-1,n}\right) \quad \text{(A2.2.1)}\\ +\frac{1}{4}\frac{\Delta t^2}{h^2}(\alpha^2-\beta^2)&\left(U^z_{l,m+1,n+1} - U^z_{l,m+1,n-1} - U^z_{l,m-1,n+1} + U^z_{l,m-1,n-1}\right)\\ &+\frac{\beta^2\Delta t^2}{h^2}\left(U^x_{l,m,n+1} - 2U^x_{l,m,n} + U^x_{l,m,n-1}\right)\\ U^z_{l+1,m,n} - 2U^z_{l,m,n} + U^z_{l-1,m,n} &= \frac{\alpha^2\Delta t^2}{h^2}\left(U^z_{l,m,n+1} - 2U^z_{l,m,n} + U^z_{l,m,n-1}\right) \quad \text{(A2.2.2)}\\ +\frac{1}{4}\frac{\Delta t^2}{h^2}(\alpha^2-\beta^2)&\left(U^x_{l,m+1,n+1} - U^x_{l,m+1,n-1} - U^x_{l,m-1,n+1} + U^x_{l,m-1,n-1}\right)\\ &+\frac{\beta^2\Delta t^2}{h^2}\left(U^z_{l,m+1,n} - 2U^z_{l,m,n} + U^z_{l,m-1,n}\right) \end{aligned}$$

where $U^x_{l,m,n} \approx u_x(t_l, x_m, z_n)$ and $U^z_{l,m,n} \approx u_z(t_l, x_m, z_n)$.

Substituting a plane wave solution, $U^x_{l,m,n} = A_1 E_{l,m,n}$ and $U^z_{l,m,n} = A_2 E_{l,m,n}$, where A_1 and A_2 are arbitrary constants, yields the following eigenvalue problem

$$\Lambda \begin{bmatrix} A_1 \\ A_2 \end{bmatrix} = \begin{bmatrix} \Gamma & \Phi \\ \Phi & \Upsilon \end{bmatrix} \begin{bmatrix} A_1 \\ A_2 \end{bmatrix} \tag{A2.2.3}$$

where

$$\Lambda = \frac{h^2}{\Delta t^2}\sin^2\left(\frac{\omega\Delta t}{2}\right) \tag{A2.2.4}$$

$$\Gamma = \alpha^2\sin^2\left(\frac{k_x h}{2}\right) + \beta^2\sin^2\left(\frac{k_z h}{2}\right) \tag{A2.2.5}$$

$$\Upsilon = \alpha^2\sin^2\left(\frac{k_z h}{2}\right) + \beta^2\sin^2\left(\frac{k_x h}{2}\right) \tag{A2.2.6}$$

$$\Phi = \frac{\alpha^2-\beta^2}{4}\sin\left(k_x h\right)\sin\left(k_z h\right)\ . \tag{A2.2.7}$$

The system has non-trivial solutions if $\Lambda = \Lambda_1$ or $\Lambda = \Lambda_2$, where

$$\begin{aligned}\Lambda_1 &= \alpha^2\left[\sin^2\left(\frac{k_x h}{2}\right) + \sin^2\left(\frac{k_z h}{2}\right)\right] \\ &- (\alpha^2-\beta^2)\sin^2\left(\frac{k_x h}{2}\right)\sin^2\left(\frac{k_z h}{2}\right)\end{aligned} \tag{A2.2.8}$$

$$\begin{aligned}\Lambda_2 &= \beta^2\left[\sin^2\left(\frac{k_x h}{2}\right) + \sin^2\left(\frac{k_z h}{2}\right)\right] \\ &+ (\alpha^2-\beta^2)\sin^2\left(\frac{k_x h}{2}\right)\sin^2\left(\frac{k_z h}{2}\right)\ .\end{aligned} \tag{A2.2.9}$$

From $\frac{\Delta t^2}{h^2}|\Lambda_1| \leq 1$ and noting that $|\Lambda_1| \leq \alpha^2+\beta^2$, then

$$\frac{\Delta t^2}{h^2}|\Lambda_1| \leq \frac{\Delta t^2}{h^2}\left(\alpha^2+\beta^2\right) = \frac{\alpha^2\Delta t^2}{h^2}\left(1+\frac{\beta^2}{\alpha^2}\right) \leq 1, \tag{A2.2.10}$$

therefore the stability condition for this scheme is

$$\mathrm{q} = \frac{\alpha\Delta t}{h} \leq \left(1+\frac{\beta^2}{\alpha^2}\right)^{-1/2}\ . \tag{A2.2.11}$$

The same stability condition is obtained using Λ_2. This result was first obtained in Alterman & Lowenthal (1970) using a different approach.

From eqs. (A2.2.4) and (A2.2.8), the grid dispersion relation of the P-wave is given by

$$\frac{\alpha_h}{\alpha} = \frac{1}{\pi\ s\ \mathrm{q}}\sin^{-1}\left(\frac{\Delta t}{h}\sqrt{\Lambda_1}\right)\ , \tag{A2.2.12}$$

and using eq. (A2.2.9), the grid dispersion of the S-wave is given by

$$\frac{\beta_h}{\beta} = \frac{r}{\pi\ s\ \mathrm{q}} \sin^{-1}\left(\frac{\Delta t}{h}\sqrt{\Lambda_2}\right) . \tag{A2.2.13}$$

Similar expressions were given in Cohen (2002). Note that both dispersion relations are functions of the P- and S-wave velocities.

2.3 Staggered Grid Scheme

There are several formulations for this scheme, the most common being the velocity-stress formulation (Virieux, 1984, 1986; Levander, 1988; Graves, 1996; Minkoff, 2002) in which the time derivative of the equation of Hooke's law is taken together with the equation of motion and solved for particle velocity and stress. It can be shown that the stability and grid dispersion results shown in this appendix hold without modifications for the velocity-stress, the stress-displacement or the displacement-velocity-stress formulations (Moczo et al., 2000a). For simplicity, the stress-displacement formulation will be used, which is given by

$$\rho\partial_{tt}\mathbf{u} = \nabla\cdot\sigma \tag{A2.3.1}$$

$$\sigma = \lambda\mathbf{I}\nabla\cdot\mathbf{u} + \mu(\nabla\mathbf{u} + \nabla\mathbf{u}^T) , \tag{A2.3.2}$$

where σ is the stress tensor. For this methods, separate grids for the displacement and stress are defined, where one grid is staggered with respect to the other. In the 2D case, the approximations are given by

$$U^x_{l,m+1/2,n} \approx u_x(t_l, x_{m+1/2}, z_n), \tag{A2.3.3}$$

$$U^z_{l,m,n+1/2} \approx u_z(t_l, x_m, z_{n+1/2}) \tag{A2.3.4}$$

$$T^{xx}_{l,m,n} \approx \sigma_{xx}(t_l, x_m, z_n), \tag{A2.3.5}$$

$$T^{zz}_{l,m,n} \approx \sigma_{zz}(t_l, x_m, z_n), \tag{A2.3.6}$$

$$T^{xz}_{l,m+1/2,n+1/2} \approx \sigma_{xz}(t_l, x_{m+1/2}, z_{n+1/2}) . \tag{A2.3.7}$$

Using second order differential operators, yields

$$
\begin{aligned}
U^x_{l+1,m+1/2,n} &= 2U^x_{l,m+1/2,n} - U^x_{l-1,m+1/2,n} && \text{(A2.3.8)}\\
&+ \frac{\Delta t^2}{h\rho}\Big(T^{xx}_{l,m+1,n} - T^{xx}_{l,m,n}\\
&+ T^{xz}_{l,m+1/2,n+1/2} - T^{xz}_{l,m+1/2,n-1/2}\Big)\\
U^z_{l+1,m,n+1/2} &= 2U^z_{l,m,n+1/2} - U^z_{l-1,m,n+1/2} && \text{(A2.3.9)}\\
&+ \frac{\Delta t^2}{h\rho}\Big(T^{xz}_{l,m+1/2,n+1/2} - T^{xz}_{l,m-1/2,n+1/2}\\
&+ T^{zz}_{l,m,n+1} - T^{zz}_{l,m,n}\Big)\\
T^{xx}_{l,m,n} &= \frac{\lambda+2\mu}{h}\left(U^x_{l,m+1/2,n} - U^x_{l,m-1/2,n}\right) && \text{(A2.3.10)}\\
&+ \frac{\lambda}{h}\left(U^z_{l,m,n+1/2} - U^z_{l,m,n-1/2}\right)\\
T^{zz}_{l,m,n} &= \frac{\lambda}{h}\left(U^x_{l,m+1/2,n} - U^x_{l,m-1/2,n}\right) && \text{(A2.3.11)}\\
&+ \frac{\lambda+2\mu}{h}\left(U^z_{l,m,n+1/2} - U^z_{l,m,n-1/2}\right)\\
T^{xz}_{l,m+1/2,n+1/2} &= \frac{\mu}{h}\Big(U^x_{l,m+1/2,n+1} - U^x_{l,m+1/2,n} && \text{(A2.3.12)}\\
&\quad + U^z_{l,m+1,n+1/2} - U^z_{l,m,n+1/2}\Big)\ .
\end{aligned}
$$

Using the plane-wave assumption, eq. (A2.1.2), then

$$U^x_{l,m,n} = A_1 E_{l,m,n}, \quad U^z_{l,m,n} = A_2 E_{l,m,n}, \qquad \text{(A2.3.13)}$$

$$T^{xx}_{l,m,n} = B_1 E_{l,m,n}, \quad T^{zz}_{l,m,n} = B_2 E_{l,m,n}, \quad T^{xz}_{l,m,n} = B_3 E_{l,m,n}\ . \qquad \text{(A2.3.14)}$$

Substituting in the staggered-grid scheme yields

$$\begin{bmatrix} A_1 \\ A_2 \end{bmatrix} \sin^2\left(\frac{\omega\Delta t}{2}\right) = \qquad \text{(A2.3.15)}$$

$$-\frac{i\Delta t}{2\rho h}\begin{bmatrix} \sin\left(\frac{k_x h}{2}\right) & 0 & \sin\left(\frac{k_z h}{2}\right) \\ 0 & \sin\left(\frac{k_z h}{2}\right) & \sin\left(\frac{k_x h}{2}\right) \end{bmatrix}\begin{bmatrix} B_1 \\ B_2 \\ B_3 \end{bmatrix} \qquad \text{(A2.3.16)}$$

$$\begin{bmatrix} B_1 \\ B_2 \\ B_3 \end{bmatrix} = \frac{2i}{h} \begin{bmatrix} \rho\alpha^2 \sin\left(\frac{k_x h}{2}\right) & \lambda \sin\left(\frac{k_z h}{2}\right) \\ \lambda \sin\left(\frac{k_x h}{2}\right) & \rho\alpha^2 \sin\left(\frac{k_z h}{2}\right) \\ \rho\beta^2 \sin\left(\frac{k_z h}{2}\right) & \rho\beta^2 \sin\left(\frac{k_x h}{2}\right) \end{bmatrix} \begin{bmatrix} A_1 \\ A_2 \end{bmatrix} . \quad \text{(A2.3.17)}$$

Substituting eq. (A2.3.17) in (A2.3.16) yields the following 2×2 system

$$\Lambda \begin{bmatrix} A_1 \\ A_2 \end{bmatrix} = \begin{bmatrix} \Gamma & \Phi \\ \Phi & \Upsilon \end{bmatrix} \begin{bmatrix} A_1 \\ A_2 \end{bmatrix} , \quad \text{(A2.3.18)}$$

where

$$\Lambda = \frac{h^2}{\Delta t^2} \sin^2\left(\frac{\omega \Delta t}{2}\right) \quad \text{(A2.3.19)}$$

$$\Gamma = \alpha^2 \sin^2\left(\frac{k_x h}{2}\right) + \beta^2 \sin^2\left(\frac{k_z h}{2}\right) \quad \text{(A2.3.20)}$$

$$\Upsilon = \alpha^2 \sin^2\left(\frac{k_z h}{2}\right) + \beta^2 \sin^2\left(\frac{k_x h}{2}\right) \quad \text{(A2.3.21)}$$

$$\Phi = (\alpha^2 - \beta^2) \sin\left(\frac{k_x h}{2}\right) \sin\left(\frac{k_z h}{2}\right) . \quad \text{(A2.3.22)}$$

The system has non-trivial solutions if $\Lambda = \Lambda_1$ or $\Lambda = \Lambda_2$, where

$$\Lambda_1 = \alpha^2 \left[\sin^2\left(\frac{k_x h}{2}\right) + \sin^2\left(\frac{k_z h}{2}\right)\right] , \quad \text{(A2.3.23)}$$

$$\Lambda_2 = \beta^2 \left[\sin^2\left(\frac{k_x h}{2}\right) + \sin^2\left(\frac{k_z h}{2}\right)\right] . \quad \text{(A2.3.24)}$$

From these eigenvalues, two stability conditions are obtained, namely

$$\frac{\alpha \Delta t}{h}\sqrt{2} \leq 1 \quad \text{and} \quad \frac{\beta \Delta t}{h}\sqrt{2} \leq 1 . \quad \text{(A2.3.25)}$$

The first one is more restrictive, thus the stability condition is $\mathrm{q}\sqrt{2} \leq 1$. The grid dispersion relation for the P-wave is related to Λ_1, and is given by

$$\frac{\alpha_h}{\alpha} = \frac{r}{\pi \, \mathrm{q} \, s} \sin^{-1}\left[\mathrm{q}\sqrt{\sin^2\left(\frac{\pi s \cos\theta}{r}\right) + \sin^2\left(\frac{\pi s \sin\theta}{r}\right)}\right] , \quad \text{(A2.3.26)}$$

and from Λ_2, the dispersion relation for the S-wave is

$$\frac{\beta_h}{\beta} = \frac{r}{\pi \, \mathrm{q} \, s} \sin^{-1}\left[\frac{\mathrm{q}}{r}\sqrt{\sin^2(\pi s \cos\theta) + \sin^2(\pi s \sin\theta)}\right] , \quad \text{(A2.3.27)}$$

where $r = \alpha/\beta$. A similar analysis can be performed using 4^{th} order differential operators. The stability condition for the 4^{th} order staggered-grid scheme is $\mathrm{q} \leq \frac{6}{7\sqrt{2}}$, and the grid dispersion relations are

$$\begin{aligned}
\frac{\alpha_h}{\alpha} &= \frac{7\sqrt{2}}{6}\frac{r}{\pi\ \mathrm{q}\ s}\sin^{-1}\left[\frac{6}{7\sqrt{2}}\mathrm{q}\left\{\frac{9}{8}\sin^2\left(\frac{\pi s\cos\theta}{r}\right)+\frac{9}{8}\sin^2\left(\frac{\pi s\sin\theta}{r}\right)\right.\right. \\
&\quad \left.\left.-\frac{1}{24}\sin^2\left(3\frac{\pi s\cos\theta}{r}\right)-\frac{1}{24}\sin^2\left(3\frac{\pi s\sin\theta}{r}\right)\right\}^{1/2}\right], \qquad \text{(A2.3.28)} \\
\frac{\beta_h}{\beta} &= \frac{7\sqrt{2}}{6}\frac{r}{\pi\ \mathrm{q}\ s}\sin^{-1}\left[\frac{6}{7\sqrt{2}}\frac{\mathrm{q}}{r}\left\{\frac{9}{8}\sin^2\left(\pi s\cos\theta\right)+\frac{9}{8}\sin^2\left(\pi s\sin\theta\right)\right.\right. \\
&\quad \left.\left.-\frac{1}{24}\sin^2\left(3\pi s\cos\theta\right)-\frac{1}{24}\sin^2\left(3\pi s\sin\theta\right)\right\}^{1/2}\right]. \qquad \text{(A2.3.29)}
\end{aligned}$$

The stability condition for the 2D case with second order differential operators was first given in Virieux (1986), and for the fourth order differential operators was given in Graves (1996) and Moczo et al. (2000a). The grid dispersion relations where derived in Moczo et al. (2000a) for the second and fourth order schemes. The 3D case is also analyzed in Moczo et al. (2000b). Note that the stability conditions for the P- and S-waves, eq. (A2.3.25), depend on the P- and S-wave velocities alone and that the grid dispersion relations (A2.3.26) and (A2.3.27) depend on the ratio of P- to S-wave velocity.

Appendix 3

Condition Number of the Mass Matrix in the Discontinuous Galerkin Method

In this appendix, the condition numbers of the mass matrix for the IP-DGM will discussed. The results using the three types of proposed basis functions and up to a polynomial degree of 10 assuming a constant density are summarized in Table A3.1. Note that the table shows the condition numbers for the mass matrix in 1D; the condition numbers in 2D and 3D will be the square and cube respectively for each method and degree.

Recall that the entries of the 1D mass matrix in element E are given by

$$M_{ij} = \int_E \phi_i^E \phi_j^E \tag{A3.0.1}$$

and that the condition number using the 2-norm is given by the ratio of the largest eigenvalue to the smallest eigenvalue (Watkins, 2002), which are trivially computed for a diagonal matrix. Also note that the condition number is independent of the size of the element, therefore an element of unit length will be considered for succinctness.

Let us first consider the Legendre basis. The diagonal entries of the mass matrix in 1D, assuming that the basis functions have the usual ordering, are given by

$$M_{ii} = \int_E (\phi_i^E)^2 = 2(i-1)+1, \quad i = 1, \ldots, \kappa+1. \tag{A3.0.2}$$

Therefore the largest eigenvalue is equal to $2\kappa+1$, the smallest is equal to 1 and the condition number is given by $\text{cond}(M_{ii}) = 2\kappa+1$.

Degree	Legendre	GLL	Gauss
1	3	1	1
2	5	4	1.6
3	7	5	1.87
4	9	7.11	2.40
5	11	8.32	2.73
6	13	10.24	3.23
7	15	11.55	3.58
8	17	13.37	4.06
9	19	14.74	4.43
10	21	16.51	4.90

Table A3.1: Condition number of the mass matrix in 1D assuming a constant density inside the elements. The condition numbers in 2D and 3D are given by the square or cube of these values.

Considering now the GLL or Gauss basis, the diagonal entries of the mass matrix are given by

$$M_{ii} = \sum_{k=1}^{n} w_k (\phi_i^E(x_k))^2 = w_i, \quad i = 1, \ldots, \kappa + 1. \tag{A3.0.3}$$

where n is the quadrature order, and x_k and w_k are the quadrature nodes and weights. Recall that the basis functions are defined using the Lagrange polynomials and the quadrature nodes, and that for the GLL basis the nodes and weights are those of the GLL quadrature rules, whereas for the Gauss basis those of the Gauss quadrature rules. The condition number of the mass matrix for the nodal basis is therefore given by $\text{cond}(M_{ii}) = \max_k(w_k)/\min_k(w_k)$.

It should be noted that the condition number does not create any problems in the implementation of these basis functions because the inversion of a diagonal matrix is a stable procedure. The only concern is the accuracy.

Index

Bibliography

Ainsworth, M., 2004a. Discrete Dispersion Relation for hp-Version Finite Element Approximation at High Wave Number, *SIAM Journal on Numerical Analysis*, **42**(2), 553–575.

Ainsworth, M., 2004b. Dispersive and dissipative behaviour of high order discontinuous Galerkin finite element methods, *Journal of Computational Physics*, **198**(1), 106–130.

Ainsworth, M., Monk, P., & Muniz, W., 2006. Dispersive and Dissipative Properties of Discontinuous Galerkin Finite Element Methods for the Second-Order Wave Equation, *Journal of Scientific Computing*, **27**(1), 5–40.

Aki, K. & Richards, P., 2002. *Quantitative Seismology*, University Science Books, Sausalito, California, 2nd edn.

Alford, R., Kelly, K., & Boore, D., 1974. Accuracy of finite-difference modeling of the acoustic wave equation, *Geophysics*, **39**(6), 834–842.

Alterman, Z. & Karal, F., 1968. Propagation of elastic waves in layered media by finite difference methods, *Bull. Seismol. Soc. Am.*, **58**(1), 367–398.

Alterman, Z. & Lowenthal, D., 1970. Seismic waves in a quarter and three-quarter plane, *Geophys. J. R. Astron. Soc.*, **20**, 101–126.

Bao, H., Bielak, J., Ghattas, O., Kallivokas, L., O'Hallaron, D., Shewchuk, J., & Xu, J., 1998. Large-scale simulation of elastic wave propagation in heterogeneous media on parallel computers, *Computer Methods in Applied Mechanics and Engineering*, **152**(1-2), 85–102.

Bécache, E., Joly, P., & Tsogka, C., 2000. An Analysis of New Mixed Finite Elements for the Approximation of Wave Propagation Problems, *SIAM Journal on Numerical Analysis*, **37**, 1053–1084.

Bécache, E., Joly, P., & Tsogka, C., 2002. A new family of mixed finite elements for the linear elastodynamic problem, *SIAM Journal on Numerical Analysis*, **39**(6), 2109–2132.

Brenner, S. & Scott, L., 2002. *The Mathematical Theory of Finite Element Methods*, Texts in Applied Mathematics, Springer.

Chaljub, E., Komatitsch, D., Vilotte, J.-P., Capdeville, Y., Valette, B., & Festa, G., 2007. Spectral element analysis in seismology, in *Advances in Wave Propagation in Heterogeneous Media*, Advances in Geophysics, pp. 365–419, eds Wu, R.-S. & Maupin, V., Elsevier.

Chopra, A. K., Dibaj, M., Clough, R. W., Penzien, J., & Seed, H. B., 1969. Earthquake analysis of earth dams, *4th World Conf. Earthquake Engineering*, pp. A5–55.

Chung, E. & Engquist, B., 2006. Optimal Discontinuous Galerkin Methods for Wave Propagation, *SIAM Journal on Numerical Analysis*, **44**(5), 2131–2158.

Cockburn, B. & Shu, C., 1989. TVB Runge-Kutta Local Projection Discontinuous Galerkin Finite Element Method for Conservation Laws II: General Framework, *Mathematics of Computation*, **52**(186), 411–435.

Cockburn, B. & Shu, C.-W., 1998. The Runge-Kutta discontinuous Galerkin method for conservation laws V: multidimensional systems, *Journal of Computational Physics*, **141**(2), 199–224.

Cockburn, B., Lin, S., & Shu, C., 1989. TVB Runge-Kutta local projection discontinuous Galerkin finite element method for conservation laws III: one-dimensional systems, *Journal of Computational Physics*, **84**(1), 90–113.

Cockburn, B., Hou, S., & Shu, C.-W., 1990. The Runge-Kutta Local Projection Discontinuous Galerkin Finite Element Method for Conservation Laws. IV: The Multidimensional Case, *Mathematics of Computation*, **54**(190), 545–581.

Cohen, G., 2002. *Higher-Order Numerical Methods for Transient Wave Equations*, Scientific Computation, Springer-Verlag.

Cohen, G. & Fauqueux, S., 2000. Mixed finite elements with mass-lumping for the transient wave equation, *Journal of Computational Acoustics*, **8**(1), 171–188.

Cohen, G. & Fauqueux, S., 2005. Mixed spectral finite elements for the linear elasticity system in unbounded domains, *SIAM Journal on Scientific Computing*, **26**(3), 864–884.

Dablain, M. A., 1986. The application of high-order differencing to the scalar wave equation, *Geophysics*, **51**(1), 54–66.

Darlow, B., 1980. *A Penalty-Galerkin Method for Solving the Miscible Displacement Problem*, Ph.D. thesis, Rice University, Houston, Texas.

Dawson, C., Sun, S., & Wheeler, M., 2004. Compatible algorithms for coupled flow and transport, *Computer Methods in Applied Mechanics and Engineering*, **193**(23-26), 2565–2580.

De Basabe, J. D. & Sen, M. K., 2007. Grid dispersion and stability criteria of some common finite-element methods for acoustic and elastic wave equations, *Geophysics*, **72**(6), T81–T95.

De Basabe, J. D., Sen, M. K., & Wheeler, M. F., 2008. The Interior Penalty Discontinuous Galerkin Method for Elastic Wave Propagation: Grid Dispersion, *Geophysical Journal International*, **175**(1), 83–93.

de la Puente, J., Käser, M., Dumbser, M., & Igel, H., 2007. An arbitrary high-order discontinuous Galerkin method for elastic waves on unstructured meshes – IV. Anisotropy, *Geophysical Journal International*, **169**(3), 1210–1228.

Dormy, E. & Tarantola, A., 1995. Numerical simulation of elastic wave propagation using a finite volume method, *Journal of Geophysical Research*, **100**(B2), 2123–2134.

Dubiner, M., 1991. Spectral methods on triangles and other domains, *Journal of Scientific Computing*, **6**(4), 345–390.

Dumbser, M. & Käser, M., 2006. An arbitrary high-order discontinuous Galerkin method for elastic waves on unstructured meshes – II. The three-dimensional isotropic case, *Geophysical Journal International*, **167**(1), 319–336.

Dumbser, M. & Munz, C.-D., 2006. Building Blocks for Arbitrary High Order Discontinuous Galerkin Schemes, *Journal of Scientific Computing*, **27**(1-3), 215–230.

Dumbser, M., Käser, M., & de la Puente, J., 2007a. Arbitrary high-order finite volume schemes for seismic wave propagation on unstructured meshes in 2D and 3D, *Geophysical Journal International*, **171**(2), 665–694.

Dumbser, M., Käser, M., & Toro, E., 2007b. An arbitrary high-order Discontinuous Galerkin method for elastic waves on unstructured meshes – V. Local time stepping and p-adaptivity, *Geophysical Journal International*, **171**(2), 695–717.

Dupont, T., 1973. L2-Estimates for Galerkin Methods for Second Order Hyperbolic Equations, *SIAM Journal on Numerical Analysis*, **10**(5), 880–889.

Fauqueux, S., 2003. *Eléments finis mixtes spectraux et couches absorbantes parfaitement adaptées pour la propagation d'ondes élastiques en régime transitoire*, Ph.D. thesis, Université de Paris, IX-Dauphine.

Gottlieb, S., 2005. On high order strong stability preserving runge-kutta and multi step time discretizations, *Journal of Scientific Computing*, **25**(1), 105–128.

Graves, R., 1996. Simulating seismic wave propagation in 3D elastic media using staggered-grid finite differences, *Bull. Seismol. Soc. Am.*, **86**(4), 1091–1106.

Grote, M., Schneebeli, A., & Schotzau, D., 2006. Discontinuous Galerkin Finite Element Method for the Wave Equation, *SIAM Journal on Numerical Analysis*, **44**(6), 2408–2431.

Hu, F., Hussaini, M., & Rasitarinera, P., 1999. An analysis of the discontinuous Galerkin method for wave propagation problems, *Journal of Computational Physics*, **151**(2), 921–946.

Hughes, T. J. R., 2000. *The Finite Element Method*, Dover Publications, Mineola, New York, 2nd edn.

Jenkins, E., Riviere, B., & Wheeler, M., 2002. A priori error estimates for mixed finite element approximations of the acoustic wave equation, *SIAM Journal on Numerical Analysis*, **40**(5), 1698–1715.

Jund, S. & Salmon, S., 2007. Arbitrary High-Order Finite Element Schemes and High-Order Mass Lumping, *International Journal of Applied Mathematics and Computer Science*, **17**(3), 375–393.

Karniadakis, G. & Sherwin, S., 1999. *Spectral/hp Element Methods for Computational Fluid Dynamics*, Numerical Mathematics and Scientific Computation, Oxford Uiversity Press.

Käser, M. & Dumbser, M., 2006. An arbitrary high-order discontinuous Galerkin method for elastic waves on unstructured meshes – I. The two-dimensional isotropic case with external source terms, *Geophysical Journal International*, **166**(2), 855–877.

Käser, M., Dumbser, M., de la Puente, J., & Igel, H., 2007a. An arbitrary high-order discontinuous Galerkin method for elastic waves on unstructured meshes – III. Viscoelastic attenuation, *Geophysical Journal International*, **168**(1), 224–242.

Käser, M., Mai, P., & Dumbser, M., 2007b. Accurate Calculation of Fault-Rupture Models Using the High-Order Discontinuous Galerkin Method on Tetrahedral Meshes, *Bulletin of the Seismological Society of America*, **97**(5), 1570–1586.

Kelly, K., Ward, R., Treitel, S., & Alford, R., 1976. Synthetic seismograms - A finite-difference approach, *Geophysics*, **41**(1), 2–27.

Komatitsch, D. & Tromp, J., 1999. Introduction to the spectral element method for three-dimensional seismic wave propagation, *Geophysical Journal International*, **139**(3), 806–822.

Komatitsch, D. & Tromp, J., 2002a. Spectral-element simulations of global seismic wave propagation-I. Validation, *Geophysical Journal International*, **149**(2), 390–412.

Komatitsch, D. & Tromp, J., 2002b. Spectral-element simulations of global seismic wave propagation-II. Three-dimensional models, oceans, rotation and self-gravitation, *Geophysical Journal International*, **150**(1), 303–318.

Komatitsch, D. & Vilotte, J., 1998. The spectral-element method: an efficient tool to simulate the seismic response of 2D and 3D geological structures, *Bulletin of the Seismological Society of America*, **88**(2), 368–392.

Komatitsch, D., Ritsema, J., & Tromp, J., 2002. The spectral-element method, Beowulf computing, and global seismology, *Science*, **298**(5599), 1737–1742.

Komatitsch, D., Liu, Q., Tromp, J., Süss, P., Stidham, C., & Shaw, J., 2004. Simulations of Ground Motion in the Los Angeles Basin Based upon the Spectral-Element Method, *Bulletin of the Seismological Society of America*, **94**(1), 187–206.

Komatitsch, D., Tsuboi, S., & Tromp, J., 2005. The spectral-element method in seismology, *Geophysical Monograph*, **157**, 205–227.

Kubatko, E., Westerink, J., & Dawson, C., 2007. Semi discrete discontinuous Galerkin methods and stage-exceeding-order, strong-stability-preserving Runge-Kutta time discretizations, *Journal of Computational Physics*, **222**(2), 832–848.

Lamb, H., 1904. On the Propagation of Tremors over the Surface of an Elastic Solid, *Philosophical Transactions of the Royal Society of London*, **203**, 1–42.

Lax, P. D. & Wendroff, B., 1964. Difference schemes for hyperbolic equations with high order of accuracy, *Communications on Pure and Applied Mathematics*, **17**(3), 381–398.

Levander, A., 1988. Fourth-order finite-difference P-SV seismograms, *Geophysics*, **53**(11), 1425–1436.

Li, B. Q., 2006. *Discontinuous Finite Elements in Fluid Dynamics and Heat Transfer*, Computational Fluid and Solid Mechanics, Springer.

Lysmer, J. & Drake, L., 1972. A finite element method for seismology, in *Methods in Computational Physics*, vol. 11, pp. 181–216, Academic Press.

Madariaga, R., 1976. Dynamics of an expanding circular fault, *Bull. Seismol. Soc. Am.*, **66**(3), 639–666.

Marfurt, K. J., 1984. Accuracy of finite-difference and finite-element modeling of the scalar and elastic wave equations, *Geophysics*, **49**(5), 533–549.

Minkoff, S., 2002. Spatial parallelism of a 3D finite difference velocity-stress elastic wave propagation code, *SIAM J. Sci. Comput.*, **24**(1), 1–19.

Mitchell, A. & Griffiths, D., 1980. *The Finite Difference Method in Partial Differential Equations*, John Wiley and Sons.

Moczo, P., Kristek, J., & Bystricky, E., 2000a. Stability and grid dispersion of the P-SV 4^{th}-order staggered-grid finite-difference scheme, *Studia Geoph. et Geod.*, **44**, 381–402.

Moczo, P., Kristek, J., & Halada, L., 2000b. 3D fourth-order staggered-grid finite-difference schemes: Stability and grid dispersion, *Bull. Seismol. Soc. Am.*, **90**(3), 587–603.

Mulder, W. A., 1999. Spurious modes in finite-element discretizations of the wave equation may not be all that bad, *Applied Numerical Mathematics*, **30**(4), 425–445.

Mullen, R. & Belytschko, T., 1982. Dispersion analysis of finite element semidiscretizations of the two-dimensional wave equation, *International Journal for Numerical Methods in Engineering*, **18**(1), 11–29.

Patera, A. T., 1984. A spectral element method for fluid dynamics: Laminar flow in a channel expansion, *Journal of Computational Physics*, **54**(3), 468–488.

Priolo, E., 2001. Earthquake Ground Motion Simulation Through the 2-D Spectral Element Method, *Journal of Computational Acoustics*, **9**(4), 1561–1581.

Reed, W. & Hill, T., 1973. Triangular mesh methods for the neutron transport equation, *Los Alamos Scientific Laboratory Technical Report*, **LA-UR-73-479**.

Rivière, B. & Wheeler, M., 2001. Discontinuous finite element methods for acoustic and elastic wave problems. part I: Semidiscrete error estimates, *TICAM report*, **0**(01-02), 1–12.

Rivière, B., Wheeler, M., & Girault, V., 1999. Improved energy estimates for interior penalty, constrained and discontinuous Galerkin methods for elliptic problems. Part I, *Computational Geosciences*, **3**(3), 337–360.

Rivière, B., Wheeler, M., & Girault, V., 2001. A Priori Error Estimates for Finite Element Methods Based on Discontinuous Approximation Spaces for Elliptic Problems, *SIAM Journal on Numerical Analysis*, **39**(3), 902–931.

Schwartzkopff, T., Munz, C., Toro, E., & Millington, R., 2001. The ADER approach in 2D, *Discrete Modelling and Discrete Algorithms on Continuum Mechanics*, pp. 207–216.

Schwartzkopff, T., Munz, C., & Toro, E., 2002. ADER: A High-Order Approach for Linear Hyperbolic Systems in 2D, *Journal of Scientific Computing*, **17**(1), 231–240.

Schwartzkopff, T., Dumbser, M., & Munz, C., 2004. Fast high order ADER schemes for linear hyperbolic equations, *Journal of Computational Physics*, **197**(2), 532–539.

Seriani, G. & Priolo, E., 1994. Spectral element method for acoustic wave simulation in heterogeneous media, *Finite Elements in Analysis and Design*, **16**(3-4), 337–348.

Smith, W. D., 1975. The application of finite element analysis of body wave propagation problems, *Geophysical Journal of the Royal Astronomical Society*, **42**(2), 747 – 768.

Stanescu, D., Kopriva, D., & Hussaini, M., 2000. Dispersion Analysis for Discontinuous Spectral Element Methods, *Journal of Scientific Computing*, **15**(2), 149–171.

Stockwell, J., 1999. The CWP/SU: Seismic Unix package, *Computers and Geosciences*, **25**, 415–419.

Sun, S. & Wheeler, M., 2005. Discontinuous Galerkin methods for coupled flow and reactive transport problems, *Applied Numerical Mathematics*, **52**(2-3), 273–298.

Tordjman, N., 1995. *Eléments finis d'ordre élevé avec condensation de masse pour l'équation des ondes*, Ph.D. thesis, Université de Paris, IX-Dauphine.

Tordjman, N., Cohen, G., & Joly, P., 1994. Eléments finis d'ordre élevé avec condensation de masse pour l'équation des ondes en dimension 1, Rapport de Recherche 2323, INRIA, Le Chesnay, France.

Virieux, J., 1984. SH-wave propagation in heterogeneous media - Velocity-stress finite-difference method, *Geophysics*, **49**(11), 1933–1942.

Virieux, J., 1986. P-SV wave propagation in heterogeneous media - Velocity-stress finite-difference method, *Geophysics*, **51**(4), 889–901.

Watkins, D., 2002. *Fundamentals of Matrix Computations*, Pure and Applied Mathematics, John Wiley and Sons, 2nd edn.

Wheeler, M., 1978. An elliptic collocation-finite element method with interior penalties, *SIAM Journal on Numerical Analysis*, **15**(1), 152–161.

Vita

Jonás de Dios De Basabe Delgado was born in Ensenada, Baja California, México in 1975. He was the third of five children born to Beatriz and Ritter. In 2002 he married Eunice and they have one daughter together. In 1999 he graduated with honors from the State University of Baja California (Universidad Autónoma de Baja California, UABC) in Tijuana, with a bachelor's degree in Computer Engineering. He then studied a M.S. in Earth Sciences at the Ensenada's Center for Scientific Research and Higher Education (Centro de Investigación Científica y Educación Superior de Ensenada, CICESE) in Ensenada. He worked as a scientific-software developer in CICESE and as a teacher in UABC until 2004. Throughout his higher education and career he has participated in the Mexican Student Fellowship COMPA (Compañerismo Estudiantil). In 2004 he joined the Computational and Applied Mathematics Ph.D. program at the University of Texas at Austin under the supervision of Mrinal K. Sen and Mary F. Wheeler.

Permanent address: Calle Huétamo # 171, Colonia San Fernando,
Tecate, Baja California, México

This dissertation was typeset with LaTeX[†] by the author.

[†]LaTeX is a document preparation system developed by Leslie Lamport as a special version of Donald Knuth's TeX Program.